HAROKOPIO UNIVERSITY of ATHENS, GREECE

-School of Environment, Geography and Applied Economics,

Department of Geography-

Master on Applied Geography and Spatial Planning, Sector: Geoinformatics

"AMAZON RAINFOREST DEFORESTATION STUDY USING SAR POLARIMETRY METHODS"

Thesis Editing: Kanakaki Stavroula

Professor – Supervisor: Is. Parcharidis

Athens, February 2016

CONTENTS

11. AKNOWLEDGEMENTS

BIBLIOGRAPHY – REFERENCES

<u>Internet sources</u>

ABSTRACT

Nowadays science evolves more and more. Every day, new discoveries and inventions come to light. Remote Sensing is a field of earth sciences that become more and more popular the recent years because of its achievements.

More specifically, SAR Remote Sensing has helped a lot lately because of its potentials. The all-weather satellite instruments, the precision of its measurements and the extremely detailed results can give a new "weapon" to the scientists in order to study an organize more over important "earth issues".

SAR Polarimetry, furthermore, constitutes a major and separate field of SAR Remote Sensing since has its own rules and theory and it appears such capabilities that can offer notable results for helping in studying of special phenomena on earth that any other science could do with such accuracy, speed and detail.

Sectors like Ice melting, Deforestation and Soil Analyses and much more can make SAR Polarimetry a great science tool that can achieve a better and faster way in excellent management of Natural Disasters and rest Earth Phenomena.

Amazon Rainforest is one of the biggest and more important rainforests in Globe and its observation and protection are of extremely high importance. SAR Polarimetry has the advantage of achieving to study in depth the vegetation in such areas where optical satellite instruments are just useless. Moreover it can distinguish the different vegetated areas and cultivated parts of land. The results via this methodology are quite satisfying and reliable and the data processing does not take so much time as if we made fieldwork.

INTRODUCTION

SAR Polarimetry today has shown huge results about special studies in many areas. Analyzing data from satellite SAR systems like ERS-1 and RADARSAT-1 and its observations have demonstrated the value of monitoring the Earth for a wide range of applications, ranging from operational forecasting in near real-time to long-term climate studies. SAR systems began with single-polarization and single-frequency systems and now have reached the multiple polarizations level. Moreover, airborne acquisitions by polarimetric SARs have shown major improvements for a number of applications.

Furthermore, the combination of polarimetric SAR data and single polarization ones may become real useful for special and important case studies. SAR polarimetry methods have been approved extremely important for the cases like:

- Agriculture classification
- Sea ice monitoring
- Vegetation parameter retrieval

SAR Polarimetry as far it concerns the crop classification is able to discriminate between the different crop types. For the sea ice classification the polarimetry is especially advantageous for discrimination between thin ice types and between ice and water. Concluding, in the case of SAR interferometry, the polarimetry is an intergrated component of the approach, which enables quantitative estimation of the for instance vegetation parameters, in our cases forest height estimation, with high accuracy.

Except these fields that were mentioned above, SAR Polarimetry has many other applications in other fields, like: Agriculture Applications (Crop Productivity/within Field Variations, Scattering Mechanisms and Soil Conservation), Coastal Zone Applications (Shoreline Detection and Substrate Mapping), Forestry Applications (Frequency Dependence and Polarimetric Parameters), Hydrology Applications (Flood/Wetland Mapping, Snow Mapping and Soil Moisture Mapping), Oceans Applications (Marine Winds, Oil Slick Detection and Ship Detection), Sea Ice Applications (Ice Structure and Type, Ice-Water Ambiguity, Polarimetric Analyses for Sea-Ice and Sea-Ice Classification).

So, it is quite clear that SAR Polarimetry has a wide range of applications in earth sciences and in the future it is expected to solve a lot of problems.

AIM OF STUDY

Forests provide a source of oxygen treasure. For the human being, life without oxygen and green is impossible. Rainforests with the extremely dense vegetation provide a breath of life to all of us. The Amazon Rainforest produces about 20% of the earth’s oxygen (WWF) so it is quite clear how important is to be remained virgin and fully protected.

Unfortunately, recent years, Amazon rainforest overexploitation is growing increasingly having started provoking major problems in the local community but in the whole world too. The biggest problems are the illegal and non-systematic deforestation acts that make the situation just uncontrollable and unpredictable.

SAR Polarimetry is a scientific tool that has many advantages in crop and forest studies. In this thesis we used SAR satellite data and SAR Polarimetry and other methods for analyzing the data and studying the vegetation of the area. It was investigated a large area of Brazilian Amazon Forest that covers the areas: Parana. The images cover a long year period of almost 7 years which gives the opportunity to apply a multitemporal study.

The area that is investigated is covered by crops, residential areas and virgin forest land too. So we have an interesting dataset that gives a lot of information about the study area.

There have been used 2 different datasets: ENVISAT and ALOS images. The main aim of the study was to investigate areas that in the period that we refer to there are changes in land use, of any type.

LITERATURE REVIEW

Koyama C.N. et al 2010 have introduced a novel approach to develop an empirical soil moisture algorithm for dual-polarized PALSAR data. In particular the dual-pol H/A/Alpha decomposition was applied to exploit the polarimetric phase information contained in the FBD343 mode. The first results showed the great potential of the applied method to directly invert biomass and surface roughness information from the partial polarimetric L-band data. Along with the land-use classification capabilities of dual-polarized L-band SAR systems, the findings give a promising outlook in terms of the possibility to develop a really operational soil moisture retrieval model for PALSAR data collected in the FDB mode. That is, information on the land cover and the disturbing effects from vegetation and surface roughness can be derived without the use of a priori knowledge or auxiliary EO data (Koyama C.N. et al 2010).

Arai K. 2011 applied a method for polarimetric Synthetic Aperture Radar: MRA. SAR image classification with high frequency component derives from wavelet Multi-Resolution Analysis. It is found that the proposed features of three received echo signal power, HH, HV, and VV as well as HH4 of high component derived from MRA analysis with polarization signature are effective to improve classification performance for PI-SAR types of polarimetric SAR images. More than 10% of improvement of the classification performance is confirmed by adding HH4. The improvement depends on the level of MRA, because there is the most appropriate level depending on the frequency component of the polarization signature of the ground cover target. The computational resource requirement for the previously proposed maximum curvature of the trajectory in eigenvector space which is converted from the polarization signature is twice much larger than that of the proposed MRA based feature utilized classification. Thus it may said that the proposed high frequency component of polarization signature based classification method is superior to the conventional classification method with three echo signal powers, and to the previously proposed maximum curvature based classification method in terms of classification performance and the required computation resources (Arai K. 2011).

Jagdhuber 2012 tried the novel (multi-angular) polarimetric decomposition techniques for soil parameter retrieval which can be applied without test site calibration directly to agricultural areas. The developed algorithms are validated with fully polarimetric SAR data acquired by the airborne E-SAR sensor of the German Aerospace Center (DLR) for three different study areas in Germany. The achieved results reveal inversion rates up to 99% for the soil moisture and soil roughness retrieval in agricultural areas. However, in forested areas the inversion rate drops significantly for most of the algorithms, because the inversion in forests is invalid for the applied scattering models at L-band. The validation against simultaneously acquired field measurements indicates an estimation accuracy (root mean square error) of 5-10 vol.% for the soil moisture (range of in situ values: 1-46 vol.%) and of 0.37-0.45cm for the soil roughness (range of in situ values: 0.5-4.0 cm) within the catchment. So, the results showed that a continuous monitoring of soil parameters with the obtained precision, excluding frozen and snow covered conditions, is possible (Jagdhuber 2012).

Zwieback et al. 2012 proposed a statistical test for invariances in SAR polarimetry which is based on a likelihood ratio test. The possible null hypotheses are that the second-order statistics of the target are invariant to reflections, rotation or that they show azimuthal symmetry. The application of these tests to an agricultural scene (L-band) indicates: i) that there is a strong dependence on the number of looks and ii) that the topography as well as the land cover plays an important role. More generally, the symmetry tests might prove useful in different scenarios as pre-processing steps for decomposition and parameter inversion techniques, when the models exhibit invariances which might not be present in the data. Such tests could also be advantageous in classification studies or the estimation of the orientation angle from the coherency matrix, which relies on the medium showing reflection symmetry (about the axis to be determined), but not being rotationally invariant (Zwieback et al. 2012).

Ballester-Berman et al. 2013 worked on vineyards monitoring by means of radar sensors and specifically they have focused in soil moisture estimation. They worked on a two-component scenario where there is one dominant direct return from the soil and a multiple scattering component accounting for disturbing and non-modeled signal fluctuations from soil and short vegetation. They analyzed the polarimetric indicators that give support to such a model and have proposed a combined X-Bragg/Fresnel approach to characterize the polarized direct response from soil. Validation of polarimetric model has been performed in terms of its consistency with respect to the available data. Also, the analysis of laboratory data gathered at the EMSL over a rough surface gives support to these statements. High inversion rates are reported for different phenological stages of vines and according to the results presented here the model gives a consistent interpretation of the data as long as the volume component power remains about or below 50% of the surface component power (Ballester-Berman J.D. et al 2013).

Gallant et al. 2014 investigated the use of multitemporal polarimetric synthetic aperture radar (SAR) data acquired with Canada’s Radarsat-2 system to track within-season changes in wetland vegetation and surface water. They speculated, a priori, how temporal and morphological traits of different types of wetland vegetation should respond over a growing season with respect to four energy-scattering mechanisms. They used ground-based monitoring data and otherancillary information to assess the limits and consistency of the SAR data for tracking seasonal changes in wetlands. They found the traits of different types of vertical emergent wetland vegetation were detected well with the SAR data and corresponded with our anticipated backscatter responses. They also found using data from Landsat’s optical/infrared sensors in conjunction with SAR data helped remove confusion of wetland features with upland grasslands. These results suggest SAR data can provide useful monitoring information on the statuses of wetlands over time (Gallant et al. 2014).

Haldar D. et al 2014 focused on the utility of multi-dimension SAR data for crop condition assessment of various important tropical crops in India. VV/HV polarization stands to be better discriminator for wheat and mustard as compared to HH/HV. Circular cross polarized ratio added significantly to the discrimination capability. Combined use of RR/RL and HH/HV polarization increased the accuracy of crop discrimination by about 10%. Backscattered value increased with biomass in early to mid crop stage of cotton, mustard and Jute but extrapolation of trend indicates saturation at higher level of biomass in C- band. In case of wheat, decreasing trend of backscatter with relatively low sensitivity was observed at biomass above 5 kg per square meter in C-band. Thus there was scope of retrieval of the scattering parameters in higher wavelength in advanced crop stage. Probably soil backscattering dominated the trend in case of wheat however sampling with broader biomass range is necessary to corroborate the finding (Haldar D. et al 2014).

Lahlou N. et al 2014 proposed an original approach using TomSAR and PolTomSAR data to spatially discriminate the ground response and to characterize its intensity and polarimetric features in order to retrieve improved soil moisture information. They focused on modifications of the PolSARProSim software used to simulate multi-baseline PolInSAR images. The double-bounce intensity is then theoretically calculated and is compared to the results using the simulated data. From this, a new method was proposed to retrieve soil moisture under a vegetation layer (Lahlou N. et al 2014).

Hong S.-H. et al 2014 have used quad-pol C-band RADARSAT-2 data to explore the behavior of co- and cross-pol scattering behaviors in multipath wetland and urban environments. Interferometric processing of the wetland data shows that all four quad interferograms present similar fringe patterns reflecting water-level changes in the wetlands. Because the cross-pol signal clearly indicates scattering from the ground, we suggest that the cross-pol signal includes contributions from both volume and double-bounce scattering and not only volume scattering as commonly assumed. They used this new understanding to propose a modified scattering decomposition approach based on the coherency matrix that decomposes quad-pol data into four components: single bounce, co- and cross-pol double bounce, and volume scattering. They have applied the new decomposition to two study areas: first to the urban environment of San Francisco area and the other to the rural Everglades wetlands of South FL. The new decomposition results showed a very good fit between volume scattering and open areas, such as city parks, in San Francisco. It also showed that a significant part of the cross-pol signal in the urban area consists of double-bounce scattering from building oriented diagonally to the radar direction of illumination. In the wetland environment, the double-bounce component was extracted from the cross-pol showing the variation according to the characteristics of surface's vegetation. The decomposition of the cross-pol signal into volume and double-bounce components can improve SAR-based biomass estimates, which typically assume that the cross-pol signal solely reflects volume scattering (Hong S.-H. et al 2014).

Hong et al. 2015 processed quad-pol data using the Hong & Wdowinski four-component decomposition, which accounts for double bounce scattering in the cross-polarization signal. The calculated decomposition images consisted of four scattering mechanisms (single, co- and cross-pol double, and volume scattering). They applied an object-oriented image analysis approach to classify vegetation types with the decomposition results. They also used a high-resolution multispectral optical RapidEye image to compare statistics and classification results with Synthetic Aperture Radar (SAR) observations. The calculated classification accuracy was higher than 85%, suggesting that the TerraSAR-X quad-pol SAR signal had a high potential for distinguishing different vegetation types. Scattering components from SAR acquisition were particularly advantageous for classifying mangroves along tidal channels. They conclude that the typical scattering behaviors from model-based decomposition are useful for discriminating among different wetland vegetation types (Hong et al. 2015).

Alemohammad S. H. et al 2015 introduced a new framework to retrieve vegetation parameters and smooth-surface soil reflection coefficients using SAR polarimetry and the fully polarimetric covariance matrix of the backscattering signal from AirMOSS observations. The retrieved soil reflectivities (both horizontally and vertically -polarized) can then be used to estimate the soil moisture profile. The retrieval model takes into account contributions from surface, dihedral and volume scattering coming from the vegetation and soil components, and does not require prior vegetation parameters. This approach reduces the dependency of the retrieval on allometry-based vegetation models with large numbers of uncertain parameters (Alemohammad S. H. et al 2015).

Joerg H. et al 2015 have been applied tomographic SAR methodologies to agricultural vegetation. Even though the Rayleigh resolution in height was in the order of the vegetation heights, changes in the scattering characteristics could be detected. Differences could be clearly observed between species and between stages of the phonological cycle, such as changes in growth or penetration capabilities. The added value of SAR Tomography for agricultural vegetation is that it provides an increased observation space without the need of model assumptions. For instance, polarimetric interferometric SAR enables the separation of scattering centres in height using one baseline together with the polarimetric variation of the interferometric coherence but requires a model assumption for the vegetation volume. However, it has been found that there is a difference in terms of reliability of phase centres and complex reflectivities estimated from SAR Tomography. While phase centres could be reliably estimated, complex reflectivities appeared more challenging. In this regard, the interpretation of the related polarimetric signatures turned out to be rather difficult. One reason is the cross-talk from the ground to the volume layer and vice versa in which a key role is played by height resolution (Joerg H. et al 2015).

12. AMAZON RAINFOREST

12.1 The Amazon River

The Amazon River Basin is home to the largest rainforest on Earth. The basin -- roughly the size of the forty-eight contiguous United States -- covers some 40% of the South American continent and includes parts of eight South American countries: Brazil, Bolivia, Peru, Ecuador, Colombia, Venezuela, Guyana, and Suriname, as well as French Guiana, a department of France (Butler R. 2006).

Reflecting environmental conditions as well as past human influence, the Amazon is made up of a mosaic of ecosystems and vegetation types including rainforests, seasonal forests, deciduous forests, flooded forests, and savannas. The basin is drained by the Amazon River, the world's largest river in terms of discharge, and the second longest river in the world after the Nile. The river is made up of over 1,100 tributaries, 17 of which are longer than 1000 miles, and two of which (the Negro and the Madeira) are larger, in terms of volume, than the Congo (formerly the Zaire) river. The river system is the lifeline of the forest and its history plays an important part in the development of its rainforests (Butler R. 2006).

12.2 History

At one time Amazon River flowed westward, perhaps as part of a proto-Congo (Zaire) river system from the interior of present day Africa when the continents were joined as part of Gondwana. Fifteen million years ago, the Andes were formed by the collision of the South American plate with the Nazca plate. The rise of the Andes and the linkage of the Brazilian and Guyana bedrock shields, blocked the river and caused the Amazon to become a vast inland sea. Gradually this inland sea became a massive swampy, freshwater lake and the marine inhabitants adapted to life in freshwater. For example, over 20 species of stingray, most closely related to those found in the Pacific Ocean, can be found today in the freshwaters of the Amazon (Butler R. 2006).

About ten million years ago, waters worked through the sandstone to the west and the Amazon began to flow eastward. At this time the Amazon rainforest was born. During the Ice Age, sea levels dropped and the great Amazon lake rapidly drained and became a river. Three million years later, the ocean level receded enough to expose the Central American isthmus and allow mass migration of mammal species between the Americas (Butler R. 2006).

The Ice Ages caused tropical rainforest around the world to retreat. Although debated, it is believed that much of the Amazon reverted to savanna and montane forest. Savanna divided patches of rainforest into "islands" and separated existing species for periods long enough to allow genetic differentiation (a similar rainforest retreat took place in Africa. Delta core samples suggest that even the mighty Congo watershed was void of rainforest at this time). When the ice ages ended, the forest was again joined and the species that were once one had diverged significantly enough to constitute designation as separate species, adding to the tremendous diversity of the region. About 6000 years ago, sea levels rose about 130 meters, once again causing the river to be inundated like a long, giant freshwater lake (Butler R., 2006).

12.3 The Amazon River today

Today the Amazon River is the most voluminous river on Earth, eleven times the volume of the Mississippi, and drains an area equivalent in size to the United States. During the high water season, the river's mouth may be 300 miles wide and every day up to 500 billion cubic feet of water (5,787,037 cubic feet/sec) flow into the Atlantic. For reference, the Amazon's daily freshwater discharge into the Atlantic is enough to supply New York City's freshwater needs for nine years. The force of the current -- from sheer water volume alone -- causes Amazon River water to continue flowing 125 miles out to sea before mixing with Atlantic salt water. Early sailors could drink freshwater out of the ocean before sighting the South American continent (Butler R. 2006).

The river current carries tons of suspended sediment all the way from the Andes and gives the river a characteristic muddy whitewater appearance. It is calculated that 106 million cubic feet of suspended sediment are swept into the ocean each day. The result from the silt deposited at the mouth of the Amazon is Majaro island, a river island about the size of Switzerland (Butler R. 2006).

12.4 The Amazon rainforest

While the Amazon Basin is home to the world's largest tropical rainforest, the region consists of a number of ecosystems ranging from natural savanna to swamps. Even the rainforest itself is highly variable, tree diversity and structure varying depending on soil type, history, drainage, elevation, and other factors. This is discussed at greater length in the rainforest ecology section (Butler R. 2006).

12.5 The changing Amazon rainforest

The Amazon has a long history of human settlement, but in recent decades the pace of change has accelerated due to an increase in human population, the introduction of mechanized agriculture, and integration of the Amazon region into the global economy. Vast quantities of commodities produced in the Amazon — cattle beef and leather, timber, soy, oil and gas, and minerals, to name a few — are exported today to China, Europe, the U.S., and other countries. This shift has had substantial impacts on the Amazon (Butler R., 2006).

This transition from a remote backwater to a cog in the global economy has resulted in large-scale deforestation and forest degradation in the Amazon — more than 1.4 million hectares of forest have been cleared since the 1970s. An even larger area has been affected by selective logging and forest fires (Butler R. 2006).

Conversion for cattle grazing is the biggest single direct driver of deforestation. In Brazil, more than 60 percent of cleared land ends up as pasture, most of which has low productivity, supporting less than one head per hectare. Across much of the Amazon, the primary objective for cattle ranching is to establish land claims, rather than produce beef or leather. But market-oriented cattle production has nonetheless expanded rapidly during the past decade (Butler R. 2006).

Industrial agricultural production, especially soy farms, has also been an important driver of deforestation since the early 1990s. However since 2006 the Brazil soy industry has had a moratorium on new forest clearing for soy. The moratorium was a direct result of a Greenpeace campaign.

Mining, subsistence agriculture, dams, urban expansion, agricultural fires, and timber plantations also result in significant forest loss in the Amazon. Logging is the primary driver of forest disturbance and studies have shown that logged-over forests — even when selectively harvested — have a much higher likelihood of eventual deforestation. Logging roads grant access to farmers and ranchers to previous inaccessible forest areas (Butler R. 2006).

Deforestation isn't the only reason the Amazon is changing. Global climate change is having major impacts on the Amazon rainforest. Higher temperatures in the tropical Atlantic reduce rainfall across large extents of the Amazon, causing drought and increasing the susceptibility of the rainforest to fire. Computer models suggest that if current rates of warming continue, much of the Amazon could transition from rainforest to savanna, especially in the southern parts of the region. Such a shift could have dramatic economic and ecological impacts, including affecting rainfall that currently feeds regions that generate 70 percent of South America's GDP and triggering enormous carbon emissions from forest die-off. These emissions could further worsen climate change (Butler R. 2006).

12.6 Protecting the Amazon rainforest

While destruction of the Amazon rainforest is ongoing, the overall rate of deforestation rate in the region is slowing, mostly due to the sharp drop in forest clearing in Brazil since 2004 (Butler R. 2006).

Brazil's declining deforestation rate has been attributed to several factors, some of which it controls, some of which it doesn't. Since 2000 Brazil has established the world's largest network of protected areas, the majority of which are located in the Amazon region. Since 2004 the government has also had a deforestation reduction program in place. This includes improved law enforcement, satellite monitoring, and financial incentives for respecting environmental laws. Furthermore, the private sector — especially the soy, logging, and cattle industries — are increasingly responsive to consumer demand for less-damaging commodities. Finally the Brazilian Amazon has been the site of a number of innovative and ambitious conservation experiments, ranging from jurisdictional commodity certification to indigenous led Reducing Emissions from Deforestation and Degradation (REDD+) projects to Norway's billion dollar performance-based payment for cutting deforestation (Butler R. 2006).

12.7 Paraná River

Paraná is a river of South America, the second longest after the Amazon, rising on the plateau of southeast-central Brazil and flowing generally south to the point where, after a course of 3,032 miles (4,880 km), it joins the Uruguay River to form the extensive Río de la Plata estuary of the Atlantic Ocean (Encyclopaedia Britannica 2015).

The Paraná River's drainage basin, with an area of about 1,081,000 square miles (2,800,000 square km), includes the greater part of southeastern Brazil, Paraguay, southeastern Bolivia, and northern Argentina. From its origin at the confluence of the Grande and Paranaíba rivers to its junction with the Paraguay River, the river is known as the Alto (Upper) Paraná. This upper course has three important tributaries, namely the Tietê, the Paranapanema, and the Iguaçu, all three having their sources near the Atlantic coast in southeastern Brazil. The Alto Paraná's passage through the mountains was formerly marked by the Guaíra Falls; this series of massive waterfalls was completely submerged in the early 1980s by the reservoir of the newly built Itaipú dam complex, which spans the Alto Paraná (Encyclopaedia Britannica 2015).

From its confluence with the Iguaçu River to its junction with the Paraguay River, the Alto Paraná continues as the frontier between Paraguay and Argentina. When it is joined by the Paraguay, it becomes the lower Paraná and commences to flow only through Argentine territory. Near Santa Fé, the lower Paraná receives its last considerable tributary, the Salado River. Between Santa Fé and Rosario the delta of the Paraná begins to form, being 11 miles (18 km) wide at its upper end and roughly 40 miles (65 km) wide at its lower end. Within the delta the river divides again and again into distributary branches, the most important being the last two channels formed, the Paraná Guazú and the Paraná de las Palmas (Encyclopaedia Britannica 2015).

The volume of the lower Paraná River is dependent on the amount of water that it receives from the Paraguay River, which provides about 25 percent of the total; the Paraná's annual average discharge is 610,700 cubic feet per second (17,293 cubic metres per second). The basin of the Alto Paraná has a hot and humid climate year round, with dry winters and rainy summers. The climate of the middle and lower basins ranges from subtropical in the north to temperate humid in the south, with less plentiful rainfall. The Alto Paraná has two zones of vegetation, forests to the east and savanna to the west. Forests continue along the Paraná downstream to Corrientes, where the savanna begins to dominate both banks. The Paraná River has a rich and varied animal life that includes many species of edible fish. Much of the Paraná basin is economically unexploited. The main dam of the huge Itaipú project on the Paraná River was completed in 1982 and had a power generating capacity of 12,600 megawatts. The Yacyretá Dam on the lower Paraná River began operation in 1994. The lower river is a transport route for agricultural products, manufactured goods, and petroleum products, and its waters are used for irrigation of the adjacent farmlands (Encyclopaedia Britannica 2015).

13. BRAZIL – RAINFORESTS

Brazil holds about one-third of the world's remaining rainforests, including a majority of the Amazon rainforest. Terrestrially speaking, it is also the most biodiverse country on Earth, with more than 56,000 described species of plants, 1,700 species of birds, 695 amphibians, 578 mammals, and 651 reptiles (Butler R. 2014).

The bulk of Brazil's forest cover is found in the Amazon Basin, a mosaic of ecosystems and vegetation types including rainforests (the vast majority), seasonal forests, deciduous forests, flooded forests, and savannas, including the woody*cerrado*. This region has experienced an exceptional extent of forest loss over the past two generations—an area exceeding 760,000 square kilometers, or about 19 percent of its total surface area of 4,005,082 square kilometers, has been cleared in the Amazon since 1970, when only 2.4 percent of the Amazon's forests had been lost. The increase in Amazon deforestation in the early 1970s coincided with the construction of the Trans-Amazonian Highway, which opened large forest areas to development by settlers and commercial interests. In more recent years, growing populations in the Amazon region, combined with increased viability of agricultural operations, have caused a further rise in deforestation rates (Butler R. 2014).

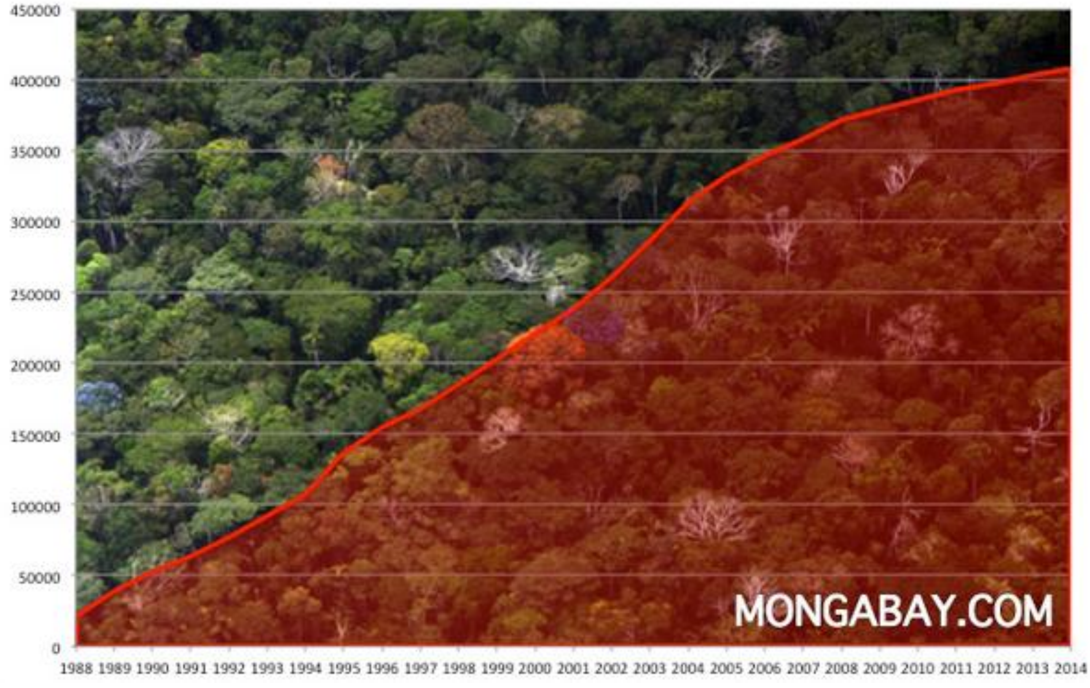

Figure 1 - Aggregated forest loss in the Brazilian Amazon, 1988-2014 (sq km)

(Source: Mongabay)

Recent studies indicate that these figures do not include extensive areas degraded by fires and selective logging. Research led by the Woods Hole Research Center and the Carnegie Institution's Department of Global Ecology found that each year the amount of forest degraded is roughly equivalent to the amount of forest cleared. The finding is trouble to ecologists because degraded forest has lower levels of biodiversity and is more likely to be cleared in the future. Further, degraded forest is more susceptible to fires (Butler R. 2014).

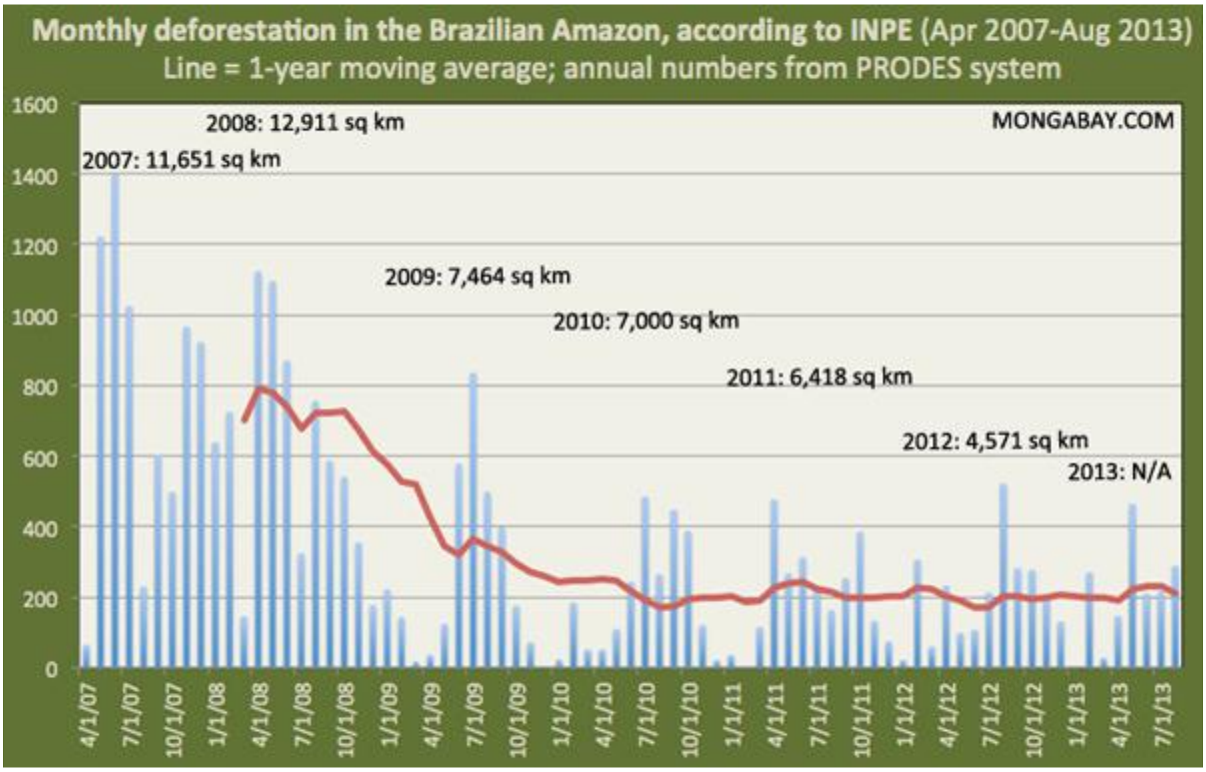

Figure 2 – Monthly deforestation over Brazilian Amazon, 2007-2013 (Source: Mongabay)

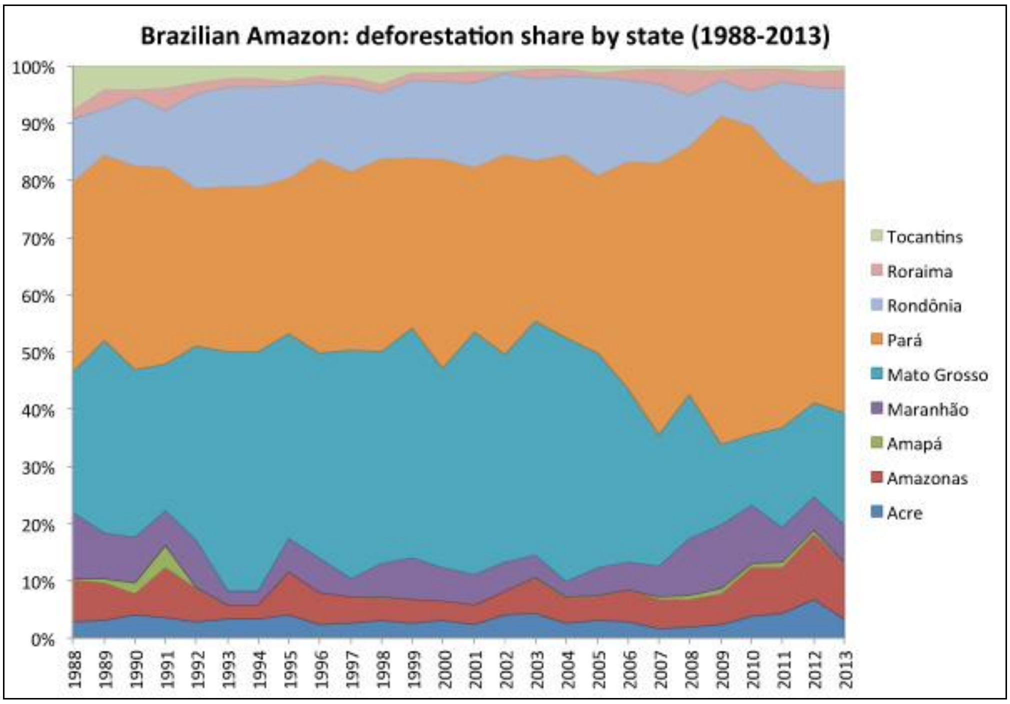

Figure 3 – Brazilian deforestation by state, 1988-2013 (Source: Mongabay)

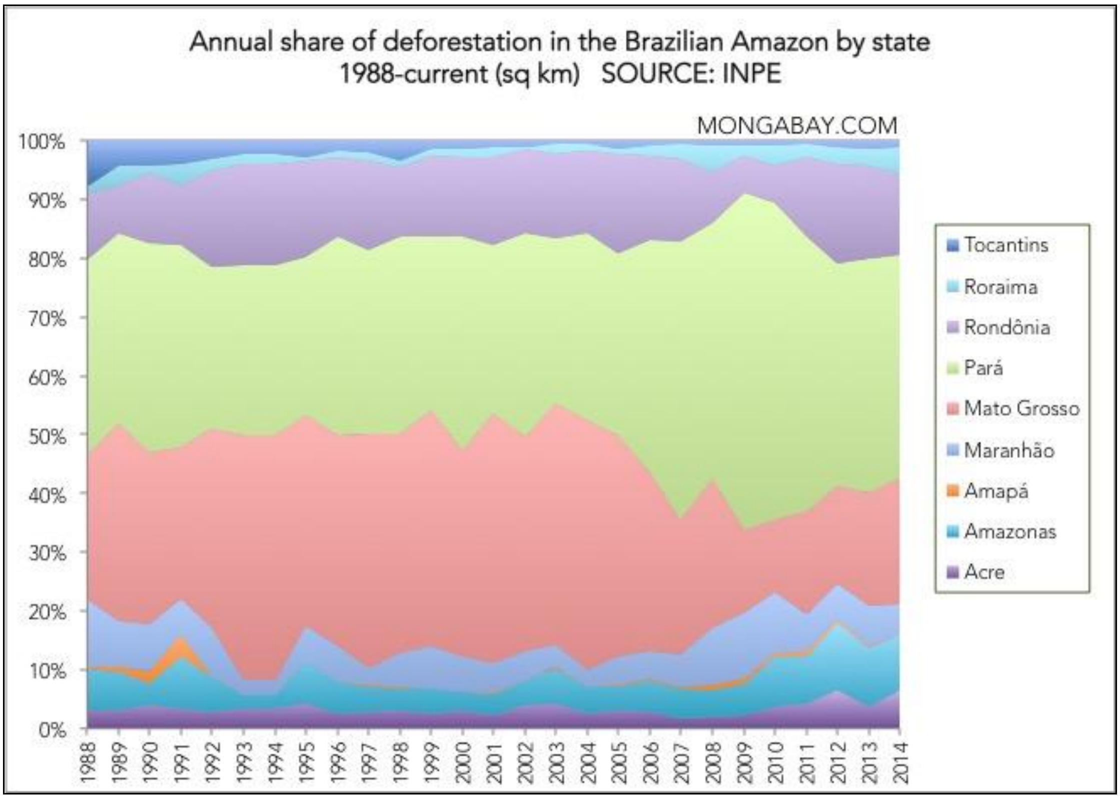

Figure 4 – Annual share of deforestation by state, 1988-2014 (Source: Mongabay)

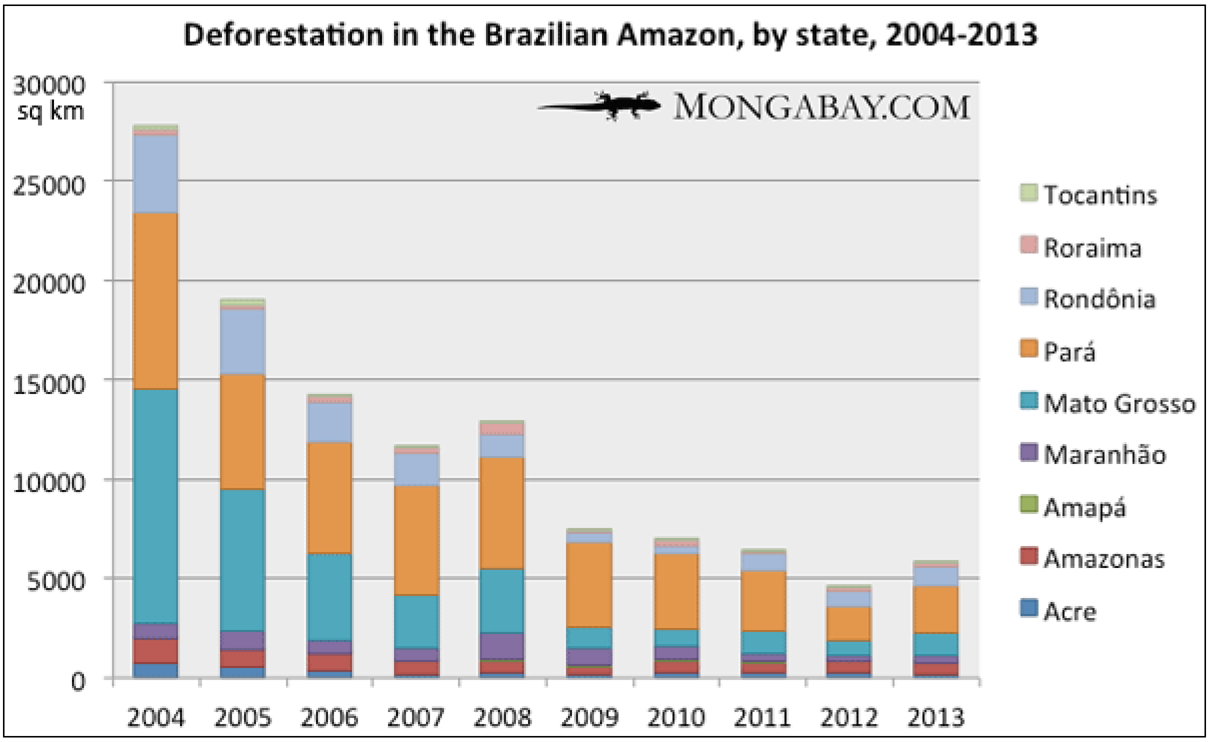

Figure 5 – Deforestation of Brazil by state, 2004-2013 (Source: Mongabay)

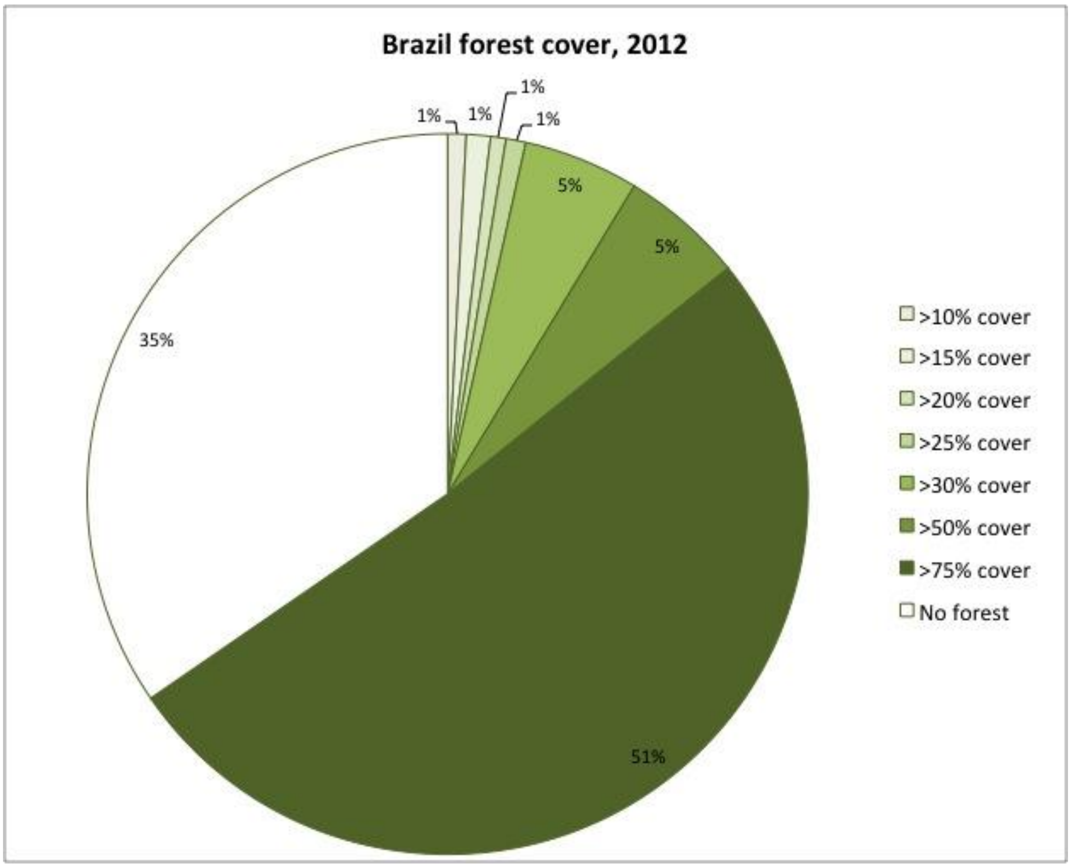

Figure 6 - Forest coverage of Brazil in 2012 (Source: Mongabay)

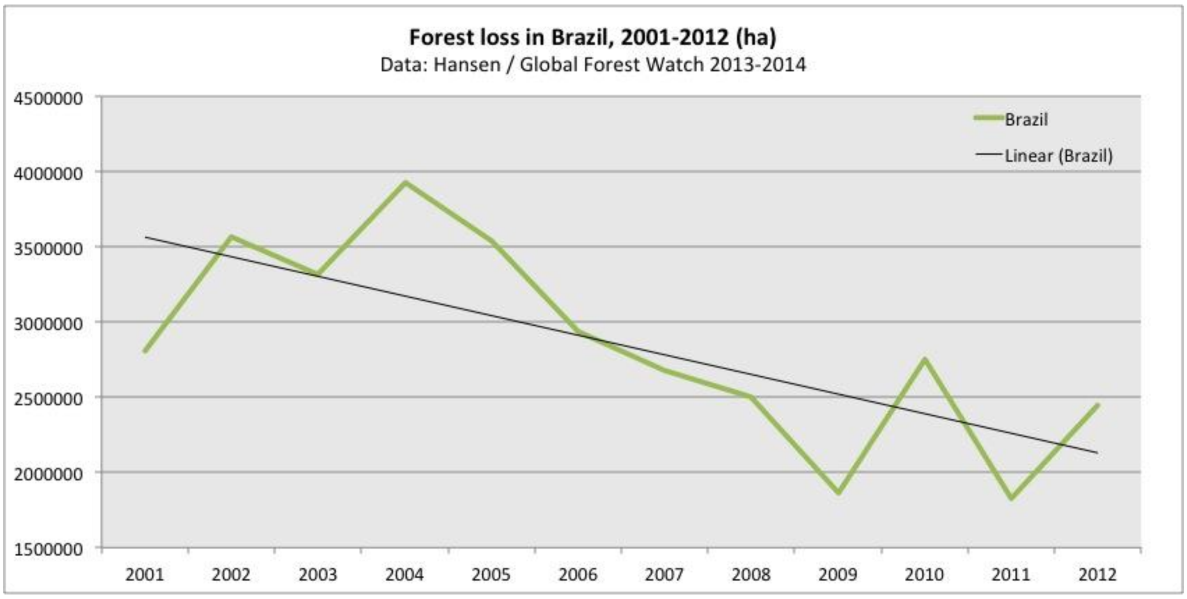

Figure 7 - Forest loss in Brazil, 2001-2012, (Source: Mongabay)

13.1 Why the Amazon rainforest is disappearing?

Historically the majority of deforestation has resulted from the actions of poor subsistence farmers, but in recent decades this has changed, with a greater proportion of forest clearing done by large landowners and corporations. Such is the case in Brazil, a large portion of deforestation can be attributed to land clearing for pasture by commercial and speculative interests (Butler R. 2014).

Since 2004 the rate of deforestation in the Brazilian Amazon has fallen nearly 80 percent to the lowest levels recorded since annual record keeping began in the late 1980s. Importantly, this decline has occurred at the same time that Brazil's economy has grown roughly 40 percent and agricultural output has surged, suggesting a decoupling of economic growth from deforestation (Butler R. 2014).

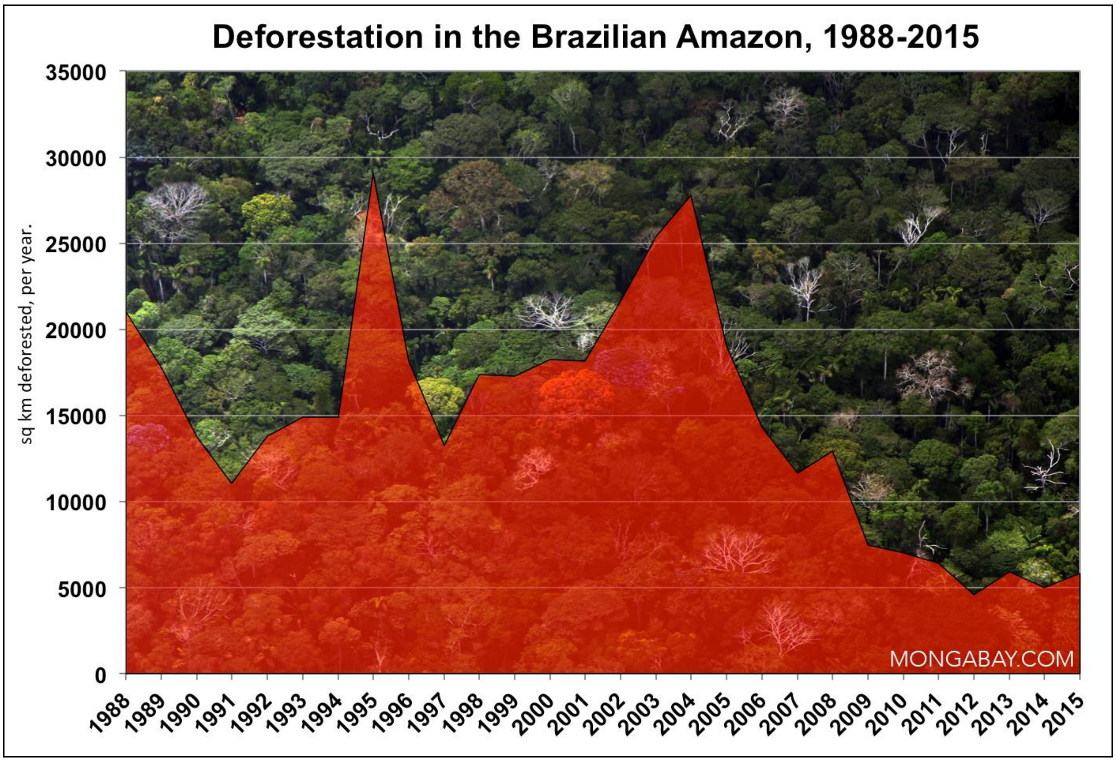

Figure 8 - Deforestation in the Brazilian Amazon, 1988-2015, (Source: Mongabay)

While this is welcome news for Earth's largest rainforest, there remains a risk that the trend could reverse. Furthermore, scientists worry that rising temperatures and increased incidence of drought are increasingly the vulnerability of the Amazon rainforest to catastrophic die-off (Butler R. 2014).

13.2 Causes of deforestation in Amazon

In evaluating deforestation in the Amazon, it is important to understand both direct and indirect drivers of forest loss (Butler R. 2014).

Direct drivers of deforestation including conversion of forests for pasture, farmland, and plantations, as well as surface mining, dams that inundate forested areas, and intense fires (Butler R. 2014).

Indirect drivers of deforestation include more subtle factors, like insecure land tenure, corruption, poor law enforcement, infrastructure projects, policies that favor conversion over conservation, and selective logging that create conditions or enable activities that facilitate forest clearing (Butler R. 2014).

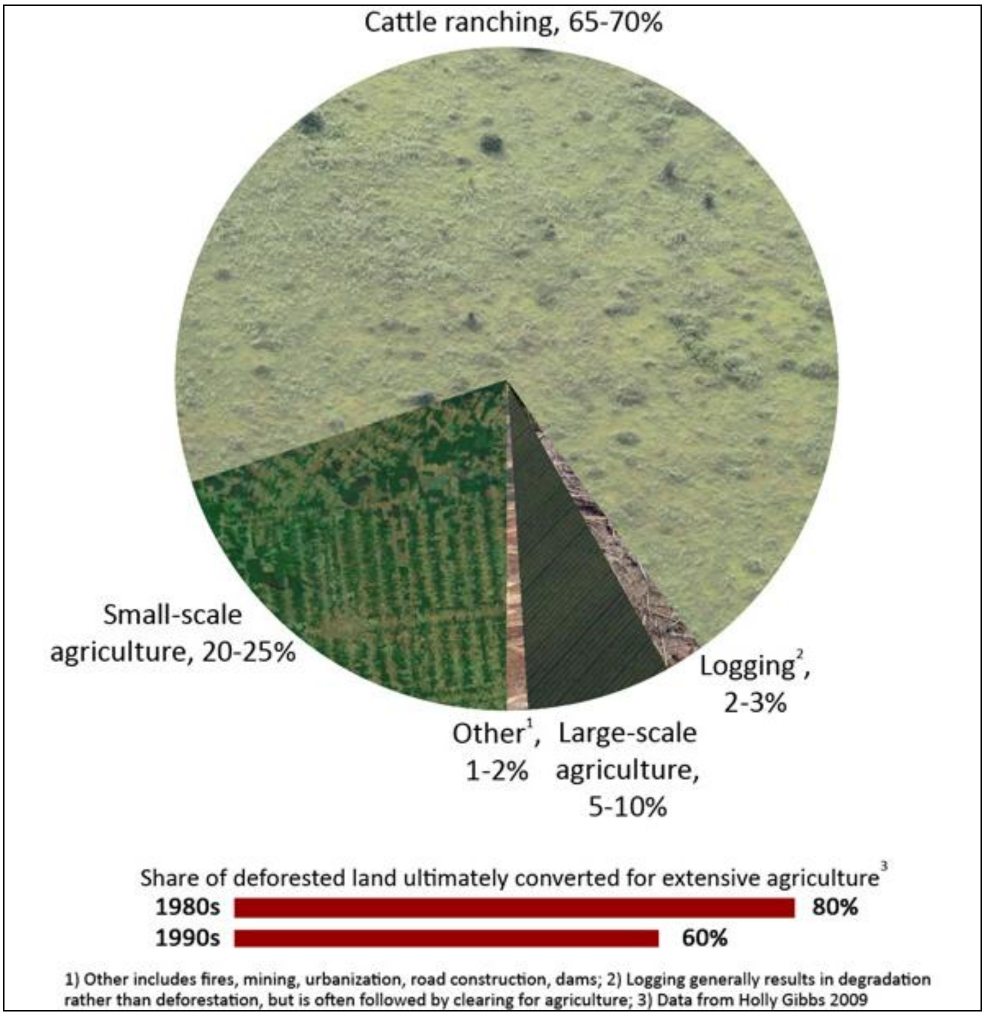

Figure 9 - Causes of Deforestation in the Brazilian Amazon, 2000-2005, (Source: Mongabay)

13.3 Cattle ranching

Conversion of rainforest for cattle pasture is the single largest driver of deforestation in Brazil. Clearing forest for pasture is the cheapest and easiest way to establish an informal claim to land, which can then be sold on to other parties at a profit. In some parts of the Brazilian Amazon, cleared rainforest land can be worth more than eight times that of land with standing forest. According to this, cattle ranching is often viewed as a way to speculate on appreciating land prices (Butler R. 2014).

However since 2000 ,cattle ranching in the Amazon has become increasingly industrialized, meaning that more ranchers are producing cattle to sell commercially. Most of the beef ends up in the domestic market, but secondary products like hides and leather are often exported (Butler R. 2014).

These exports left Brazilian cattle ranchers exposed in the late 2000's when Greenpeace launched a high profile campaign against companies that were sourcing leather and other products from major Brazilian cattle processors. That campaign led major companies to demand zero deforestation cattle. Combined with a crackdown by public prosecutors, the Brazilian cattle industry started to shift substantially toward less damaging practices in late 2009, contributing to the downward trend in deforestation (Butler R. 2014).

13.4 Soy

The model for the Brazilian cattle industry to move toward zero deforestation came from the country's soy industry, which underwent a similar transformation three years earlier. That shift was also initiative by a Greenpeace campaign, which targeted the soy-based chicken feed used by McDonald's in Europe. Within months of that campaign's launch, the largest soy crushers and traders in the Amazon had established a moratorium on buying soy produced via deforestation in the Amazon (Butler R. 2014).

13.5 Timber

Logging in the Brazilian Amazon remains plagued by poor management, destructive practices, and outright fraud. Vast areas of rainforest are logged -- legally and illegally -- each year (Butler R. 2014).

13.6 Palm Oil

At present, Amazon palm oil is not a major driver of deforestation in Brazil. The industry may in fact offer a more productive alternative to other land use in the region, if low productivity cattle pastures are instead converted into plantations (Butler R. 2014).

13.7 Dams, roads, and other infrastructure projects

Brazil is in the midst of an infrastructure construction spree, including scores of dams across the Amazon basin and a series of road projects that could greatly exacerbated deforestation. Mining is also a major activity in the region (Butler R. 2014).

13.8 Conservation in Brazil

While Brazil may be better known for losing its forests, it is important to recognize that it also leads the world in conservation efforts. During the 2000's Brazil easily led the world in establishing new protected areas. Those gains were consolidated in 2014, when donors established a trust fund that will underwrite the country's protected areas system through 2039 (Butler R. 2014).

Beyond strict protected areas, more than a fifth of the Brazilian Amazon lies within indigenous reservations, which research has shown reduce deforestation even more effectively than national parks. (Butler R. 2014)

13.9 Brazil's other forests

While the Amazon rainforest is Brazil's most famous forest, the country also has other types of forest (Butler R. 2014).

The Mata Atlântica or Atlantic Forest is a drier tropical forest that lies along the coast and inland areas to the south of the Amazon. It has been greatly reduced by conversion to agricultural -- especially sugar cane and cattle pasture -- and urbanization. The Mata Atlântica is arguably Brazil's most threatened forest (Butler R. 2014).

The Pantanal is an inland wetland that borders Paraguay and Bolivia and covers an area of 154,884 square kilometers. It includes a mosaic of forests and flooded grasslands (Butler R. 2014).

The cerrado biome is a tropical grassland that covers 1.9 square kilometers, or approximately 22 percent of the country. It is being rapidly destroyed for agriculture (Butler R. 2014).

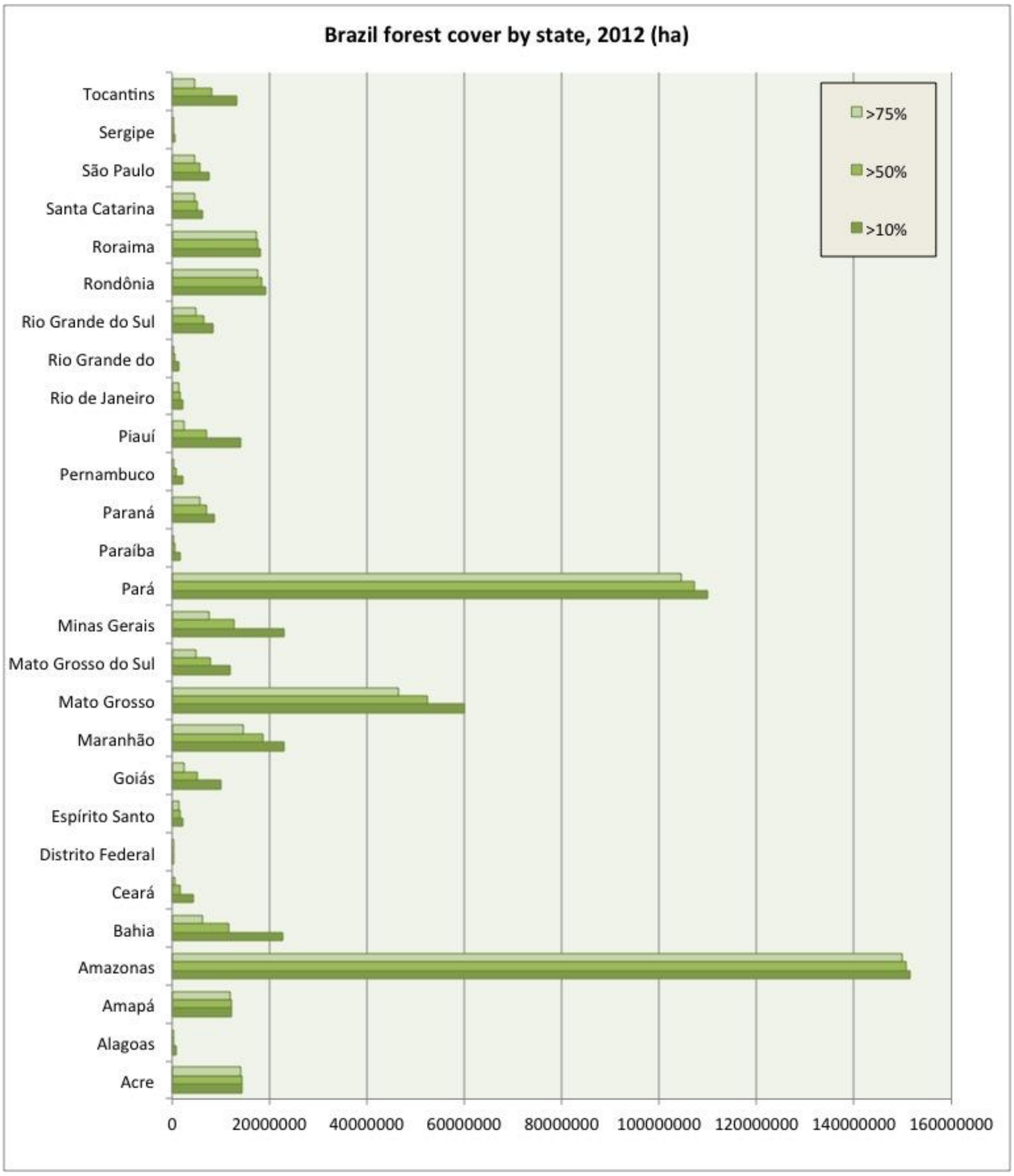

Figure 10 - Brazil forest cover by state, 2012 (ha) (Source: Mongabay)

	Total forest area		Dense forest area		Forest gain		Forest loss		Total land area
	>10% tree cover (ha)	% total land cover	>50% tree cover (ha)	% total land cover	2001-2012 (ha)	% total forest cover	2001-2012 (ha)	% total forest cover	(ha)
Acre	14459057	94.7%	14305428	93.7%	38568	0.3%	717510	5.0%	15264510
Alagoas	709713	25.8%	429847	15.7%	16103	2.3%	67853	9.6%	2746283
Amapc	12290163	87.9%	12087487	86.5%	55406	0.5%	167458	1.4%	13979727
Amazonas	151391279	98.4%	150644508	97.9%	178808	0.1%	1408988	0.9%	153804486
Bahia	22647380	40.5%	11736809	21.0%	450125	2.0%	2084198	9.2%	55983795
Cearc	4218042	28.6%	1511810	10.2%	39985	0.9%	225859	5.4%	14755448
Distrito Federal	95392	16.6%	29604	5.1%	1801	1.9%	1947	2.0%	574862
Espэrito Santo	2057050	47.3%	1582112	36.4%	214437	10.4%	188690	9.2%	4350624
Goics	9889091	29.2%	5281972	15.6%	122738	1.2%	781967	7.9%	33822612
Maranhyo	22887878	70.0%	18520943	56.7%	305543	1.3%	2028980	8.9%	32679563
Mato Grosso	59837613	66.4%	52426867	58.2%	432563	0.7%	8008840	13.4%	90082523
Mato Grosso do Sul	11940652	33.8%	7922995	22.4%	339934	2.8%	1105624	9.3%	35343712
Minas Gerais	22938990	39.3%	12823398	21.9%	1441341	6.3%	1765728	7.7%	58431030
Parc	109857933	90.6%	107119626	88.3%	778464	0.7%	8094417	7.4%	121310337
Paraэba	1527065	27.2%	550840	9.8%	12245	0.8%	108103	7.1%	5612509
Paranc	8757881	44.6%	6952841	35.4%	705152	8.1%	696715	8.0%	19655199
Pernambuco	2119205	21.8%	805364	8.3%	18284	0.9%	169401	8.0%	9731052
Piauэ	13940619	55.6%	6988488	27.9%	58661	0.4%	651154	4.7%	25056781
Rio de Janeiro	2071028	48.1%	1567191	36.4%	17359	0.8%	36974	1.8%	4301869
Rio Grande do Norte	1247591	23.7%	445996	8.5%	12486	1.0%	101138	8.1%	5262173
Rio Grande do Sul	8478395	32.0%	6474836	24.4%	660316	7.8%	316357	3.7%	26523923
RondÏnia	19098664	81.2%	18263404	77.7%	110964	0.6%	2911851	15.2%	23515610
Roraima	18119122	81.3%	17676744	79.3%	50301	0.3%	391846	2.2%	22291314
Santa Catarina	6368048	68.2%	5286504	56.6%	665655	10.5%	456982	7.2%	9333590
Syo Paulo	7598423	31.3%	5625284	23.2%	767099	10.1%	612764	8.1%	24280216
Sergipe	649191	29.7%	408395	18.7%	18903	2.9%	113437	17.5%	2183428
Tocantins	13251526	48.0%	8225329	29.8%	73352	0.6%	949514	7.2%	27607025
Brazil	548446992	65.4%	475694623	56.7%	7586593	1.4%	34164293	6.2%	838484205

Figure 11 - Brazilian forest statistical data (2001-2012) (Source: Mongabay)

Forest Cover

Total forest area: 477,698,000 ha
% of land area: 57.2%

Primary forest cover: 415,890,000 ha
% of land area: 49.8%
% total forest area: 87.1%

Deforestation Rates, 2000-2005

Annual change in forest cover: -3,103,000 ha
Annual deforestation rate: -0.6%
Change in defor. rate since '90s: 22.0%
Total forest loss since 1990: -42,329,000 ha
Total forest loss since 1990:-8.1%

Primary or "Old-growth" forests
Annual loss of primary forests: -3466000 ha
Annual deforestation rate: -0.8%
Change in deforestation rate since '90s: 35.0%
Primary forest loss since 1990: -17,330,000 ha
Primary forest loss since 1990:-9.7%

Forest Classification

Public: n/a
Private: n/a
Other: n/a
Use
Production: 5.5%
Protection: 17.8%
Conservation: 8.1%
Social services: 23.8%
Multiple purpose: 44.8%
None or unknown: n/a

Forest Area Breakdown

Total area: 477,698,000 ha
Primary: 415,890,000 ha
Modified natural: 56,424,000 ha
Semi-natural: n/a
Production plantation: 5,384,000 ha
Production plantation: n/a

Plantations

Plantations, 2005: 5,384,000 ha
% of total forest cover: 1.1%
Annual change rate (00-05): 21,000,000 ha

Carbon storage

Above-ground biomass: 79,219 M t
Below-ground biomass: 22,017 M t

Area annually affected by

Fire: 68,000 ha
Insects: 30,000 ha
Diseases: 20,000 ha

Number of tree species in IUCN red list

Number of native tree species: 7,880
Critically endangered: 34
Endangered: 100
Vulnerable: 187

Wood removal 2005

Industrial roundwood: 168,091,000 m^3 o.b.
Wood fuel: 122,385,000 m^3 o.b.

Table 2 - Statistics of Brazilian Amazon Forest

(Source: Mongabay)

Value of forest products, 2005

Industrial roundwood: $2,897,019,000
Wood fuel: $942,020,000
Non-wood forest products (NWFPs): $193,131,000
Total Value: $4,032,170,000

Period	Estimated Remaining Forest Cover in the Brazilian Amazon (sq. km)	Annual forest loss (sq. km)	Percent of 1970 cover remaining	Total forest loss since 1970 (sq. km)
pre-1970	4,100,000			
1970	4,001,600		97.6%	98,400
1977	3,955,870	21,130	96.5%	144,130
1978-1987	3,744,570	21,130	91.3%	355,430
1988	3,723,520	21,050	90.8%	376,480
1989	3,705,750	17,770	90.4%	394,250
1990	3,692,020	13,730	90.0%	407,980
1991	3,680,990	11,030	89.8%	419,010
1992	3,667,204	13,786	89.4%	432,796
1993	3,652,308	14,896	89.1%	447,692
1994	3,637,412	14,896	88.7%	462,588
1995	3,608,353	29,059	88.0%	491,647
1996	3,590,192	18,161	87.6%	509,808
1997	3,576,965	13,227	87.2%	523,035
1998	3,559,582	17,383	86.8%	540,418
1999	3,542,323	17,259	86.4%	557,677
2000	3,524,097	18,226	86.0%	575,903
2001	3,505,932	18,165	85.5%	594,068
2002	3,484,281	21,651	85.0%	615,719
2003	3,458,885	25,396	84.4%	641,115
2004	3,431,113	27,772	83.7%	668,887
2005	3,412,099	19,014	83.2%	687,901
2006	3,397,814	14,285	82.9%	702,186
2007	3,386,163	11,651	82.6%	713,837
2008	3,373,252	12,911	82.3%	726,748
2009	3,365,788	7,464	82.1%	734,212
2010	3,358,788	7,000	81.9%	741,212
2011	3,352,370	6,418	81.8%	747,630
2012	3,347,799	4,571	81.7%	752,201
2013	3,341,908	5,891	81.5%	758,092
	3,336,896	5,012	81.4%	763,104
2015	3,331,065	5,831	81.2%	768,935

Figure 11 – Statistics of Amazon deforestation, pre-1970-2015 (Source: Mongabay)

14. STUDY AREA

The Amazon is the world's largest rainforest, stretching over an area of more that 5 million square kilometers. In Brazil, the forest originally occupied over 4 million square kilometers – an area equivalent to almost half of continental Europe. Today, around 80% of the Brazilian Amazon remains covered by native vegetation, making it an important carbon sink. The Brazilian Amazon also holds unique biodiversity and 20% of the planet's fresh water (J. Assunção 2013).

Protecting the Amazon from illegal deforestation and enforcing environmental regulation in the region is a challenge as immerse as the forest itself. Yet, the pace of forest clearings appears to have lost momentum in recent years. Amazon deforestation rates escalated in the early 2000s, but after peaking at over 27,000 square kilometers in 2004, decreased sharply to about 5,000 square kilometers in 2011 (J. Assunção 2013).

Climate change and biodiversity concerns have pushed tropical deforestation into occupying a position at the top of the global policy debate priority list. Understanding deforestation in the Brazilian Amazon and how to most efficiently prevent it is therefore currently a matter of first-order importance not only for Brazil, but for the global community (J. Assunção 2013).

This thesis focuses mainly on SAR Polarimetry methodology and techniques that may be very useful for examining these vegetated areas where optical data can't penetrate the dense cloudy system of the rainforest and common SAR data can't analyze canopy and vegetation features (J. Assunção 2013).

14.1 Study area of Envisat images

In the following image we can see the area that Envisat images refer to. All envisat images were splitted up to 2 groups. The group of 7 scenes was used for applying a seasonal analysis of the area since all the images are of the same date (2006). The other group of 4 images was used for multitemporal analysis since the scenes refer to different year dates (2004-2006). It's very important to mention that as we can see from the screenshot above, all Envisat images cover exactly the same area. Off course the images were cut so the covering area was restricted.

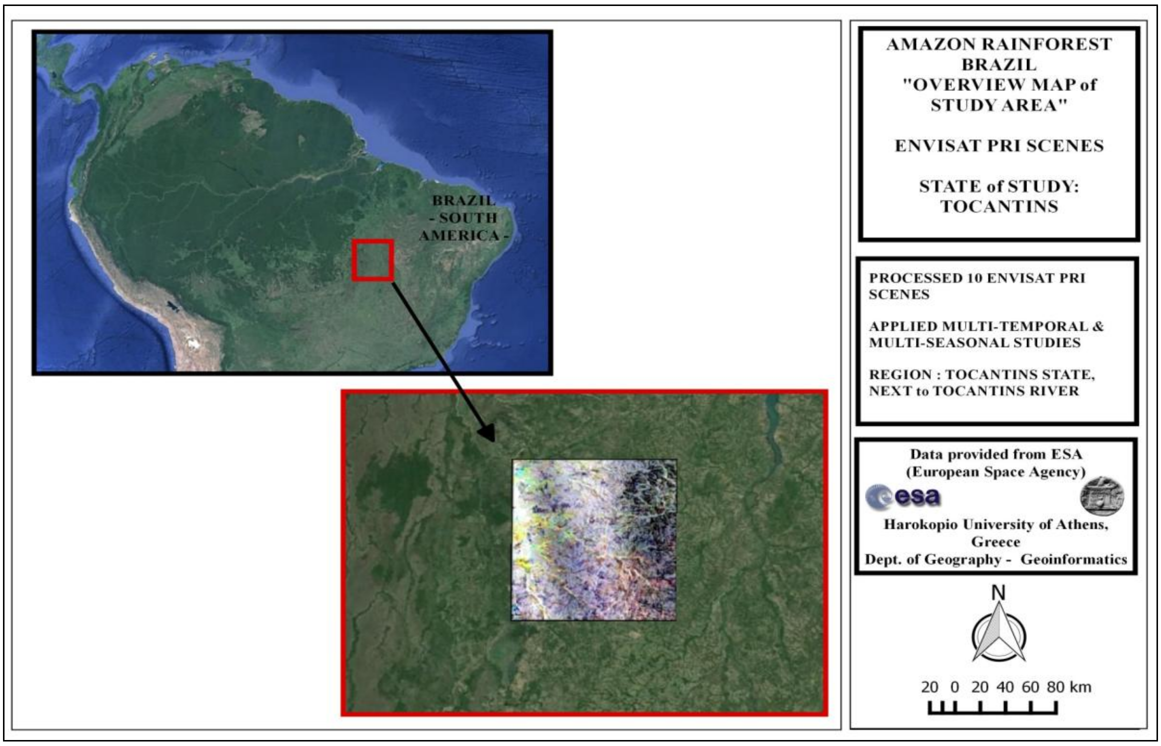

Figure 12 - Study Area of Envisat scenes, Tocantins State

Figure 13 - Study area screenshot of Alos images (Source: GoogleEarth).

These images cover a special region in the state of Tocantins on the western part of it. On the east of them there is the Tocantins River while they caver an area that consists of both residential villages such as: Crixás do Tocantins and Aliança do Tocantins, and virgin forest areas.

14.2 Study area of Alos images

In the image above you can see from a screenshot image of Google Earth, the area covering from the 24 ALOS scenes that we processed. This area contains part of the states: Pará, Amapá, Tocantins and Goiás of Brazil country.

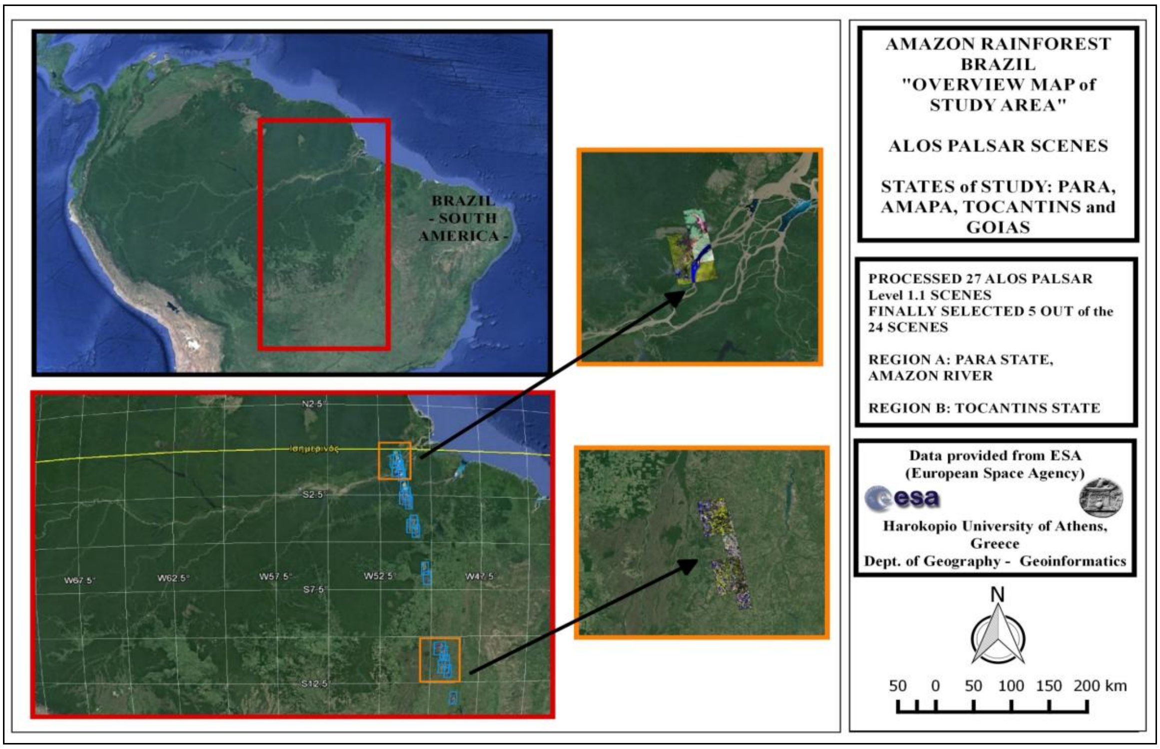

Figure 14 - Study Area of Alos scenes, Para, Amapa, Goias and Tocantins State

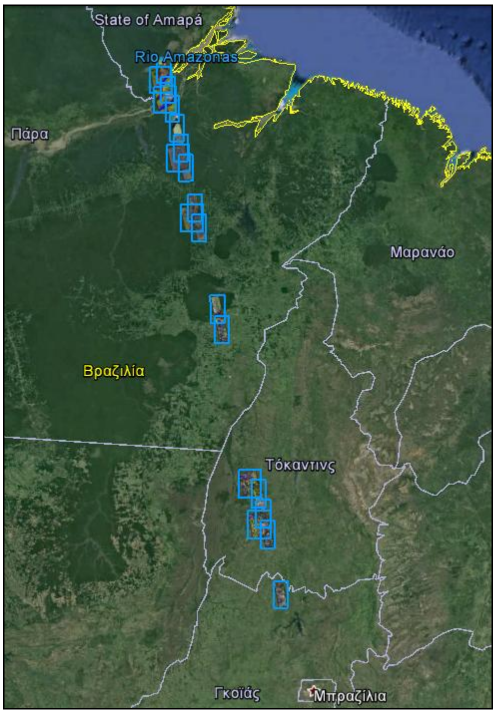

FIgure 15 - Study area of ALOS images (Source: GoogleEarth)

They cover a vast area of Amazon forest and the most important point is that they extend in a long land strip from the Amazon River on the north to the Goiás state on the south. As we previously mentioned there are 24 ALOS scenes where many of them cover almost the same area which permitted the special region study. The areas that we have many images are: a region from the Amazon River estuary to the south in the state Pará and another region in the southwestern part of Tocantins state. So, these will be the areas of special study where we will deepen in our investigation.

Pará state locates in northern Brazil (see Figure above) through which the lower Amazon River flows to the sea. It is bounded to the north by Guyana, Suriname, and the Brazilian state of Amapá, to the northeast by the Atlantic Ocean, to the east by the Brazilian states of Maranhão and Tocantins, to the south by Mato Grosso, and to the west by Amazonas. It is the second largest state in Brazil. The capital and chief city is Belém (Encyclopaedia Britannica 2015).

Figure 16 - Pará state in northern Brasil (Source: Encyclopedia Britannica, Inc. 2015)

Amapá locates in the northern Brazil (see figure above). It is bounded on the north by a small portion of Suriname and by French Guiana, on the northeast by the Atlantic Ocean, on the south and west by the Brazilian state of Pará, and on the southeast by the Amazon River. Formerly a part of Pará state, Amapá was created a territory in 1943 and became a state in 1990, with its capital at Macapá. Most of the state is tropical rainforest, and there are patches of savanna along the coast, which has long remained scantily populated (Encyclopaedia Britannica 2015).

Figure 17 - Amapá state in northern Brasil (Source: Encyclopedia Britannica, Inc. 2015)

Tocantins is an inland state of north-central Brazil (see figure above). It is bounded by the states of Maranhão and Piauí to the northeast, Bahia to the east, Goiás to the south, Mato Grosso to the west, and Pará to the northwest. The capital is Palmas. The state lies in the Brazilian Highlands at elevations between 330 and 1,300 feet (100 and 400 metres) above sea level (Encyclopaedia Britannica 2015).

Figure 18 - Tocantins state in northern Brasil (Source: Encyclopedia Britannica, Inc. 2015)

Goiás, formerly Goyaz, state locates in the south-central Brazil. Goiás is the site of the Distrito Federal (Federal District) and national capital, Brasília. It is bounded by the states of Tocantins on the north, Bahia and Minas Gerais on the east, Minas Gerais and Mato Grosso do Sul on the south, and Mato Grosso on the west. The state capital, since 1937, has been Goiânia (Encyclopaedia Britannica 2015).

Figure 19 - Goiás state in northern Brasil (Source: Encyclopedia Britannica, Inc. 2015)

In the area that cover the ALOS scenes it is exists a rich river hydrographic network that contains many rivers, small and bigger ones.

Paraná river of South America, the second longest after the Amazon, rising on the plateau of southeast-central Brazil and flowing generally south to the point where, after a course of 3,032 miles (4,880 km), it joins the Uruguay River to form the extensive Río de la Plata estuary of the Atlantic Ocean. The Paraná River's drainage basin, with an area of about 1,081,000 square miles (2,800,000 square km), includes the greater part of southeastern Brazil, Paraguay, southeastern Bolivia, and northern Argentina (Encyclopaedia Britannica 2015).

Figure 20 - Paraná River (Source: Encyclopedia Britannica, Inc. 2015)

Tocantins river rises in several headstreams on the central plateau in Goiás state, Brazil. It flows northward through Goiás and then Tocantins states until it receives the Manuel Alves Grande River. Looping westward, it marks the boundary of Tocantins and Maranhão states as far as its junction with the Araguaia River. The Tocantins again turns northward and flows into the Pará River, a navigable arm of the Amazon River delta, which empties into the Atlantic Ocean. Although the Tocantins-Araguaia system is popularly regarded as a tributary of the Amazon, it is technically a separate system, with a drainage basin of more than 300,000 square miles (800,000 square kilometres) (Encyclopaedia Britannica 2015).

Xingu river locates in Mato Grosso and Pará states, Brazil. The river rises on the Planalto (plateau) do Mato Grosso, in the drainage basin framed by the Serra do Roncador and the Serra Formosa mountain ranges. Formed by several headstreams, principally the Curiseu, Batovi, and Romuro rivers, the Xingu meanders generally northward for approximately 1,300 mi (2,100 km), emptying into the Amazon River just south of the Ilha (island) Grande de Gurupá. South of Altamira it receives its main tributary, the Iriri (800 mi long) (Encyclopaedia Britannica 2015).

Anapu river is a smaller one that locates in the Pará state near Baía de Caxiuanã (bay).

Canal do Norte is the northern channel of the Amazon River and locates in the Pará state.

Moreover, there are many lagoons as well as bays that exist in the study area. Lake "Lagoa do Boi" that locates on the center part of Tocantins state, Cana Brava lake locates near Tocantins river in the state of Goiás. Finally, lakes: Caxiuanã and Pacajá which are connected, situated in the state Pará, play a major role in the local people life.

15. RADAR POLARIMETRY

The theory of electromagnetic waves polarimetry has been always a very active and profuse research topic. In a first period, researchers were mainly concerned about the basics of this theory. Whereas, the recent availability of high resolution radar devices has also opened the door for those scientists more interested into the applications of this theory, which main hobbyhorse has been to increase the knowledge about our environment and its dynamics (López-Martínez C. 2005).

Radar Polarimetry (*Polar*: polarization, *Metry*: measure) is the science of acquiring, processing and analyzing the polarization state of an electromagnetic field. Radar polarimetry is concerned with the utilization of polarimetry in radar applications. Although polarimetry has a long history which reaches back to the 18th Century, the earliest work that is related to radar dates back to the 1940s. In 1945 G.W. Sinclair introduced the concept of the scattering matrix as a descriptor of the radar cross section of a coherent scatterer. In the late 1940s and the early 1950s major pioneering work was carried out by E.M. Kennaugh. He formulated a backscatter theory based on the eigenpolarizations of the scattering matrix introducing the concept of optimal polarizations by implementing the concurrent work of G.A. Deschamps, H. Mueller, and C. Jones. Work continued after Kennaugh, but only a few notable contributions, as those of G.A. Deschamps 1951, C.D. Graves 1956, and J.R. Copeland 1960, were made until Huynen's studies in 1970s. The beginning of a new age was the treatment presented by J.R. Huynen in his doctoral thesis of 1970, where he exploited Kennaugh's optimal polarization concept and formulated his approach to target radar phenomenology. With this thesis, a renewed interest for radar polarimetry was raised. However, the full potential of radar polarimetry was never fully realized until the early 1980s, due in no small parts to the advanced radar device technology. Technological problems led to a series of negative conclusions in the 1960s and 1970s about the practical use of radar systems with polarimetric capability. Among the major contributions of the 1970s and 1980s are those of W-M Boerner who pointed out the importance of polarization first in addressing vector electromagnetic inverse scattering. He initiated a critical analysis of Kennaugh's and Huynen's work and extended Kennaugh's optimal polarization theory. He has been influential in causing the radar community to recognize the need of polarimetry in remote sensing applications (Boerner W.-M. 2007).

Polarimetry deals with the full vector nature of polarized (vector) electromagnetic waves throughout the frequency spectrum from Ultra-Low-Frequencies (ULF) to above the Far-Ultra-Violet (FUV). Whenever there are abrupt or gradual changes in the index of refraction (or permittivity, magnetic permeability, and conductivity), the polarization state of a narrow band (single-frequency) wave is transformed, and the electromagnetic "vector wave" is re-polarized. When the wave passes through a medium of changing index of refraction, or when it strikes an object such as a radar target and/or a scattering surface and it is reflected; then, characteristic information about the reflectivity, shape and orientation of the reflecting body can be obtained by implementing 'polarization control'. The complex direction of the electric field vector, in general describing an ellipse, in a plane transverse to propagation, plays an essential role in the interaction of electromagnetic 'vector waves' with material bodies, and the propagation medium. Whereas, this polarization transformation behavior, expressed in terms of the "polarization ellipse" is named "Ellipsometry" in Optical Sensing and Imaging, it is denoted as "Polarimetry" in Radar, Lidar/Ladar and SAR Sensing and Imaging - using the ancient Greek meaning of "measuring orientation and object shape". Thus, ellipsometry and polarimetry are concerned with the control of the coherent polarization properties of the optical and radio waves, respectively (Boerner W.-M. 2007).

15.1 Polarisation

The difference between horizontally polarized and vertically polarized signals is explained below. An electromagnetic (radio) wave (satellite signal) consists of two components: A ***magnetic field*** and an ***electric field*** **(**Ockert 2011).

These 2 fields oscillate (vibrate) in the same direction on the same (parallel) axis 90 degrees apart.

Therefore, signals transmitted by satellite can be polarized in one of four different ways:

- Linear horizontal
- Linear vertical
- Left-hand circular
- Right-hand circular

Polarization types

- Vertically polarized

An antenna is vertically polarized when its electrical field is perpendicular to the Earth's surface. Vertically polarized signals oscillate from top to bottom. Signals are transmitted in all directions. Therefore, vertical polarization is used for ground-wave transmission, allowing the radio wave to travel a considerable distance along the ground surface with minimum attenuation.

- Horizontally polarized

Horizontally polarized antennas have their electric field parallel to the Earth's surface. Horizontally, polarized signals oscillate from left to right. Horizontal polarization frequencies are parallel to and touch the earth. Since the earth acts a good conductor at low frequencies, it shows some of the frequencies and prevents the signals from travelling very far.

- Circular polarization

Circular polarization is most often use on satellites. The polarization of the signal is rotating. Due the position of the Earth with respect to the satellite, geometric differences may vary. Circular polarization will keep the signal constant regardless of anomalies.

Horizontal and vertical polarized signals will not interfere with each another because they are differently polarized (90 degrees apart) **(**Ockert 2011).

Spatial evolution of a plane wave vector: helicoidal trajectory

At a fixed time, $t=t_0$, the electric field is composed of two orthogonal sinusoidal waves with, in general, different amplitudes and phases at the origin.

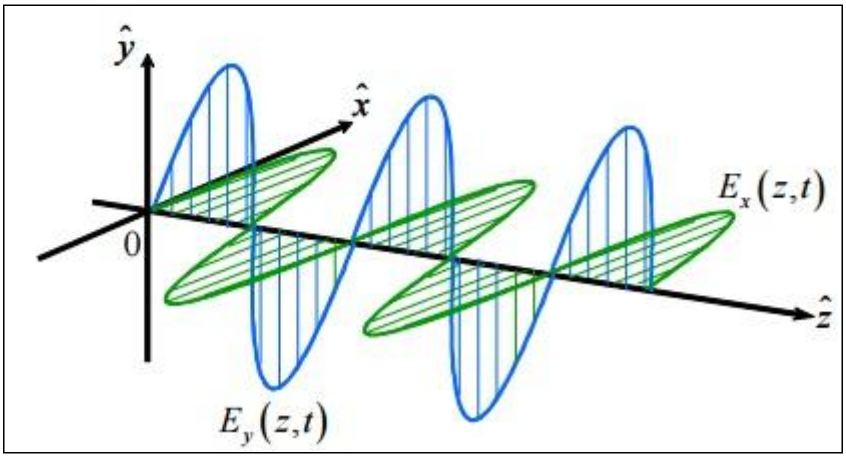

Figure 21 - Spatial evolution of a monochromatic plane wave components (López-Martínez C. 2005)

Three particular cases are generally discriminated:

Linear polarization: $\boldsymbol{\delta=\delta_y - \delta_x=0 + m\pi}$

The electric field is then a sine wave inscribed within a plane oriented with an angle ϕ with respect to $\hat{x}$

$$\vec{E}(z_0,t)=\sqrt{E_{0x}^2+E_{0y}^2}\begin{bmatrix}\cos\phi\\ \sin\phi\\ 0\end{bmatrix}\cos(\omega t_0-kz+\delta_x)$$

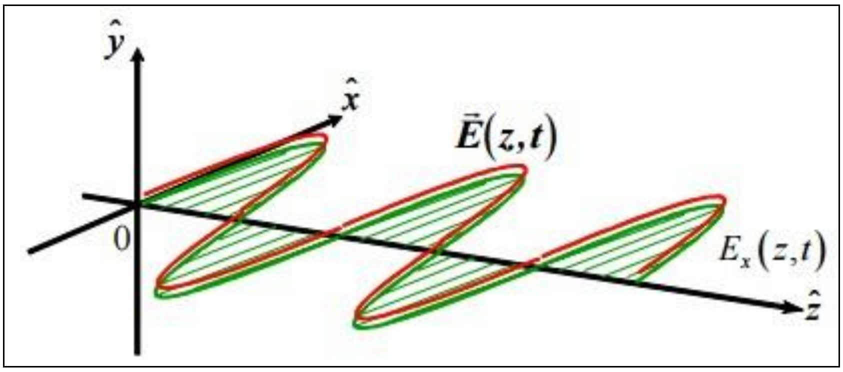

Figure 22 - Spatial evolution of a linearly (horizontal) polarized plane wave (López-Martínez C. 2005)

Circular polarization $\boldsymbol{\delta=\delta_y - \delta_x=0 + m\pi/2}$ and $E_{0x} = E_{0y}$

In this case, the wave has a constant modulus and is oriented with an angle (z) with ϕ respect to the axis $\hat{x}$

$$\left|\vec{E}(z,t_0)\right| = E_{0x}^2 + E_{0y}^2 \text{ and } \phi(z) = \pm(\omega t_{\grave{a}} - kz + \delta_x)$$

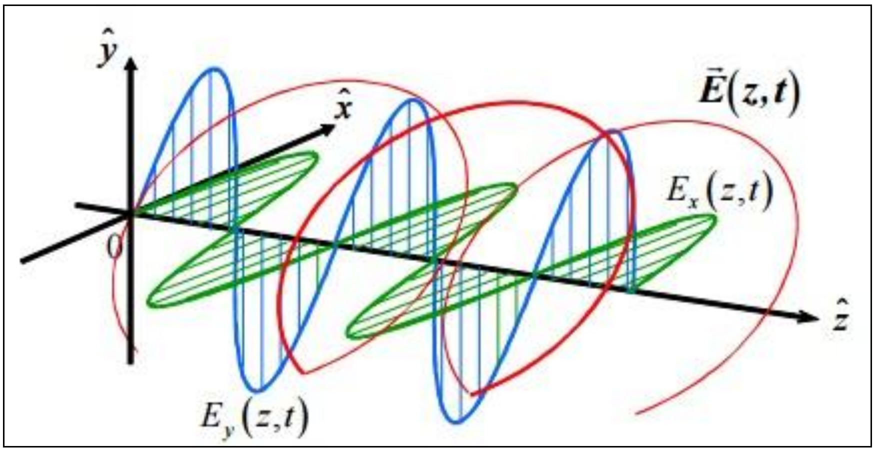

Figure 23 - Spatial evolution of a circularly polarized plane wave (López-Martínez C. 2005)

The wave rotates circularly around the $\hat{z}$ axis.

Elliptic polarization: Otherwise

The wave describes a helicoidal trajectory around the âxis

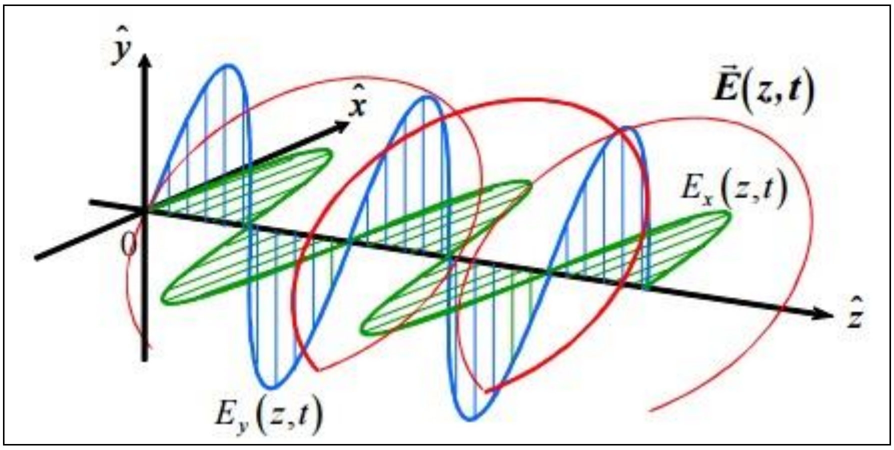

Figure 24 - Spatial evolution of an elliptically polarized plane wave (López-Martínez C. 2005)

.

Polarization ellipse

Geometrical description

The former paragraph introduced the spatial evolution of a plane monochromatic wave and showed that it follows a helicoidal trajectory along the axis. From a practical point of view, three-dimensional helicoidal curves are difficult to represent and to analyze. This is why a characterization of the wave in the time domain, at a fixed position, is generally preferred (López-Martínez C. 2005).

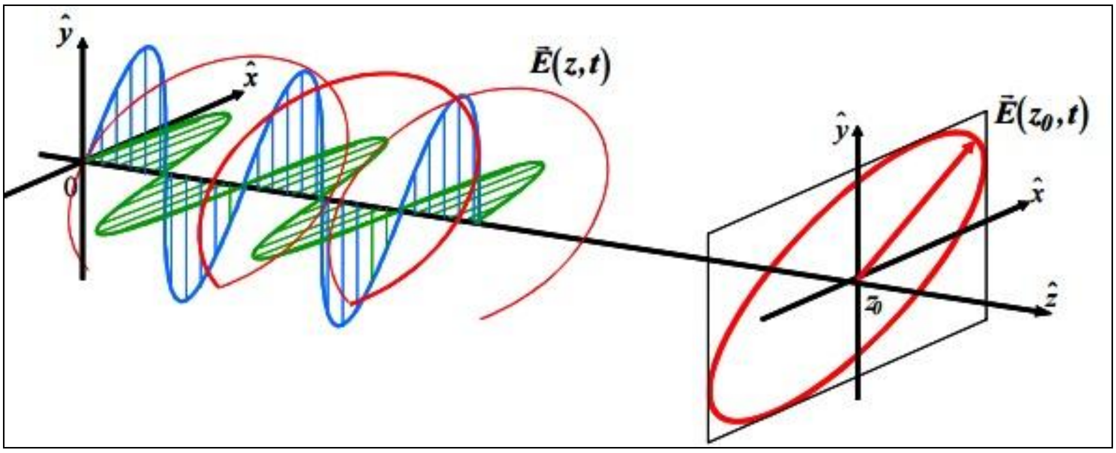

Figure 25 - Temporal trajectory of a monochromatic plane wave at a fixed abscissa z = z0 (López-Martínez C. 2005)

The temporal behavior is then studied within an equiphase plane, orthogonal to the direction of propagation and at a fixed location along the $\hat{z}$ axis. As time evolves, the wave propagates "through" equi-phase planes nd describe a characteristic elliptical

$\vec{E}$

locus as shown in zˆ Figure 5. The nature of the wave temporal trajectory may be determined from the following parametric relation between the components of (z_0,t) (López-Martínez C. 2005).

$$\left(\frac{E_x(z_0,t)}{E_{0x}}\right)^2 - 2\frac{E_x(z_0,t)E_y(z_0,t)}{E_{0x}E_{0y}}\cos(\delta_y-\delta_x)+\left(\frac{E_y(z_0,t)}{E_{0y}}\right)^2 = \sin(\delta_y-\delta_x)$$

The expression in (13) is the equation of an ellipse, called the polarization ellipse that describes the wave polarization.

The polarization ellipse shape may be characterized using 3 parameters as shown below.

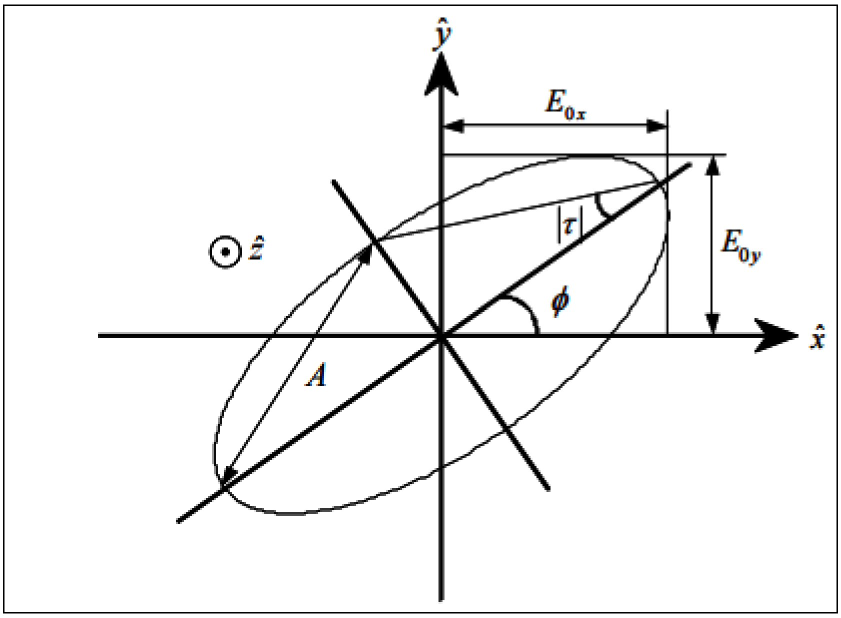

Figure 26 - Polarization ellipse (ESA Polarimetry Tutorial, 2005)

- A is called the ellipse amplitude and is determined from the ellipse axis as

$$A=\sqrt{E_{0x}^2+E_{0y}^2}$$

- $\phi \in \left[-\frac{\pi}{2},\frac{\pi}{2}\right]$ is the ellipse orientation and is defined as the angle between the ellipse major axis and $\hat{x}$

$$\tan 2\phi = 2\frac{E_{0x}E_{0y}}{E_{0x}^2-E_{0y}^2}\cos\delta \quad \text{with} \quad \delta=\delta_y-\delta_x$$

- $|\tau| \in \left[0,\frac{\pi}{4}\right]$ is the ellipse aperture, also called ellipticity, defined as

$$|\sin 2\tau| = 2\frac{E_{0x}E_{0y}}{E_{0x}^2 + E_{0y}^2}|\sin\delta|$$

<u>Sense of rotation</u>

As time elapses, the wave vector $\vec{E}(z_0,t)$ rotates in the $(\hat{x},\hat{y})$ to describe the polarization ellipse. The time-dependent orientation of $\vec{E}(z_0,t)$ with respect to, $\hat{x}$ named $\xi(t)$ is shown below.

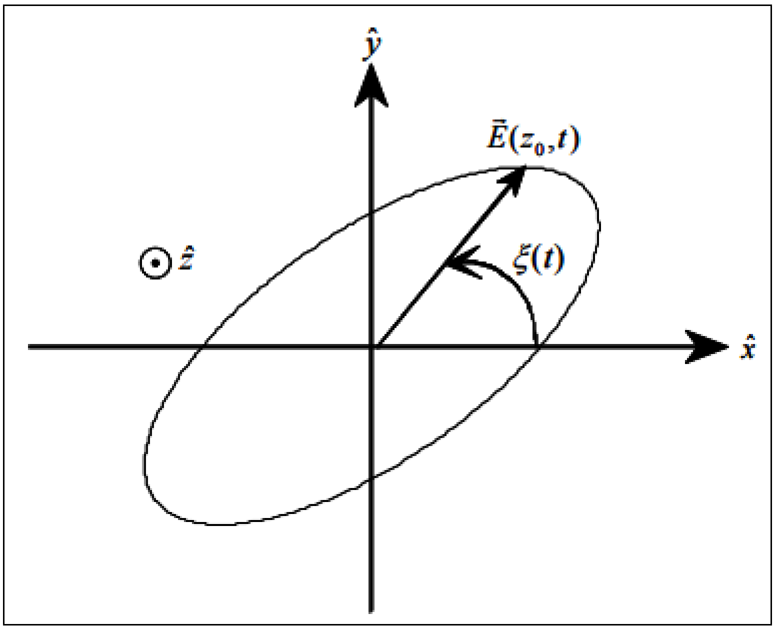

Figure 27 - Time-dependant rotation of $\vec{E}(z_0,t)$

(ESA Polarimetry Tutorial, 2005)

The time-dependent angle may be defined from the components of the wave vector in order to determine its sense of rotation.

$$\tan\xi(t) = \frac{E_y(z_0,t)}{E_x(z_0,t)} = \frac{E_{0y}\cos(\omega t - kz_0 + \delta_y)}{E_{0x}\cos(\omega t - kz_0 + \delta_x)}$$

The sense of rotation may then be related to the sign of the variable τ

$$\frac{\partial\xi(t)}{\partial t} \propto -\sin\delta \Rightarrow sign\left(\frac{\partial\xi(t)}{\partial t}\right) = -sign(\tau) \text{ with } \sin 2\tau = 2\frac{E_{0x}E_{0y}}{E_{0x}^2 + E_{0y}^2}\sin\delta$$

By convention, the sense of rotation is determined while looking in the direction of propagation. A right hand rotation corresponds then to

$$\frac{\partial\xi(t)}{\partial t} > 0 \Rightarrow (\tau,\delta) < 0$$

whereas a left hand rotation is characterized by

$$\frac{\partial\xi(t)}{\partial t} < 0 \Rightarrow (\tau,\delta) > 0$$

Below, the figure provides a graphical description of the rotation sense convention.

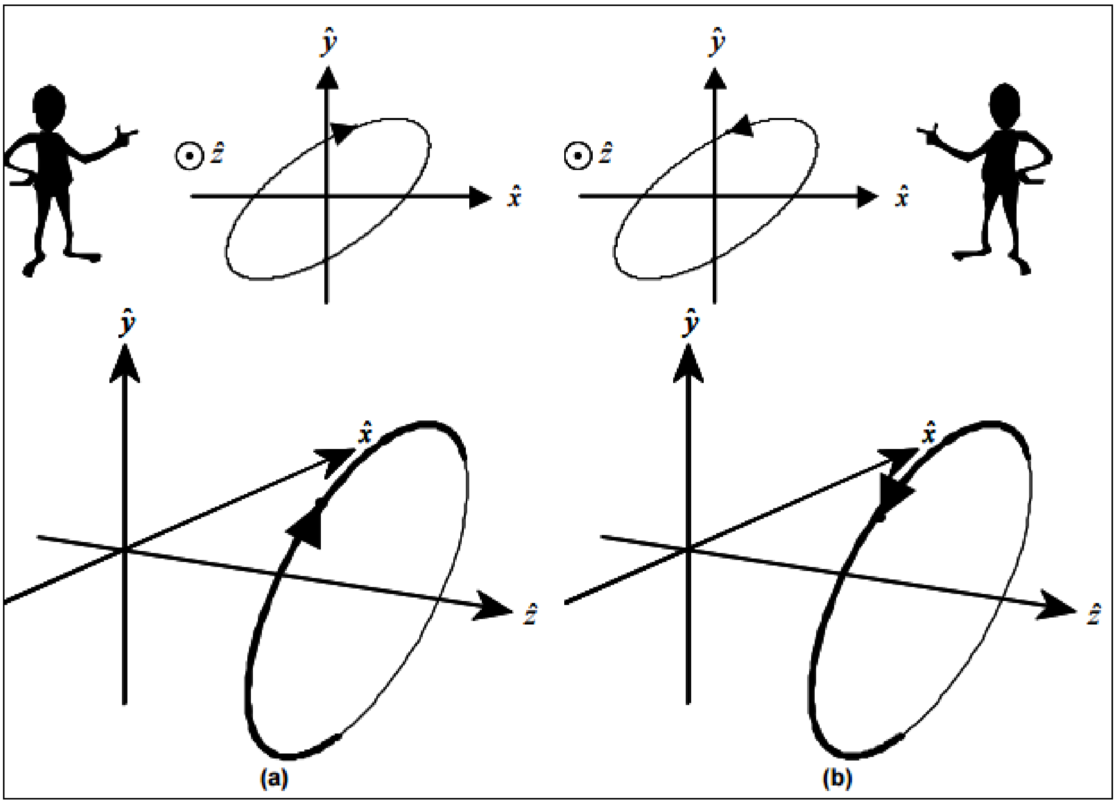

Figure 28 - (a) Left hand elliptical polarizations. (b) Right hand elliptical polarizations (ESA Polarimetry Tutorial, 2005)

<u>Quick estimation of a wave polarization state</u>

A wave polarization is completely defined by two parameters derived from the polarization ellipse

- Its orientation, $\phi \in \left[-\frac{\pi}{2}, \frac{\pi}{2}\right]$
- Its ellipticity $\tau \in \left[-\frac{\pi}{4}, \frac{\pi}{4}\right]$, with *sign*($\tau$) indicating the sense of rotation

The ellipse amplitude A can be used to estimate the wave power density.

The following procedure provides a quick (calculation free) way to roughly estimate a wave polarization.

Three cases may be discriminated from the knowledge of $\delta = \delta_y - \delta_x$, E_{0x}, E_{Oy}

$\delta = 0, \pi$

The polarization is linear since $\tau = 0$ and the orientation angle is given by

$$\phi = \tan^{-1}\left(\frac{E_{0y}}{E_{0x}}\right) \text{ if } \delta = 0 \text{ and } \qquad \phi = -a\tan\left(\frac{E_{0y}}{E_{0x}}\right) \text{ if } \delta = \pi$$

$$\delta = \pm\frac{\pi}{2} \quad \text{and } E_{0x} = E_{0y}$$

The polarization is circular, since $\tau = \pm\frac{\pi}{4}$ and the sense of rotation is given by *sign* (δ).

If $\delta < 0$, the polarization is right circular, whereas for $\delta > 0$ the polarization is left circular.

• Otherwise

If $\delta < 0$, the polarization is right elliptic, whereas for $\delta > 0$ the polarization is left elliptic.

Canonical polarization states

In practice the axes $\hat{x}$ and $\hat{y}$ are generally referred to as the horizontal, $\hat{h}$ and vertical $\hat{v}$ directions (López-Martínez C. 2005).

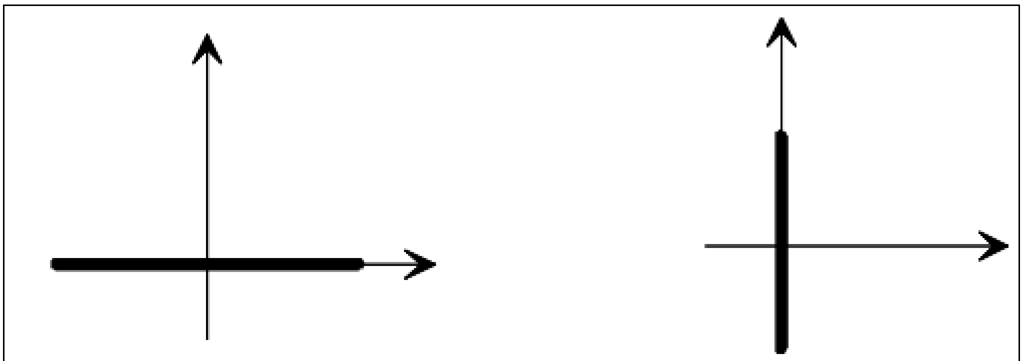

Figure 29 – (a) Horizontal polarization (b) Vertical polarization (ESA Polarimetry Tutorial, 2005)

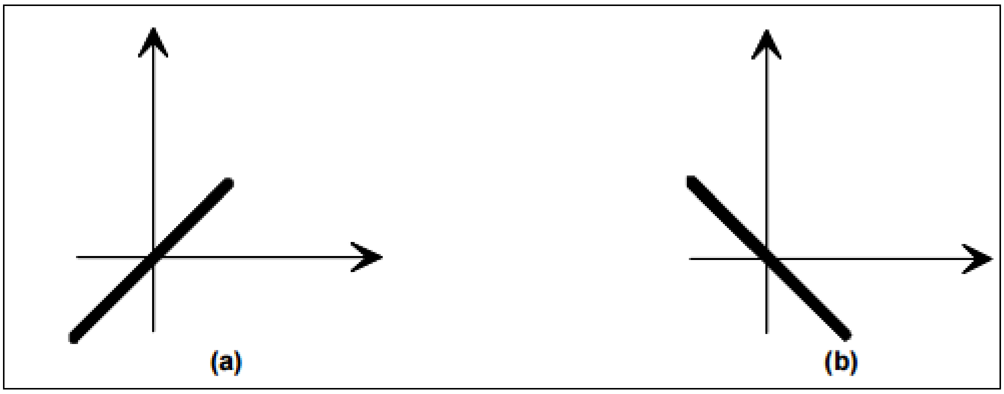

Figure 30 – (a) Right circular polarization. (b) Left circular polarization (ESA Polarimetry Tutorial, 2005)

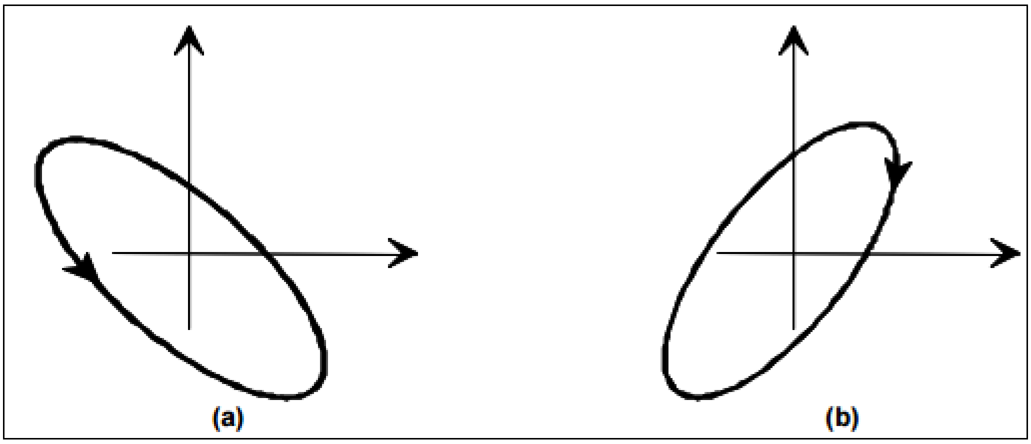

Figure 31 – (a) Right elliptical –45o polarization. (b) Left elliptical +45o polarization (ESA Polarimetry Tutorial, 2005)

15.2 SAR Polarimetry

<u>Wave Polarimetry</u>

Polarimetry refers specifically to the vector nature of the electromagnetic waves, whereas radar polarimetry is the science of acquiring, processing and analyzing the polarization state of an electromagnetic wave in radar applications (López-Martínez C. 2005).

This section summarizes the main theoretical aspects necessary for a correct processing and interpretation of the polarimetric information. As a result, the first part presents the so called wave polarimetry that deals with the representation and the understanding of the polarization state of an electromagnetic wave. The second part introduces the concept of scattering polarimetry. This concept collects the topic of inferring the properties of a given target, from a polarimetric point of view, given the incident and the scattered polarizes electromagnetic waves (López-Martínez C. 2005).

Electromagnetic Waves and Polarization

The generation, the propagation, as well as the interaction with matter of the electric and the magnetic fields $\vec{\mathbf{E}}(\vec{\mathbf{r}},t)$ are governed by the Maxwell's equations. In the most general case, these fields may present any spatial, i.e., $\vec{\mathbf{r}}$, and any time, i.e., *t*, dependence (López-Martínez C. 2005).

Nevertheless, the interest is on the special case of constant amplitude monochromatic plane fields which is adapted to the analysis of a wave polarization. In this particular case, the electromagnetic fields that shall be considered to be time-harmonic, i.e., the fields present a time dependence of the type $e^{j\omega t}$, where $\omega = 2\pi f$ is the angular frequency and f is the time frequency. In order to simplify the following analysis, this time dependence can be removed by considering the electric and the magnetic fields, for a specific time and a particular point in the space, in the following way

$$\vec{\mathbf{E}}(\vec{\mathbf{r}},t) = \Re\left\{\underline{\vec{\mathbf{E}}}(\vec{\mathbf{r}})e^{j\omega t}\right\}$$

$$\vec{\mathbf{H}}(\vec{\mathbf{r}},t) = \Re\left\{\underline{\vec{\mathbf{H}}}(\vec{\mathbf{r}})e^{j\omega t}\right\}$$

Where $\Re\{\cdot\}$ denotes the real part and $\underline{\vec{\mathbf{E}}}(\vec{\mathbf{r}})$ and $\underline{\vec{\mathbf{H}}}(\vec{\mathbf{r}})$ represent the time independent complex electric and magnetic field amplitudes, respectively, or simply complex amplitudes. Considering a source free, lossless, isotropic media, the expressions for the electric and magnetic complex fields can be of different form, leading for instance to: travelling waves, standing waves, evanescent waves and attenuating travelling and standing waves (López-Martínez C. 2005). Nevertheless, the interest is on travelling waves of the form:

$$\underline{\vec{\mathbf{E}}}(\vec{\mathbf{r}}) = \underline{\mathbf{E}}_0^{+}e^{-j\vec{\mathbf{k}}\cdot\vec{\mathbf{r}}} + \underline{\mathbf{E}}_0^{-}e^{j\vec{\mathbf{k}}\cdot\vec{\mathbf{r}}}$$

$$\underline{\vec{\mathbf{H}}}(\vec{\mathbf{r}}) = \underline{\mathbf{H}}_0^{+}e^{-j\vec{\mathbf{k}}\cdot\vec{\mathbf{r}}} + \underline{\mathbf{H}}_0^{-}e^{j\vec{\mathbf{k}}\cdot\vec{\mathbf{r}}}$$

In the previous two equations, the terms in $e^{-j\vec{\mathbf{k}}\cdot\vec{\mathbf{r}}}$ must be considered as travelling waves propagating in the positive sense of the direction of the vector $\vec{\mathbf{k}}$, whereas the terms in $e^{-j\vec{\mathbf{k}}\cdot\vec{\mathbf{r}}}$ represent travelling waves propagating in the negative sense of $\vec{\mathbf{k}}$. The vector $\vec{\mathbf{k}}$ receives the name of propagating vector, which amplitude is the wave number ***k*** .
Without loss of generality, considering the propagation of a time-harmonic field in an infinite (unbounded) media, it can be assumed that $\underline{\mathbf{H}}_0^{-} = 0$ and $\underline{\mathbf{E}}_0^{-} = 0$. In the particular case of an infinite, source free, lossless, isotropic media, and considering the solutions of the wave equations in, *Transverse Electromagnetic* (TEM) waves, or modes, propagating along a particular direction shall be considered. The most important characteristic of TEM waves is that, both the electric $\underline{\vec{\mathbf{E}}}(\vec{\mathbf{r}})$ and the magnetic $\underline{\vec{\mathbf{H}}}(\vec{\mathbf{r}})$ fields, at every point in space are contained in a local plane, which is independent of time. Without any other restriction, this plane may change from one point to another. If the space orientation of the planes where the fields are contained for a TEM mode is the same, that is, the planes are parallel, then the fields form *plane waves*. If in addition to having planar equiphases, the field has

equiamplitude planar surfaces, that is, the amplitude is the same over each plane, then it is called uniform plane wave. The planar nature of a wave can be also observed with the fact that the complex term $e^{-j\vec{\mathbf{k}}\cdot\vec{\mathbf{r}}}$ of the electric and magnetic fields is constant in a plane. TEM waves are not restricted to be planar. For instance, when the phase term $e^{-j\vec{\mathbf{k}}\cdot\vec{\mathbf{r}}}$ is constant in a sphere, the wave is referred to as *spherical wave*. In this situation, the local plane where the electric and magnetic fields are concentrated is tangent to the sphere where $e^{-j\vec{\mathbf{k}}\cdot\vec{\mathbf{r}}}$ is constant.

Finally, it must be mentioned that for the TEM fields in source free, lossless, isotropic media, the magnetic field $\underline{\vec{\mathbf{H}}}(\vec{\mathbf{r}})$ can be directly obtained from the electric field $\underline{\vec{\mathbf{E}}}(\vec{\mathbf{r}})$, provided the propagation vector $\hat{\mathbf{k}}$, as follows:

$$\underline{\vec{\mathbf{H}}}(\vec{\mathbf{r}}) = \sqrt{\frac{\mu}{\varepsilon}}\hat{\mathbf{k}} \times \underline{\vec{\mathbf{E}}}(\vec{\mathbf{r}})$$

That is, at any point of the space $\vec{\mathbf{r}}$, the electric and magnetic fields are perpendicular vectors that lie in a plane normal to the propagation direction.

The electric and magnetic waves considered until now, $\underline{\vec{\mathbf{E}}}(\vec{\mathbf{r}})$ and $\underline{\vec{\mathbf{H}}}(\vec{\mathbf{r}})$ are vector quantities. Consequently, the description of these waves must be performed considering a particular coordinate system. The most common coordinate systems employed to describe electromagnetic waves are the rectangular or cartesian, the cylindrical and the spherical coordinate systems. The selection of one of these is normally driven by the geometry of the particular problem under consideration, as the selection of the right coordinate system simplifies the analytical expressions of the electromagnetic waves.

The rectangular coordinate system, represented by the three orthonormal vectors $\{\hat{\mathbf{x}}, \hat{\mathbf{y}}, \hat{\mathbf{z}}\}$, is employed to simplify the electromagnetic wave description when propagation is considered in an infinite lossless, isotropic media. Without loss of generality, it is possible to assume the propagation vector parallel to $\hat{\mathbf{z}}$. Therefore, the electric and magnetic fields lie in the $\{\hat{\mathbf{x}}, \hat{\mathbf{y}}\}$ plane (López-Martínez C. 2005).

Thus, the fields may be decomposed as:

$$\underline{\vec{\mathbf{E}}}(\vec{\mathbf{r}}) = E_{0x}e^{-jkz}\hat{\mathbf{x}} + E_{0y}e^{-jkz}\hat{\mathbf{y}}$$

$$\underline{\vec{\mathbf{H}}}(\vec{\mathbf{r}}) = H_{0x}e^{-jkz}\hat{\mathbf{x}} + H_{0y}e^{-jkz}\hat{\mathbf{y}}$$

where E_{0x}, E_{0y}, H_{0x} and H_{0y} are the complex amplitudes of the fields in each coordinate, which shall be considered constant.

As shown, for a TEM electromagnetic wave propagating in an infinite, lossless, isotropic media, the electric and the magnetic fields lie in a plane orthogonal to the direction of propagation. Consequently, and as observed in and, the electric field vector (and the magnetic field vector) can be decomposed into two orthogonal components, $\hat{\mathbf{x}}$ and $\hat{\mathbf{y}}$ in the previous case. In this framework, polarization refers to the vector nature of the electromagnetic waves (López-Martínez C. 2005).

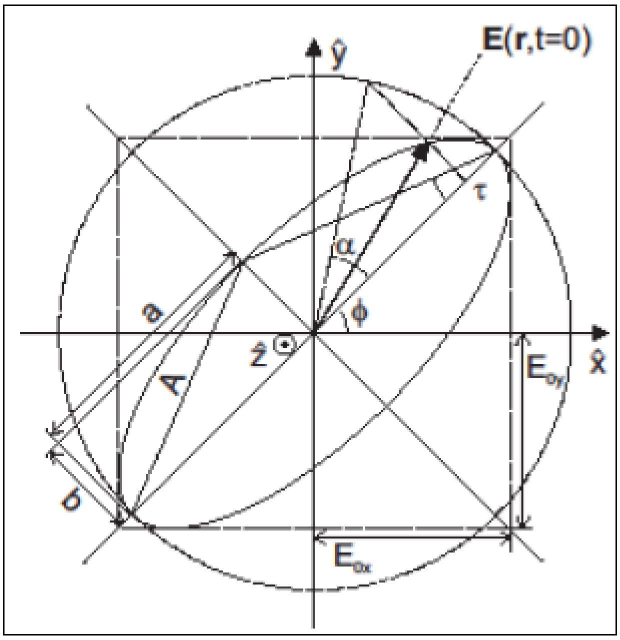

Figure 32 - Polarization ellipse
(ESA Polarimetry Tutorial)

According to the *IEEE Standard definitions for Antennas*, the polarization of a radiated wave is defined as that property of the radiated electromagnetic wave describing a time-varying direction and relative magnitude of the electric field vector; specifically, the figure traced as a function of time by the extremity of the vector at a fixed location in space, and the sense in which it is traced, as observed along the direction of propagation. Hence, polarization is the curve traced out by the end point of the arrow representing the instantaneous electric field (López-Martínez C. 2005).

16. SOFTWARE

16.1 SENTINEL-1 Toolbox

The SENTINEL-1 Toolbox (S1TBX) consists of a collection of processing tools, data product readers and writers and a display and analysis application to support the large archive of data from ESA SAR missions including SENTINEL-1, ERS-1 & 2 and ENVISAT, as well as third party SAR data from ALOS PALSAR, TerraSAR-X, COSMO-SkyMed and RADARSAT-2. The various processing tools could be run independently from the command-line and also integrated within the graphical user interface. The Toolbox includes tools for calibration, speckle filtering, coregistration, orthorectification, mosaicking, data conversion, polarimetry and interferometry.

The SENTINEL-1 Toolbox is being developed for ESA by Array in partnership with DLR, Brockmann Consult and OceanDataLab (SENTINEL-1 Toolbox ESA 2015).

16.2 PolSAR pro

The Polarimetric SAR Data Processing and Educational Tool aims to facilitate the accessibility and exploitation of multi-polarised SAR datasets including those from ESA (Envisat ASAR Alternating Polarisation mode products and Sentinel-1) and Third Party Missions (ALOS-1 PALSAR, ALOS-2 PALSAR, COSMO-SkyMed, RADARSAT-2, RISAT, TerraSAR-X and Tandem-X).

A wide-range of tutorials and comprehensive documentation provide grounding in polarimetry and polarimetric interferometry necessary to stimulate research and development of scientific applications that utilize such techniques; the toolbox of processing functions offers users the capability to implement them.

PolSARpro is developed under contract with ESA since 2003 where the initiative was a direct result of recommendations made during the first PolInSAR Workshop held at ESRIN in 2003. The **IETR (***Institute of Electronics and Telecommunications of Rennes* ***- UMR CNRS 6164***) of the **University of Rennes 1**, France is in charge of the development of the PolSARpro software.

All elements of the PolSARpro project are distributed by ESA free of charge, including the source code (ESA, 2016).

16.3 Map Ready

The MapReady Remote Sensing Tool Kit accepts level 1 detected SAR data, single look complex SAR data, and optical data from ASF (Alaska Satellite Facility) and some other facilities. It can terrain correct, geocode, apply polarimetric decompositions to multi-pol SAR data, and save to several common imagery formats including GeoTIFF. Other software included in the package are an image viewer, metadata viewer, a projection coordinate converter, and a variety of command line tools (Alaska Satellite Facility, 2016). Map Ready is installed with PolSARpro installation and they work in cooperation.

16.4 ArcMAP

ArcGIS and its tool ArcMAP is a GIS software that provides the user with a plenty of capabilities since it can create maps, apply cartographical and geographical analysis, create simulations models over many earth phenomena, process statistical geodata and many more. In this study, we used ArcMAP for creating the final maps.

16.5 ERDAS Imagine

ERDAS Imagine is a raster-based software package designed specifically to extract information from imagery.

ERDAS IMAGINE provides true value, consolidating remote sensing, photogrammetry, LiDAR analysis, basic vector analysis, and radar processing into a single product. (Hexagon Geospatial, 2015). This software is appropriate for Image analysis, remote sensing, GIS, High-performance terrain preparation, mosaicking and many others.

A geographic imaging toolset that extends the capabilities of IMAGINE Essentials by adding more precise mapping with sensor model support and geospatial data processing functions (Hexagon Geospatial, 2015).

In this study we used this software for interpretation of the final Envisat data and see the time change over the study area.

17. DATASET

17.1 ENVISAT Satellite

The first data that we got were of Envisat satellite. A system that belongs to ESA's fleet. Actually, Envisat was ESA's successor to ERS. Envisat was launched in 2002 with 10 instruments aboard and at eight tons is the largest civilian Earth observation mission (ESA Earth Online 2000-2016).

More advanced imaging radar, radar altimeter and temperature-measuring radiometer instruments extend ERS data sets. This was supplemented by new instruments including a medium-resolution spectrometer sensitive to both land features and ocean colour. Envisat also carried two atmospheric sensors monitoring trace gases (ESA Earth Online 2000-2016).

The Envisat mission ended on 08 April 2012, following the unexpected loss of contact with the satellite (ESA Earth Online 2000-2016).

In March 2002, the European Space Agency launched Envisat, an advanced polar-orbiting Earth observation satellite which provides measurements of the atmosphere, ocean, land, and ice (ESA Earth Online 2000-2016).

17.1.1 Operations

Envisat flies in a sun-synchronous polar orbit of about 800-km altitude. The repeat cycle of the reference orbit is 35 days, and for most sensors, being wide swath, it provides a complete coverage of the globe within one to three days. The exceptions are the profiling instruments MWR and RA-2 which do not provide real global coverage, but span a tight grid of measurements over the globe. This grid is the same 35-day repeat pattern which has been well established by ERS-1 and ERS-2 (ESA Earth Online 2000-2016).

In order to ensure an efficient and optimum use of the system resources and to guarantee the achievement of the mission objectives Envisat reference mission operation profiles are established and used for mission and system analyses to define the instrument operational strategies, the command and control, and the data transmission, processing and distribution scenarios (ESA Earth Online 2000-2016).

Mission and operation requirements

- Sun-synchronous polar orbit (SSO): Nominal reference orbit of mean altitude 800 km, 35 days repeat cycle, 10:00 AM mean local solar time (MLST) descending node, 98.55 deg. inclination.

- The orbit is controlled to a maximum deviation of +/- 1 km from ground track and +/- 5 minutes on the equator crossing MLST.

- Recording of payload data over each orbit for low bit rate (4.6 Mps) on tape recorders or solid state recorder (SSR).
- High rate data (ASAR and MERIS) to be accessible by direct telemetry or recording on SSR.

17.1.2 ASAR operation description

ASAR general operation strategy

ASAR offers, by exploiting the combinations of polarisations and incidence angles, 37 different and mutually exclusive operating modes in high-, medium- (wide swath mode), and reduced- (global monitoring mode) resolution. These modes will be operated mainly in response to user requests. Wave mode is also mutually exclusive with respect to all the other modes. It is a low-rate mode operated systematically over oceans as part of the global mission.
Global monitoring and wave modes are recorded systematically when operated. ASAR high- and medium-resolution imaging modes are either transmitted on a real time link (direct X-band or via Artemis Ka-band link) or recorded on the on-board solid state recorder for ground data recovery. The high- and medium-resolution data are acquired only when required to satisfy either a background mission scenario and/or user requests (ESA).

ASAR processing and data distribution

All ASAR high-rate data acquired by ESA facilities is systematically processed in near real time to generate medium-resolution products (around 150 m resolution) and browse products. Browse products are available on-line. High-resolution products are processed in near real time or off-line, upon user request. All medium- and high- resolution products are delivered to users on request either in near real time on a dissemination channel or off line on physical media (ESA Earth Online 2000-2016).

17.1.3 Envisat Orbit

Measurement patterns orbital parameters	
Orbits per Day	14 11/35
Repeat Cycle (days)	35
Orbits in Cycle	501
Orbit Period (min)	100.59
MLST at descending node	10:00
Inclination (deg)	98.55
Semi-Major Axis [Orbit Radius] (km)	7159.5
Orbit Velocity (km/s)	7.45
Mean Altitude (km)	799.8
Orbital Altitude Range (km)	780 - 820

Figure 33 - Orbit parameters of ENVISAT (ESA Earth Online 2000 – 2016)

Some of these are fundamental and have an impact on the overall concept of the system. In particular, the selection of a sun-synchronous orbit is of primary importance and has driven the physical configuration of the spacecraft. The gross altitude range, within some tens of kilometers of 800 km, is also critical to the design. After that, there is a certain degree of freedom in the choice of parameters (ESA Earth Online 2000-2016).

17.2 ENVISAT Instruments

Envisat satellite contains many instruments and more specifically it consists of: ASAR, MERIS, AATSR, RA-2, MWR, GOMOS, MIPAS, SCHIAMACHY, DORIS and LRR.

In this study we use ASAR data of Amazon rainforest. It is an Advanced Synthetic Aperture Radar (ASAR), operating at C-band, ASAR ensures continuity with the image mode (SAR) and the wave mode of the ERS-1/2 AMI (ESA Earth Online 2000-2016).

17.3 ASAR Instrument

An Advanced Synthetic Aperture Radar (ASAR), operating at C-band, ASAR ensures continuity with the image mode (SAR) and the wave mode of the ERS-1/2 AMI. It features enhanced capability in terms of coverage, range of incidence angles, polarisation, and modes of operation. This enhanced capability is provided by significant differences in the instrument design: a full active array antenna equipped with distributed transmit/receive modules which provides distinct transmit and receive beams, a digital waveform generation for pulse "chirp" generation, a block adaptive quantisation scheme, and a ScanSAR mode of operation by beam scanning in elevation.

Status	Not Operational
Type	Imaging microwave radars
Technical Characteristics	
Accuracy:	Radiometric resolution in range: 1.5-3.5 dB, Radiometric accuracy: 0.65 dB
Spatial Resolution:	Image, Wave and Alternating Polarisation modes: approx 30m x 30m.Wide Swath mode: approx 150m x 150m. Global Monitoring mode: approx1000m x 1000m.
Swath Width:	Image and alternating polarisation modes: up to 100km, Wave mode:5km, Wide swath and global monitoring modes: 400km or more
Waveband:	Microwave: C-band, with choice of 5 polarisation modes (VV, HH,VV/HH, HV/HH, or VH/VV)
Earth Topics	Land (Landscape Topography), Snow and Ice (Snow and Ice), Ocean and Coast (Ocean Currents and Topography)
Related Instruments	SAR, , L-band SAR, PALSAR, RLSBO, SAR (RADARSAT), SAR (RADARSAT-2), SAR (SAOCOM), TerraSAR-X

Figure 34 – Characteristics of ASAR instrument (ESA Earth Online 2000-2016).

17.3.1 Characteristics

The ASAR (Advanced SAR) instrument derives from the AMI istrument of ERS-1 and ERS-2. It measures the radar backscatter of the Earth's surface at C-band with a choice of five polarization modes: VV, HH, VV/HH, HV/HH, or VH/VV.

The resulting improvements in image and wave mode beam elevation steerage allow the selection of different swaths, providing a swath coverage of over 400-km wide using ScanSAR techniques.

The ASAR instrument is a phased array radar with 320 T/R-modules arranged across the antenna, such that by adjusting individual module phase and gain, the transmit and receive beams may be steered and configured.

The instrument comprises two major functional groups, the antenna subassembly (ASA) and the central electronics subassembly (CESA) with subsystems as shown in the functional block diagram. The active antenna contains 20 tiles with 16 T/R-modules each (ESA Earth Online 2000-2016).

17.3.2 Concept

ASAR consists of a coherent, active phased array SAR (i.e., distributed transmitter and receiver elements) which is mounted with the long axis of the antenna aligned with the satellite's flight direction (i.e., Y-axis). The SAR antenna with its two-dimensional beam pattern images a strip of ground to the right side of the flight path which has potentially unlimited content in the direction of motion (i.e., the azimuth direction) but is bounded in the orthogonal direction (i.e., the range direction) by the antenna elevation beamwidth. The objective of the SAR system is to produce a two-dimensional representation of the scene reflectivity at high resolution, with axes defined in the range and azimuth direction.

ASAR Stripmap Modes (Image, Wave)

When operating as a Stripmap SAR, the phased array antenna gives ASAR the flexibility to select an imaging swath by changing the beam incidence angle and the elevation beamwidth. In addition, the appropriate PRF required to ensure acceptable ambiguity performance and to suppress unwanted nadir returns is selected.

In the image mode, ASAR operates in one of seven predetermined swaths with either vertically or horizontally polarised radiation; the same polarisation is used for transmit and receive (i.e., HH or VV).

The wave mode uses the same swaths and polarisations as image mode. However, a continuous strip of data is not required. Instead, small areas of the ocean are imaged at regular intervals along the swath. This intermittent operation provides a low data rate, such that the data can be stored on board the satellite, rather than being downlinked immediately to the ground station.

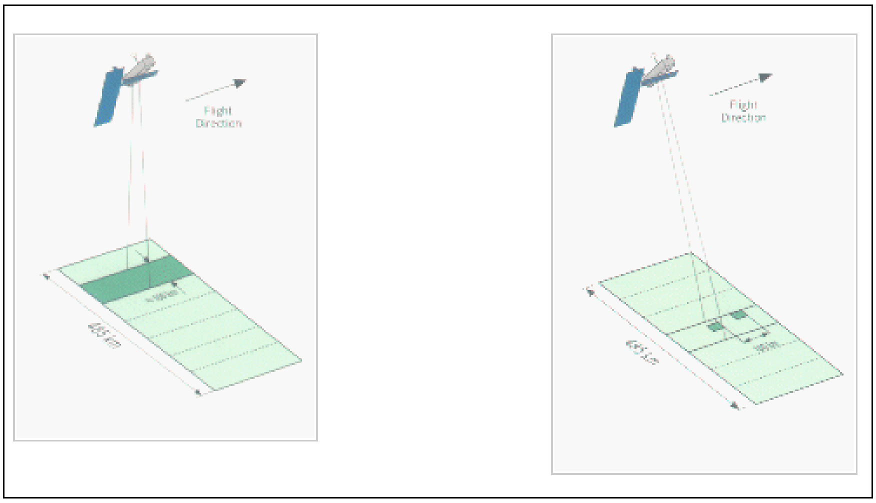

Figure 35 - ASAR Strimap modes
(ESA Earth Online 2000-2016)

<u>ASAR ScanSAR Modes: Wide swath, global monitoring, and alternating polarization</u>

ASAR operates according to the ScanSAR principle, as described above, in two measurement modes: the wide swath mode and global monitoring mode. These use five predetermined overlapping antenna beams which cover the wide swath.

An additional ASAR measurement mode, called alternating polarisation mode, which employs a modified ScanSAR technique, has also been defined. Instead of scanning between different elevation sub-swaths, the alternating polarization mode (co-polar) scans between two polarisations, HH and VV, within a single swath (which is preselected, as for image and wave modes). In addition, there are two cross-polar modes, where the transmit pulses are all H or all V polarisation, with the receive chain operating alternatively in H and V, as in the co-polar mode.

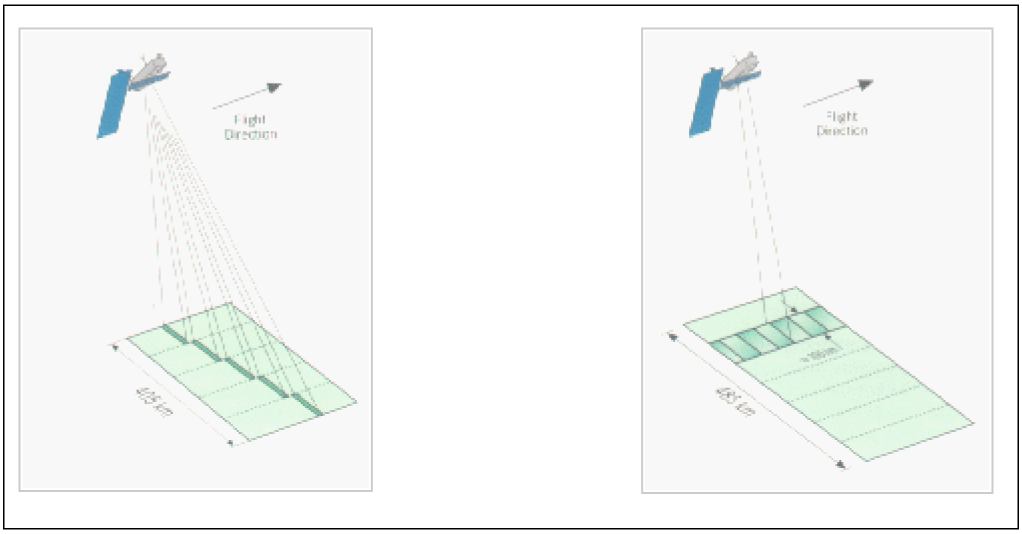

Figure 36 – ASAR ScanSAR modes (ESA Earth Online 2000-2016)

Instrument

The ASAR, operated at C-band (5.331 GHz), can be regarded as an advanced version of the SAR flying on ERS-1/2. It can be operated continuously for 30 minutes in a high-resolution mode for each orbit. Its application covers observations of land and sea characteristics under all weather conditions.

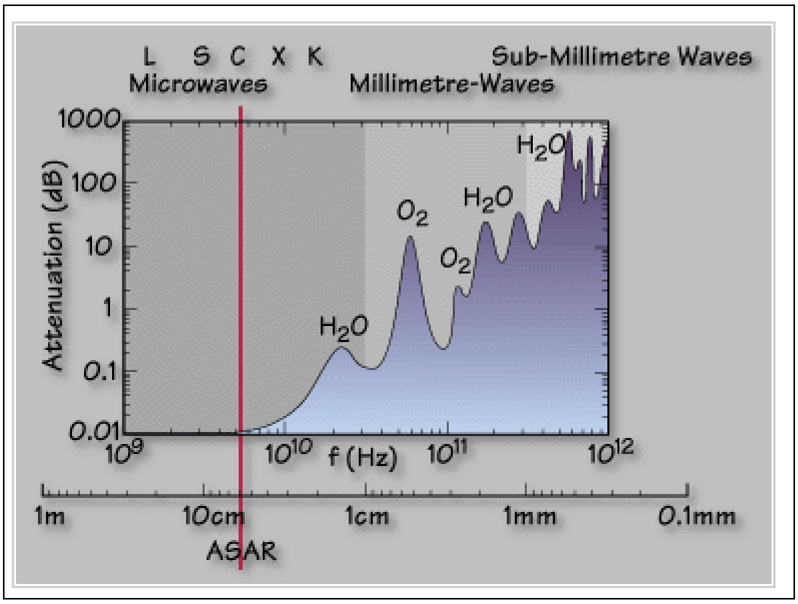

Figure 37 – Instrument (ESA Earth Online 2000-2016)

The ASAR, operated at C-band (5.331 GHz)

In order to provide the possibility to adapt to various observing requirements, ASAR incorporates the capabilities to steer the beam to image different swath positions. Additionally, imaging can be performed in horizontal and vertical polarization. These features provided by the active array antenna requires a dedicated calibration scheme. The table summarizes the ASAR capabilities (ESA Earth Online 2000-2016).

Instrument Parameters	Image Mode	Alternating Polarisation	Wide Swath	Global Monitoring	Wave Mode
Swath width	up to 100 km	up to 100 km	> 400 km	> 400 km	5 km vignette
Operation time	up to 30 min per orbit			rest of orbit	
Data Rate	up to 100 Mbit/s			0.9 Mbit/s	
Power	1365 W	1395 W	1200 W	713 W	647 W

Figure 38 – ASAR operated at C-band – characteristics (ESA Earth Online 2000-2016)

17.3.3 Operations

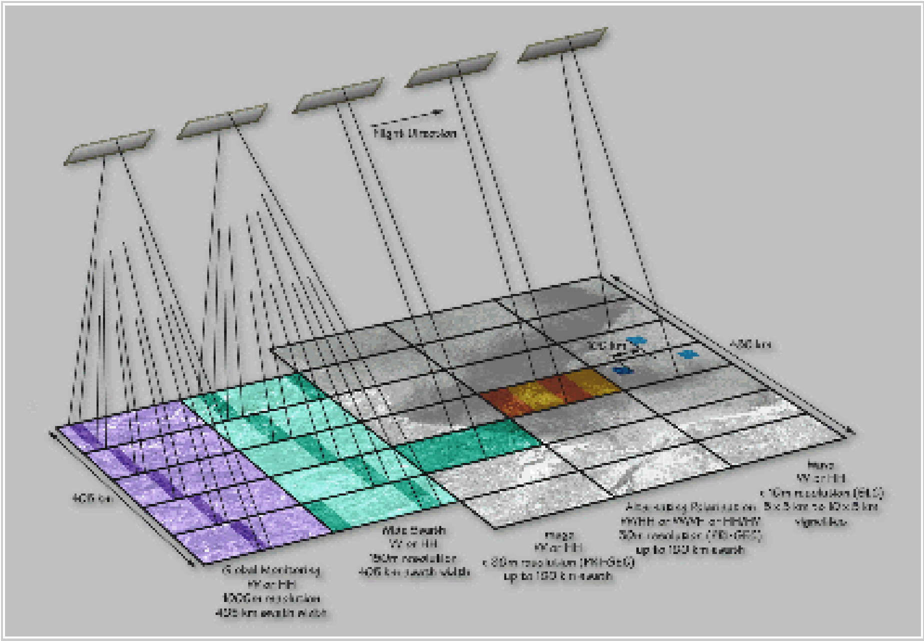

Figure 39 – ASAR's five mutually exclusive modes of operation (ESA Earth Online 2000-2016)

ASAR has five mutually exclusive modes of operation. **Global Monitoring Mode (GM)** where low resolution images (1 km) are provided using ScanSAR technique over a 405 km swath at HH or VV polarisation, **Wave Mode (WM)** where the ASAR instrument measures changes in backscatter from the sea surface due to ocean wave action, **Alternating Polarization (AP) Modeprovides** resolution products in any swath as in Image Mode but with polarisation changing from subaperture to subaperture within the synthetic aperture, **Wide Swath Mode (WS)** where the ScanSAR technique is used providing images of a wider strip (405 km) with medium resolution (150 m) in HH or VV polarization. Concluding, **Image Mode (IM)**, the data type that were used in this study are generated high spatial resolution products (30 m) similar to the ERS SAR. It images one of the seven swaths located over a range of incidence angles spanning from 15 to 45 degrees in HH or VV polarization. In the table below the range of the values is due to the different orbit positions. The values are given for Level 1b products (ESA Earth Online 2000-2016).

17.3.4 Calibration

The objective of the ASAR instrument internal calibration scheme is to derive the instrument internal path transfer function, and to perform noise calibration. This objective is realised by dedicated calibration signal paths and special calibration pulses within the instrument for making the required calibration measurements and by using these measurements to perform corrections within the ground processor (ESA Earth Online 2000-2016).

17.3.5 Applications

ASAR data have many applications in many fields like: Oceans & Coast, Land, Natural Disasters, Snow & Ice (ESA Earth Online 2000-2016).

Regarding the Land category there are numerous applications where the Advanced Synthetic Aperture Radar (ASAR) sensor is used for. Some of them are:

- Global Vegetation Monitoring
- Forestry
- Geology and Topography
- Agriculture
- Natural Hazards
- Flooding, Hydrology and Water Management
- Urban Studies

Forestry is a special category of Land-based applications of ASAR instrument. In this Thesis we use ASAR data for studying a part of Brazilian Amazon rainforest.

The multipolarisation, multi-swath modes of ASAR offer a greatly enhanced capability for forest assessment over any previous spaceborne SAR mission. New research being proposed brings together expertise in SAR data, software, ecology, and forestry, as well as a long history of ground data. The application of ASAR to the quantitative assessment of forest characteristics such as yield, species, and phenology will be demonstrated for tropical, boreal and temperate forests.

ENVISAT's ASAR instrument is able to distinguish between different vegetation types, i.e. arable land, pasture or forest. Comparing images taken at different times can help in damage assessment (ESA Earth Online 2000-2016).

17.4 ENVISAT Dataset

We used 10 images of **IM** type covering a large area of Amazon rainforest in Brazil territories. 10 ENVISAT ASAR.PRI ascending scenes, of VV polarization, swath IS2, track 131 covering the period 2004-The study area contains the state of Tocantins. You can see in the map above. The images are of 2004, 2005 and 2006 years (tables 3 & 4). Four of them were used for multitemporal analysis as they refer to different years while the rest of them were used for seasonal study as they have been collected the same year but different month. It is very important to say that all of the 11 images cover exactly the same area.

ENVISAT- ASAR IMAGES	DATE
ASA_IMP_1PNUPA20040805_013442_000000162029_00131_12710_4266.N1	5/8/2004
ASA_IMP_1PNUPA20050512_013444_000000162037_00131_16718_4268.N1	12/5/2005
ASA_IMP_1PNUPA20060427_013433_000000162047_00131_21728_4272.N1	27/4/2006
ASA_IMP_1PNUPA20060427_013433_000000162047_00131_21728_4272.N1	10/8/2006

Table 3 – Envisat ASAR images (4 in number) used for the multitemporal analysis

ENVISAT- ASAR IMAGES	DATE
ASA_IMP_1PNUPA20060112_013427_000000162044_00131_20225_4269.N1	12/1/2006
ASA_IMP_1PNUPA20060216_013430_000000162045_00131_20726_4275.N1	16/2/2006
ASA_IMP_1PNUPA20060323_013427_000000162046_00131_21227_4271.N1	23/3/2006
ASA_IMP_1PNUPA20060427_013433_000000162047_00131_21728_4272.N1	27/4/2006
ASA_IMP_1PNUPA20060601_013434_000000162048_00131_22229_4273.N1	1/6/2006
ASA_IMP_1PNUPA20060706_013440_000000162049_00131_22730_4274.N1	1/7/2006
ASA_IMP_1PNUPA20060810_013440_000000162050_00131_23231_4270.N1	10/8/2006

Table 4 - Envisat ASAR images (7 in number) used for the seasonal analysis

17.5 ALOS Satellite

The Japanese Earth observing satellite program consists of two series: those satellites used mainly for atmospheric and marine observation, and those used mainly for land observation. The Advanced Land Observing Satellite (ALOS) follows the Japanese Earth Resources Satellite-1 (JERS-1) and Advanced Earth Observing Satellite (ADEOS) and will utilize advanced land-observing technology. ALOS will be used for cartography, regional observation, disaster monitoring, and resource surveying (JAXA 2014).

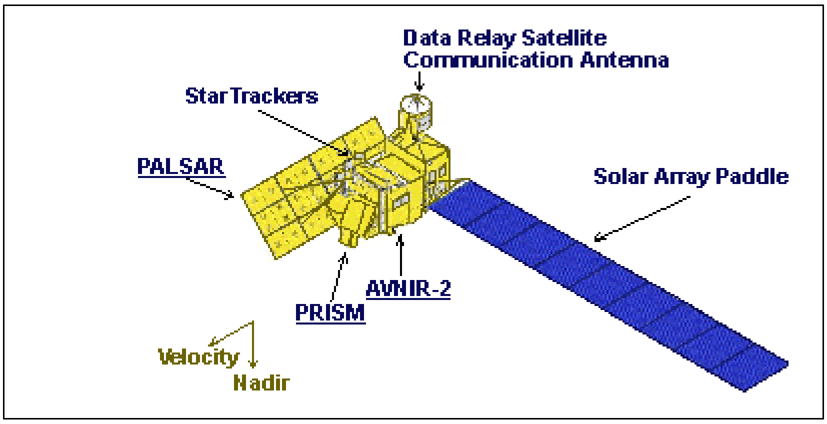

Figure 40 – ALOS Satellite - Instruments (ESA Earth Online 2000-2016)

The ALOS has three remote-sensing instruments: the Panchromatic Remote-sensing Instrument for Stereo Mapping (PRISM) for digital elevation mapping, the Advanced Visible and Near Infrared Radiometer type 2 (AVNIR-2) for precise land coverage observation, and the Phased Array type L-band Synthetic Aperture Radar (PALSAR) for day-and-night and all-weather land observation. In order to utilize fully the data obtained by these sensors, the ALOS was designed with two advanced technologies: the former is the high speed and large capacity mission data handling technology, and the latter is the precision spacecraft position and attitude determination capability. They will be essential to high-resolution remote sensing satellites in the next decade. ALOS have been successfuly launched on an H-IIA launch vehicle from the Tanegashima Space Center, Japan (JAXA 2014).

Launch Date	Jan. 24, 2006
Launch Vehicle	H-IIA
Launch Site	Tanegashima Space Center
Spacecraft Mass	Approx. 4 tons
Generated Power	Approx. 7 kW (at End of Life)
Design Life	3 -5 years
Orbit	Sun-Synchronous Sub-Recurrent
	Repeat Cycle: 46 days Sub Cycle: 2 days
	Altitude: 691.65 km (at Equator)
	Inclination: 98.16 deg.
Attitude Determination Accuracy	2.0×10^{-4} degree (with GCP)
Position Determination Accuracy	1m (off-line)
Data Rate	240Mbps (via Data Relay Technology Satellite) 120Mbps (Direct Transmission)
Onboard Data Recorder	Solid-state data recorder (90Gbytes)

Figure 41 – ALOS Characteristics (JAXA 2014)

17.5.1 ALOS Mission Concept

To help resolve local issues such as food security, water resource scarcity, disaster prevention and biological diversity conservation that also require support and collaboration from the global viewpoint, what kinds of data should be developed.

Information on current status and changes of environmental resources such as soil, water, and vegetation (from forest to farmland) are the basis in analyzing these issues. Though quality of soil may not be easy to acquire by remote sensing, risk of soil degradation caused by erosion is governed by climatic and topographical factors. Regarding water circulation and vegetation, climatic and topographical factors are dominant as well. It is also the case with disaster risks. Of course, information on how people use land (land use Information) is indispensable. Although the climate data may be excluded just because it cannot be directly observed from satellite, it could be concluded that topographic information would be the core part of the common information basis.

Furthermore, ALOS contributes to many sectors:

Generate topographic data as SDI (Spatial Data Infrastructure) at the global scale.

DEM (Digital Elevation Model) data with less than 5-meter errors and with 10 meter grid spacing will be developed. Satellite imagery has advantages in generating DEM of this level, because the measurement techniques are relatively established and elevation data are not likely to change so frequently. By overlaying high-resolution optical sensor data and SAR data on the derived DEM, information on environmental resources like vegetation and soil can be provided. For the areas where the DEM was already developed, we can focus on changes of land surfaces. Combination of DEM and satellite imagery will contribute to the development of global spatial data infrastructure.

Support "sustainable" development at local to regional scale through monitoring global environmental resources

In addition to the global spatial data Infrastructure, a variety of information on environmental resources provided through ALOS mission can help conservation of environmental resources and sustainable development at the local to regional scale.

Monitor major disasters at the global scale

Disaster such as drought, volcanic explosion and flooding can threaten sustainable and stable regional development. Being integrated with the other satellites and monitoring systems, ALOS will provide information on major disasters.

Exploration of non-renewable resources

In parallel with the monitoring of land and water related resources, ALOS mission will provide information for exploring non-renewable resources to support regional development.

Technological development for the future earth observation

ALOS is almost a single satellite, which aim at global observation with high-resolution sensors. It poses many challenging research and development topics for sensor development and data processing, which will make significant contributions to the development of next generation earth observation technologies (JAXA 2014).

17.5.2 Goals of ALOS Research Plan

To achieve the ALOS mission, it is essential not only to distribute data products to users, but also to promote scientific and utilization research for ALOS data in broad categories ranging from the environmental and resource sciences to computer science. This Plan suggests research categories that are strongly related to acquisition and application of ALOS data and that will be promoted by association and efforts of PIs in this RA and EORC (JAXA).

17.5.3 PALSAR Instrument

The Phased Array type L-band Synthetic Aperture Radar (PALSAR) is an active microwave sensor using L-band frequency to achieve cloud-free and day-and-night land observation. It provides higher performance than theJERS-1's synthetic aperture radar (SAR). Fine resolution in a conventional mode, but PALSAR will have another advantageous observation mode. ScanSAR, which will enable us to acquire a 250 to 350km width of SAR images (depending on the number of scans) at the expense of spatial resolution. This swath is three to five times wider than conventional SAR images. The development of the PALSAR is a joint project between JAXA and the Japan Resources Observation System Organization (JAROS).

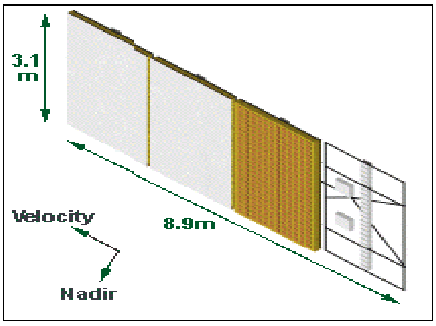

Figure 42 – PALSAR Instrument (JAXA 2014)

Mode	Fine		ScanSAR	Polarimetric (Experimental mode)*1
Center Frequency	1270 MHz(L-band)			
Chirp Bandwidth	28MHz	14MHz	14MHz,28MHz	14MHz
Polarization	HH or VV	HH+HV or VV+VH	HH or VV	HH+HV+VH+VV
Incident angle	8 to 60deg.	8 to 60deg.	18 to 43deg.	8 to 30deg.
Range Resolution	7 to 44m	14 to 88m	100m (multi look)	24 to 89m
Observation Swath	40 to 70km	40 to 70km	250 to 350km	20 to 65km
Bit Length	5 bits	5 bits	5 bits	3 or 5bits
Data rate	240Mbps	240Mbps	120Mbps,240Mbps	240Mbps
NE sigma zero *2	< -23dB (Swath Width 70km) < -25dB (Swath Width 60km)		< -25dB	< -29dB
S/A *2,*3	> 16dB (Swath Width 70km) > 21dB (Swath Width 60km)		> 21dB	> 19dB
Radiometric accuracy	scene: 1dB / orbit: 1.5 dB			

Figure 43 –PALSAR Characteristics (JAXA 2014)

Note: PALSAR cannot observe the areas beyond 87.8 deg. north latitude and 75.9 deg. south latitude when the off-nadir angle is 41.5 deg.

- *1 Due to power consumption, the operation time will be limited.
- *2 Valid for off-nadir angle 34.3 deg. (Fine mode), 34.1 deg. (ScanSAR mode), 21.5 deg. (Polarimetric mode)
- *3 S/A level may deteriorate due to engineering changes in PALSAR (JAXA 2014).

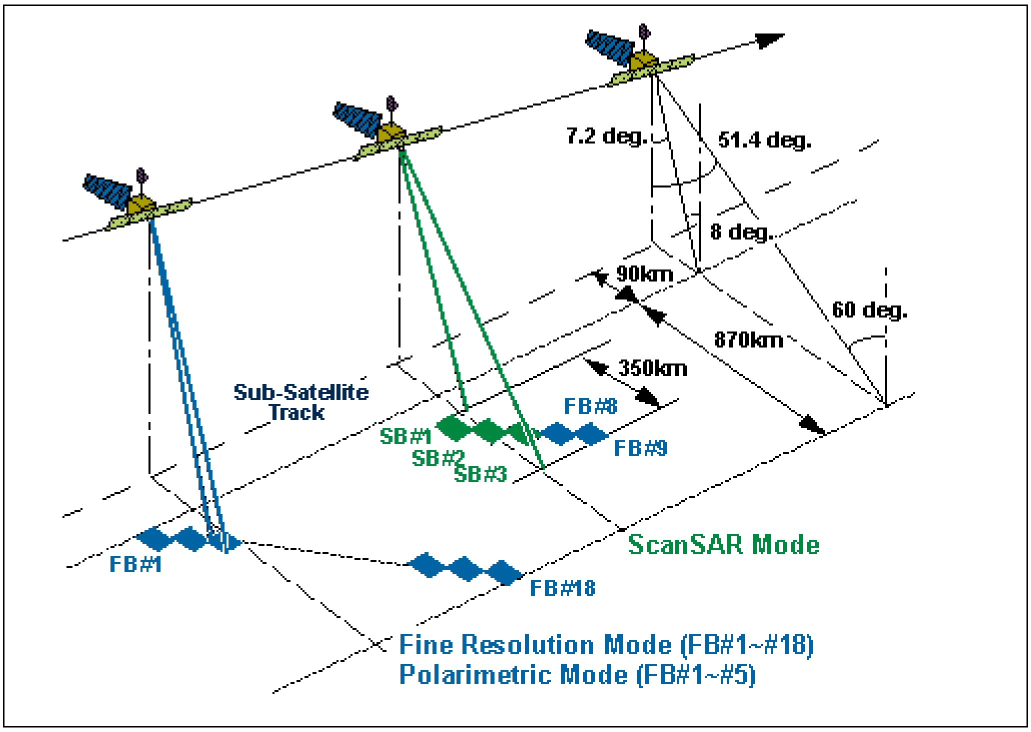

Figure 44 – PALSAR operating modes (JAXA 2014)

17.5.4 Calibration and Validation

Advanced Land Observing Satellite (ALOS, the nickname "Daichi") was successfully launched on January 24, 2006. After the initial mission check, the initial Calibration and Validation (Cal/Val) operation, which involve sensor characterizations, image quality measurements, and accuracy improvement of the standard products, were carried out from May 16 to November 23, 2006. After the initial Cal/Val operation, JAXA is continuously evaluating the standard products to improve those absolute accuracies (JAXA 2014).

Calibration and Validation of PRISM, AVNIR-2 and PALSAR on processing Level 1 data from Level 0 data are most important and necessary to improve the accuracy of high resolution DEM and biomass distribution data. Moreover, related basic studies required for Calibration and Validation of these sensors are essential for development coming generation sensors which have high performance (JAXA 2014).

17.5.5 General and Strategic Goals

<u>*General Goals*</u>

Some of the General Goals of ALOS Science Program are: the Land Use and Land Cover Research, the High-resolution Digital Elevation Model, the Orthophoto image (PRISM, AVNIR-2, PALSAR images) and land cover data, Topography and Geology, Elevation change due to soil erosion and sedimentation, Terrestrial (Vegetation) Ecosystem, Agriculture and Forestry Research, Forest distribution monitoring, Vegetation biomass distribution measurement, Application to forest management like: Monitoring the productivity of pastures and crop land, Monitoring vegetation change due to human activities such as biomass burning, Desertification Monitoring, Climatic System, Hydrological Processes, and Water Resources Realated Research like: Surface process in Vegetation monitoring, Estimating of soil moisture distribution and Run-off analysis, Water pollution analysis like Datasets of land use/land cover and their change, Snow and ice related analysis where are estimated states and changes of snow cover and snow-water equivalent, Measuring and analyzing variations of ice sheets and glaciers and sea ice monitoring, Oceanography and Coastal Zone Related Reasearch with: Oil datasets of coastal zones, High-resolution DEM of coastal zones, Datasets of sea surface wind and wave height in coastal zones, Datasets of sea ice, Ocean dynamics with fields like: Coastal topography-air-sea interaction. Wave-current interaction and various phenomena in the ocean, Disasters and Earthquakes: Diastrophism, Volcano monitoring, Slope failure, Analysis and simulation of flooding and inundation, Tidal wave analysis and Disaster monitoring technique, Basic Studies on Scattering and Interferometric Characteristics with Decomposition method for polarimetric SAR data, Polarimetric and interferometric data analysis (JAXA 2014).

Strategic Goals

Some of the Strategic Goals of ALOS Science Program are: Global High-resolution DEM and Orthophoto image (PRISM, AVNIR-2, and PALSAR), Global Biomass density dataset (PALSAR and AVNIR-2), Land surface deformation dataset (Earthquake-prone areas only), Algorithms that have to do with: Automated generation of high-resolution DEM and orthophoto image, Accuracy improvement of biomass measurement method, Calibration and Validation for each Sensor and Related Basic Studies, Calibration and validation for optical Sensors – Accuracy improvement of radiance and brightness calibration, Accuracy improvement of DEM, Atmospheric correction -, Calibration and validation for optical Sensors with Accuracy improvement of radiance and brightness calibration, Accuracy improvement of DEM, Atmospheric correction and Calibration and Validation for PLASAR system with Accurate estimation of normalized radar cross section, Accuracy improvement of interferometric SAR data and Accuracy improvement of polarimetric SAR data (JAXA 2014).

17.5.6 PALSAR Observation Strategy

The PALSAR acquisition strategy features routine observations at four pre-selected sensor modes* (Figure 46). The mode selection represents a compromise solution where scientific requirements, user requests, programmatic aspects and satellite operational constraints have been taken into consideration.

Sensor mode	Polarization	Off-nadir angle	Pass designation	Caverage	Time window	Observation frequency
Fine Beam Single pol.	HH	34.3°	Ascending	Global	Dec-Feb	1-2 obs/year
Fine Beam Dual pol.	HH+HV	34.3°	Ascending	Global	May-Sept	1-4 obs/year
Fine Beam Polarimatric	HH+HV+VH+VV	21.5°	Ascending	Regional	March-May	2 obs/2 year
Fine Beam Polarimatric	HH+HV+VH+VV	23.1°	Ascending	Regional	April-May	1 obs/2 year
ScanSAR 5-beam short burst	HH	20.1°-36.5°	Descending	(a) Global (b) Regional	Jan-Dec	(a) 1 obs/year (b) 8 obs/1 year
Fine Beam Dual pol.	HH+HV	49.0°	Ascending	the Arctic Circle	June-Oct	1-3 obs/year

Figure 45 – PALSAR Sensor default modes

To assure spatially and temporally homogeneous data collection over regional scales, acquisitions are planned in units of whole (46-day) repeat cycles, during which only one of the available default modes is selected. The PALSAR strategy is furthermore separated into one plan for ascending (evening) passes, and one for desceding (morning) ditto.

Ascending acquisitions (evening, ~22.30)

The PALSAR ascending mode plan comprises repetitive, global-scale observations with a constant off-nadir angle of 34.3° in both single polarisation (HH) and dual polarisation (HH+HV). To maintain mode-consistency in the multi-annual time series to be acquired, single-pol observations are scheduled during the northern hemisphere winter, and dual-pol observations around the summer months.

The minimum requirement for any land area on Earth is to perform at least one single-pol and one dual-pol acquisition annually, and in addition, two dual-pol acquisitions during consecutive 46-days cycles on a bi-annual basis to enable interferometric applications. Most areas are however to be acquired significantly more often than this, typically 3-5 times per year. In general, regions in the eastern hemisphere (Asia, Australia, eastern Europe and Africa) within the coverage of the Data Relay Satellite (DRTS) are acquired most frequently, while the western hemisphere (the Americas, western Europe and Africa) is restrained by the recording and down-link capacity of the on-board data recorder (HSSR).

To promote research relating to SAR polarimetry and polarimetric interferometry, polarimatric observation campaigns are planned once every two years, during which selected regions around the globe are acquired in full polarimetric mode during two consecutive cycles. As polarimetric operations at large off-nadir angles is not possible however, acquisitions will be performed at 21.5°.

Descending acquisitions (morning, ~10.30)

To minimize resource conflicts with PRISM and AVNIR-2, which only can be operated during day-time passes, the descending acquisition plan for PALSAR is principally limited to low data-rate (120 Mbps) ScanSAR observations at HH polarization.

The ScanSAR scenario comprises one global coverage on an annual basis, and in addition - given the LHH-band sensitivity to detect inundation phenomena - intensive monitoring over a number of selected regional-scale wetland environments of global significance. To adequately capture the hydrological changes that occur throughout the year, ScanSAR observations will typically be performed every 46-days during 8-9 consecutive satellite cycles (12-13 months).

* In addition to the 4 default modes, one more mode (Fine Beam HH at 21.5°) will be used for some limited, local-scale observations in descending mode (JAXA 2014).

17.6 ALOS Dataset

For this study were processed 27 ALOS-PALSAR PRI mode that cover a large area over Brazilian Amazon rainforest with full vegetation and residential zones too. These images cover a time period of almost 2 years while some of them covering the same areas giving the opportunity to apply timeseries studies. (table 5)

ALOS - PALSAR IMAGES	DATE
PSR_MMC_IP_0031278001	2/12/2010
PSR_MMC_IP_0031278002	2/12/2010
PSR_MMC_IP_0031279002	2/12/2010
PSR_MMC_IP_0031280002	2/12/2010
PSR_MMC_IP_0031281002	2/12/2010
PSR_MMC_IP_0031282001	2/12/2010
PSR_MMC_IP_0031282002	2/12/2010
PSR_MMC_TP_0067237001	17/5/2009
PSR_MMC_TP_0067237002	17/5/2009
PSR_MMC_TP_0067238001	17/5/2009
PSR_MMC_TP_0067238002	17/5/2009
PSR_MMC_TP_0067239001	17/5/2009
PSR_MMC_TP_0067240002	17/5/2009
PSR_MMC_TP_0067241001	17/5/2009
PSR_MMC_TP_0067245001	17/5/2009
PSR_MMC_TP_0067239002	17/5/2009
PSR_MMC_TP_0067240001	17/5/2009
PSR_MMC_TP_0067241002	17/5/2009
PSR_MMC_TP_0067242001	17/5/2009
PSR_MMC_TP_0067242002	17/5/2009
PSR_MMC_TP_0067243001	17/5/2009
PSR_MMC_TP_0067243002	17/5/2009
PSR_MMC_TP_0067244001	17/5/2009
PSR_MMC_TP_0067244002	17/5/2009

Table 5 – ALOS images (24 in number) used for multitemporal analysis

18. METHODOLOGY

18.1 ENVISAT Processing Methodology

As we mentioned above, we used 11 scenes of Envisat satellite, ASAR instrument that cover the region of Tocantins state of Amazon rainforest while contain pure vegetation and residential areas too. The data that are of 2004, 2005 and 2006 years have been divided in two groups. The one contains 3 images of 2004, 2005 and 2006 (there have been 2 images of 2006, of April and August, for comparing the combination of these 2 images of 2006 with the other 2 of 2004 and 2005 respectively). On the other hand, the other group contains 7 images of 2006 that cover a time period from January to August.

The first group of 3 images was used for applying a multitemporal analysis from which we can figure out important changes on vegetation and land uses that occurred in these 3 years (2004-2006), while the other one was used for a seasonal study of the area and like this we managed to study the alteration of the area vegetation.

More specifically, the first group of 3 images for the multitemporal analysis refers to the dates: 05/08/2004, 12/05/2005 and 27/04/2006 while the other one of 3 images refers to the dates: 05/08/2004, 12/05/2005 and 10/08/2006. As we analyzed above, we create these 2 groups of images because as far as the dates of 2006 are concerned, there were 2 different images: one of April (27/04/2006) and one of August (10/08/2006) while the images of 2004 and 2005 were of August and May respectively. There was no convenient solution for having three months that be in the same season so we decided to make these 2 combinations for having tried on all the potentials of the images.

As for the group that was used for the seasonal study, refers to dates: 12/01/2006, 16/02/2006, 23/09/2006, 27/04/2006, 01/06/2006, 06/07/2006 and 10/08/2006. It seems that these scenes cover almost the most part of the year and more specifically of the flowering season where we can study more accurately land cover.

Previously, was mentioned that these scenes are located in an area of the 3 states (Tocantins, Para and Goias) where Rio Paraná is running through make the whole region extremely fertile and rich in vegetation. The whole ENVISAT data processing was completed in Sentinel-1 Toolbox by ESA.

18.1.1 Remove Antenna Pattern

This operator removes antenna pattern and range spreading loss corrections applied to the original ASAR and ERS products. For ERS product, it also removes replica pulse power correction and applies the analogue to digital converter (ADC) power less correction. This operator cannot be applied to multilooked product (ESA).

Actually we didn’t applied this operator of Removing Antenna Pattern since in Envisat PRI the Antenna Pattern has been removed from the preprocessing procedure of the raw data.

Indeed, one major factor influencing accuracy of the measurement is the radiation pattern of the receiver antenna. The measured pattern will be the convolution product of the antenna radiation pattern and the phase function of the vegetation medium. The measured pattern therefore needs to undergo a deconvolution process before enable to provide reliable information (Cui H. 2010).

So, we applied this method to remove the distortion caused by the receiver antenna radiation pattern in the ASAR images.

For ground range detected products, the following corrections are removed:

- Antenna pattern gain
- Range spreading loss (SENTINEL-1 Toolbox ESA 2015)

18.1.2 Calibration

Calibration is the process of quantitatively defining the system response to known controlled signal inputs (SENTINEL-1 Toolbox ESA 2015).

Actually we didn't applied Calibration operator since the Envisat PRI data have been calibrated from the preprocessing procedure of the raw data.

The objective of SAR calibration is to provide imagery in which the pixel values can be directly related to the radar backscatter of the scene. To do this, the application output scaling applied by the processor must be undone and the desired scaling must be applied. Level-1 products provide four calibration Look Up Tables (LUTs) to produce ß0i, σ0i and γi or to return to the Digital Number (DN). The LUTs apply a range-dependent gain including the absolute calibration constant.

The radiometric calibration is applied by the following equation:

$$value(i) = \frac{|DN_i|^2}{A_i^{\,2}}$$

where, depending on the selected LUT,

$value(i)$ = one of $\beta^0{}_i$, $\sigma^0{}_i$ or γ_i or $originalDN_i$.

A_i = one of $betaNought\,(i)$, $sigmaNought\,(i)$, $gamma\,(i)$ or $dn(i)$

Bi-linear interpolation should be used for any pixels that fall between points in the LUT (ESA).

The objective of SAR calibration is to provide imagery in which the pixel values can be directly related to the radar backscatter of the scene. Though uncalibrated

SAR imagery is sufficient for qualitative use, calibrated SAR images are essential to quantitative use of SAR data.

Typical SAR data processing, which produces level 1 images, does not include radiometric corrections and significant radiometric bias remains. Therefore, it is necessary to apply the radiometric correction to SAR images so that the pixel values of the SAR images truly represent the radar backscatter of the reflecting surface. The radiometric correction is also necessary for the comparison of SAR images acquired with different sensors, or acquired from the same sensor but at different times, in different modes, or processed by different processors.

For ground range detected products, the following corrections are applied:

- Incidence angle
- Absolute calibration constant

In the event that the antenna pattern used to process an ASAR product is superseded, the operator removes the original antenna pattern, and apply a new, updated one. The old antenna pattern gain data is obtained from the external XCA file specified in the metadata of the source product. The new antenna pattern gain data and the calibration constant are obtained from the user XCA file.

For slant range complex products, the following corrections are applied:

- Incident angle
- Absolute calibration constant
- Range spreading loss
- Antenna pattern gain

The default output of calibration is sigma0 image. User can also select gamma0 and beta0 images outputting as virtual bands in the target product.

To IMS and APS products, ASAR ground range imageries (IMP like our data, APP, IMM, APM, WSM) have all been applied antenna gain pattern compensation (based on ellipsoid approximations) and range spreading loss correction during the formation of the images. Therefore the antenna pattern correction applied to the image must be removed when updated XCA file is available for the product (SENTINEL-1 Toolbox ESA 2015).

The sigma nought image can be derived from ESA's SAR ASAR level 1 IMP, APP, IMM, APM, WSM products.

18.1.3 Terrain Correction

In Sentinel-1 Toolbox we applied Doppler Terrain Correction to the scenes that had been first calibrated. The software gives the opportunity to apply radiometric normalization at the same time with the Terrain Correction so we selected this parameter too.

The relative methods proceed under the assumption that the relationship between the at-sensor radiances recorded at two different times from regions of constant reflectance is spatially homogeneous and can be approximated by linear functions. The most difficult and time consuming aspect of all of these methods is the determination of suitable time-invariant features upon which to base the normalization (Tarantino E. 2010).

The radiometric normalization makes this technique particularly advantageous. In such cases is fundamental to correct radiometrically images, in order that information contained in a single DN (Digital Number) is lightly influenced by noise. Absolute radiometric correction of multi-temporal satellite imagery requires atmospheric corrections associated with the atmospheric properties at the time of the image acquisition (Tarantino E. 2010)

We didn’t applied Terrain correction since it is not necessary in these kind of images.

The Terrain Correction Operator will produce an orthorectified product in the WGS 84 geographic coordinates. The Range Doppler orthorectification method is implemented for geocoding SAR images from a single 2D raster radar geometry. It uses available orbit state vector information in the metadata or external precise orbit, the radar timing annotations, the slant to ground range conversion parameters together with the reference DEM data to derive the precise geolocation information. Optionally radiometric normalization can be applied to the orthorectified image to produce σ^0, γ^0 or β^0 output (SENTINEL-1 Toolbox ESA 2015). In this case, we did produce these parameters.

18.1.4 Corregistration

Then, we applied Corregistration to all ASAR images since it is obligatory for SAR images processing. Thus coregistration, the alignments of SAR images from two antennas, is an essential step for the accurate determination of phase difference and for noise reduction. The entire purpose of the coregistration is to align the samples for phase differencing (Zhengxiao L. 2008).

These ASAR images were processed for change detection application, for detecting vegetation and land use changes. They all cover almost the same area. Change detection requires pixel-to-pixel match between (Zhengxiao L. 2008). the scenes. So, it was essential to be applied Corregistration for detecting the common features in SAR image groups and separating the areas with differences.

For the Corregistration of the images was used the Automatic Corregistration method while the RMS was initially set to be 0.45. In this step we used the scenes where had been applied terrain correction while the Resampling type was set to: Nearest Neighbour.

Image co-registration is fundamental for Interferometry SAR (InSAR) imaging and its applications, such as DEM map generation and analysis. To obtain a high quality InSAR image, the individual complex images need to be co-registered to sub-pixel accuracy.

The Toolbox co-register accurately one or more slave images with respect to a master image. The co-registration function is fully automatic, in the sense that it does not require the user to manually select ground control points (GCPs) for the master and slave images.

Images may be fully or only partly overlapping and may be from acquisitions taken at different times using multiple sensors or from multiple passages of the same satellite.

The achievable co-registration accuracy for images in the same acquisition geometry and over flat areas will be better than 0.2 pixels for two real images and better than 0.05 pixels for two complex images.

The image co-registration is accomplished in three major processing steps with three operations: Create Stack operator, GCP Selection operator and Warp operator.

The GCP Selection operator then creates an alignment between master and slave images by matching the user selected master GCPs to their corresponding slave GCPs. There are two stages for the operation: coarse registration and fine registration. For real images co-registration, the coarse registration is applied. The registration is achieved by maximizing the cross-correlation between master and slave images on a series of imagettes defined across the images. For complex image co-registration, the additional fine registration is applied. The registration is achieved by maximizing the coherence between master and slave images at a series of imagettes defined across the images.

With the master-slave GCP pairs selected, a pair function is created by the Warp operator, which maps pixels in the slave image into pixels in the master image (SENTINEL-1 Toolbox ESA 2015).

18.1.5 Filtering

The scattering from distributed scatterers leads to coherent interferences of waves scattered from many randomly distributed elementary scatterers inside the resolution cell. This provokes granular noise which actually is the speckle phenomenon. This phenomenon provokes the distortion of the interpretation (ESA).

The presence of speckle noise as grainy salt-and-pepper patterns in a SAR image often obscures the underlying image content, reduces the interpretability of the image, and complicates digital image processing (Qiu F. 2004).

There many filters that we can apply on SAR images via the Sentinel-1 Toolbox software. Some of them are: Frost, Gamma Map, Lee and Refined Lee. Actually, applying Image filtering, pixel values of an original image are modified using the gray values of the neighboring pixels.

Sigma Filter (Lee) and Frost Filter (Frost) that were used in this paper are linear speckle filters. SPECKLE is a scattering phenomenon and not a noise. However, from the image SAR processing point of vıew, the speckle can be modeled as multiplicative noise for extended target » (Pottier E. 2004)

Moreover, Lee et al. 2009 mention that Lee filter window 7x7 size and Frost filter (with a damping factor of 2) window size 5x5 are the best choises for VV and VH polarization. Window size is for smoothing. The larger the window size, the larger the smoothing is. So, we decided to use those 2 filters after having applying, of course few of the rest of them that Sentinel-1 Toolbox provides with in order to figure out which are the best for our situation.

Thus, in this thesis, as we mentioned above, we decided to apply Lee and Frost filters. Furthermore, at this point it would be good to clarify that except for the fact that has to do with the filter. Each filter can be applied in special combinations depending on the kernel that is used. Another setting is about the window size. This parameter is about smoothing. The larger the window size, the largest the smoothing.

The adaptability of the Lee or Frost filter to the local speckle and scene statistics are known (Qiu F. 2004).

Speckle noise corrupts images that are obtained by coherent radiation, like SAR instruments. The presence of this type of noise decreases the usefulness of these images for both human and automatic interpretation.

A simple moving average (eg, 3x3, 5x5 window) over the image tends to reduce the speckle, due to the fact that there is a tendency for a moderately low correlation between adjacent speckle samples, if the point spread function of the sensor is not too wide. However, this low-pass filter tends to indiscriminately blur the image.

Lee developed a widely used local statistics filter for speckle noise reduction. A pointwise linear filter minimizing the mean square error has the form:

$$x' = x_m + b(z - x_m)$$

where

$$b = var(x)/var(z)$$

And x_m and var(x) (a priori mean and variance of the original signal) can be estimated through measurements of the sample mean and sample variance of the noisy image and knowledge of the type of detection and number of looks by the expressions (Nelson D. 1997):

$$x_m = z_m / n_m = z_m$$

and

$$\mathrm{var}(x) = \frac{\mathrm{var}(z) - z_m^2 \sigma_n^2}{\sigma_n^2 + 1}$$

The evaluation of a filter performance should consider several factors: retention of mean value over homogeneous areas, (unbiasedness), speckle reduction capability, edge sharpness and thin features preservation, texture preservation, computational efficiency and implementation complexity (Mascarenhas, N. D. A.1997).

Speckle noise is a common phenomenon in all coherent imaging systems like laser, acoustic and SAR imagery. The source of this noise is attributed to random interference between the coherent returns issued from the numerous scatterers present on a surface, on the scale of a wavelength of the incident radar wave (i.e. a resolution cell). Speckle noise is often an undesirable effect, especially for ATR systems. Thus, speckle filtering turns out to be a critical pre-processing step for detection/classification optimization (Gagnon L.).

Basically, SAR speckle reduction techniques fall into two categories: non-coherent (or multi-look integration) and adaptive image restoration techniques (post-image formation methods). Multi-look techniques5 consist of (1) dividing the bandwidth of the azimuth (along track) spectrum of the radar image into L segments (called looks and corresponding to L echo spectra of the same scene point generated by L incident radar pulses), (2) forming L independent images from these spectra and (3) incoherently averaging them. This reduces the azimuth spectrum bandwidth, and thus speckle noise, but at the expense of increasing the computational load and degrading the image resolution if L is too large. However, many SAR systems integrate few looks during the image formation in order to minimally improve image quality. If necessary, residual speckle has to be processed using post-image formation filters. Among the more widely used filters are the Median, Lee, Kuan, Frost and Gamma filters. Others like the Kalman, Geometric, Oddy and AFS filters are less common (maybe because of the algorithmic complexity) but are nevertheless considered as competitive candidates to the “standard" filters. All these filters usually perform efficiently on most SAR images but with some limitations regarding resolution degradation and smoothing of uniform areas. Wavelet-based filterings have been proposed to overcome these difficulties. They are essentially based on a WCS approach and seem to demonstrate a higher quality in image enhancement (i.e. good signal averaging over homogeneous regions with minimal resolution degradation of image details). We have recently proposed such a filter, based on the use of SD wavelets. The performance results were encouraging but comparative tests were performed only with a small subset of standard filters (Median and Geometric). A more extensive test bank was required in order to better validate our tool; this is the purpose of the present work (Gagnon L.).

SAR images have inherent salt and pepper like texturing called speckles which degrade the quality of the image and make interpretation of features more difficult. Speckles are caused by random constructive and destructive interference of the de-phased but coherent return waves scattered by the elementary scatters within each resolution cell. Speckle noise reduction can be applied either by spatial filtering or multilook processing.

The operator supports the following speckle filters for handling speckle noise of different distributions (Gaussian, multiplicative or Gamma):

- Mean
- Median
- Frost
- Lee
- Refined Lee
- Gamma-MAP

The parameters that should be selected are: the source band (if it is not set then by default all bands will be selected), the speckle filter, the x and y size of the kernel (width and height respectively). For Frost filter, an extra parameter is required: the frost damping factor. Furthermore, for Refined Lee filter an extra parameter is obligatory to be set: the Edge Threshold. It is a threshold for detecting edges. An area of 7x7 pixels with local variance lower than this threshold is considered flat and normal Local Statistics Filter is used for the filtering. If the local variance is greater than the threshold, then the area is considered as edge area and Refined Lee filter will be used for the filtering (SENTINEL-1 Toolbox ESA 2015).

18.1.5.1 Lee Filter

The Lee sigma filter was developed in 1983 based on the simple concept of two-sigma probability, and it was reasonably effective in speckle filtering. However, deficiencies were discovered in producing biased estimation and in blurring and depressing strong reflected targets. The advancement of synthetic aperture radar (SAR) technology with high-resolution data of large dimensions demands better and efficient speckle filtering algorithms (Lee J.-S. 2008).

We can use Lee filters to smooth noisy (speckled) data that have an intensity related to the image scene and that also have an additive and/or multiplicative component. Lee filtering is a standard deviation based (sigma) filter that filters data based on statistics calculated within individual filter windows. Unlike a typical low-pass smoothing filter, the Lee filter and other similar sigma filters preserve image sharpness and detail while suppressing noise. The pixel being filtered is replaced by a value calculated using the surrounding pixels (Lee J.-S. 2008).

Lee filter was derived from the minimum square error (MMSE) criteria by introducing the local statistics method in it. It was believed that it can reduce speckle noise while preserving the edges in the image (Huang Y. 1996)

Adaptive filters, such as the Lee filter, are based on the assumption that the mean and variance of the pixel of interest are equal to the local mean and variance of all pixels within the user-selected moving window. The Lee filter removes the noise by minimizing either the mean square error or the weighted least square estimation. The Lee filter has the ability to preserve prominent edges, linear features, point target, and texture information (Qiu F. 2004).

The Lee filter (more precisely Lee MMSE filter) is a particular case of the Kuan filter when the term σ^2_x/L is removed in Eq.:

$$\hat{x} = \bar{y} + \frac{\sigma_x^2 (y - \bar{y})}{\sigma_x^2 + (\bar{y}^2 + \sigma_x^2)/L}$$

This term does not appear in Lee's original derivation due to a linear approximation made there for the multiplicative noise model (a first-order Taylor series expansion of *y* about *x* and *n*) (Gagnon L.).

18.1.5.2 Frost Filter

We can use Frost filters to reduce speckle while preserving edges in radar images. The Frost filter is an exponentially damped circularly symmetric filter that uses local statistics. The pixel being filtered is replaced with a value calculated based on the distance from the filter center, the damping factor, and the local variance (Shi Z. 1994).

In this filter, it required that we enter the value in the Damping Factor field. The damping factor determines the amount of exponential damping and the default value of 1 is sufficient for most radar images. Larger damping values preserve edges better but smooth less, and smaller values smooth more. A damping value of 0 results in the same output as a low pass filter (Shi Z. 1994).

In this paper, we entered a damping factor of 2 since we checked and compared the results with the ones of factor 1 and we decided that were a little bit better.

It was derived from the principle of MMSE. The filter kernel can vary with the local statistical value of the images so as to reduce the noise while at the same keeping the edges (Huang Y. 1996).

The Frost filter replaces the pixels of interest with a weighted sum of the values within the moving window. The weighting factors decrease with distance from the pixel of interest and increase for the central pixels as variance within the window increases. This filter assumes multiplicative noise and stationary noise statistics (Qiu F. 2004).

A linear minimum mean square error convolutional filter for multiplicative noise reduction was proposed from Frost et al. The observed process is assumed to be further convoluted by a point spread function h(t), although this blurring is ignoring in the derivation of the filter, which has the form:

$$x'(t) = z(t) * m(t) \quad \text{(a)}$$

Where m(t) is an isotropic impulse response of the spatial filter given by an exponential expression:

$$m(t) = K_1 \alpha \exp(-\alpha|t|) \quad \text{(b)}$$

K_1 is a normalizing constant that guarantees the preservation of the mean value and *a* is given by:

$$\alpha^2 = (2a/\sigma_n^2)[\mathrm{var}(x)/(\mathrm{var}(x) + x_m^2)] + a$$

Where xm and var(x) are evaluated by eqs.(a) and (b), respectively, over a 5x5 window and exp(-a) is the correlation coefficient between adjacent pixels of the original image x(t). By assuming an autoregressive model for the original image x(t). By assuming an autoregressive model for the original non-noisy backscatter image, Quelle and Boucher proposed an implementation of Frost’s filter including an estimation of that correlation coefficient (Mascarenhas, N. D. A. 1997).

Although Frost’s filter was shown to be not optimal, it has been widely used for speckle noise reduction (Mascarenhas, N. D. A. 1997).

18.2 ALOS Processing Methodology

Alos data require an extending processing since it' is about a very complicated data system. PolSARpro is a suitable software for full processing of such data and extracting important and useful results.

18.2.1 Import of Data

In the step of importing the data we must determine which is the exact directory of the image that we are going to process.

18.2.2 Data Extraction

In this step it is realized the ALOS data extraction and it is produced a Pauli decomposition image.

The Pauli decomposition is suited for analysis of high-resolution SAR data because it operates on the individual pixels on a coherent basis. It further characterizes scatterers in terms of the following physical concepts:

- s alpha matrix: sphere, plate, or trihedral (single- or odd-bounce scattering). Alpha^2 is the power scattered by these types of targets.
- s beta matrix: dihedral oriented at 0 degrees. Beta^2 represents the power scattered by this type of target.
- s gamma matrix: diplane oriented at 45 degrees. Gamma^2 is the power scattered by this type of target.

The Pauli components can be used to classify land cover. Each intensity can be color coded (alpha to R; beta to G; and gamma to B). An RGB display of the intensity of the first three Pauli components is useful for manual interpretation (PCI Geomatics, 2015).

In this step, as we previously mentioned, it is produced an image based in the Pauli decomposition.

18.2.3 Geocoding

Geocoding of SAR data is a very important step in SAR data processing since it allows to resample SAR data in ground geometry.

When geocoding and rectification is performed, the output image will commonly have different pixel size, orientation, and coordinates from those in the input image. To determine the DN values for pixels in output image, the resampling process is required. Resampling is the process of determining new values for output pixels after geometric transformation of input image. It is based on the original image. Three commonly used resampling techniques: nearest neighbor, bilinear, and cubic convolution (Jensen, J.R. 1996.).

Chapter 6 in Jensen, J.R. 1996. Introductory Digital Image Processing: A Remote Sensing Perspective. Second Edition, Upper Saddle River, NJ, Prentice Hall. 318pp.

PolSARpro offers geocoding tools via the 3 methods too. The user has the opportunity to select which method is more appropriate for his data.

<u>Resampling methods</u>

- **Nearest neighbor resampling**

The nearest neighbor assignment will identify the location of the closest input pixel, then assign the value of the nearest input pixel to the output pixel. Nearest neighbor sampling has the least apparent impact, copying actual data values to the output image. However, this technique may induce high frequency artifacts, causing edges to appear in the direction of sampling. Nearest neighbor resampling should be used for multi-band images. During processing, the relationship between bands is preserved, allowing more accurate crossband operations.

- **Bilinear resampling**

Bilinear interpolation identifies the four nearest input pixels to the location of an output pixel. The new value for the output pixel is a weighted average determined by the value of the four nearest input pixels and their relative position or weighted distance from the location of the center of the output pixel in the input image. The bilinear interpolation reduces the high frequency component of the image, blurring sharp edges. It is preferred for continuous surfaces and smoothly varying images. Elevation, temperature, air pressure, gravitational or magnetic field can be represented as continuous smooth images, and are most appropriately resampled using bilinear interpolation. Bilinear resampling is not suitable for crossband processing. During 2- dimensional interpolation the relationship between the two bands can be altered undesirably.

- **Cubic convolution resampling**

Cubic convolution uses the 16 nearest input pixels to determine the output pixel value. A smooth surface specified by a 2-dimensional third order polynomial equation is fitted through the input pixels to find the value at the output pixel center. Cubic convolution tends to smooth the data more than bilinear resampling method. Cubic convolution may considerably distort the original data, and is not recommended for rigorous calculations. But it can be used to enhance data for visual display.

The nearest neighbor assignment should be used for nominal (categorical) or ordinal data. Bilinear interpolation or cubic convolution should not be used on categorical data. All three techniques can be applied to continuous data, with the nearest neighbor producing the more blocky output and the cubic convolution the smoothest result. On this Thesis we applied bilinear resample technique according to ALOS data processing suggestions (using PolSARpro software) of Pottier Er. in the Summer School during July of 2013 in the Harokopio University of Athens. One of the default parameters is the Datum of WGS84. Geocoding was applied to all of 24 Alos images we had (Jensen, J.R. 1996).

18.2.4 Terrain Correction

Terrain correction is the process of correcting geometric distortions that lead to geolocation errors. The distortions are induced by side-looking (rather than straight-down looking or nadir) imaging, and compounded by rugged terrain. Terrain correction moves image pixels into the proper spatial relationship with each other (Alaska Satellite Facility, 2016).

Thus, the objective of the SAR geocoding is to reconstruct the imaging geometry to find the corresponding position on the Earth for each image pixel. Since the satellite state vector is known from orbit information, the position of each SAR pixel is estimated on a given earth model by solving the rangeDoppler equations. Due to geometrical distortions caused by the side looking geometry, a one-to-one relation does not exist between radar and map geometry. Therefore, a DEM is used to perform an accurate geocoding and then geometric terrain correction of terrain induced distortions (Akbari B 2014).

It is a very essential processing step for scenes of mountainous areas especially. In our case, we tried to applied terrain correction using an SRTM of GeoTIFF format at 90-meter resolution that covers the whole images area. We achieved to apply terrain correction to 9 of them but the rest of them showed a problem so the terrain correction was impossible to be done.

18.2.5 Create KML file

In order to locate our data in the globe we created kml files for each Alos image that we processed.

18.2.6 Matrix Elements

This step creates binary files corresponding to the modulus and argument of the (3x3) complex Coherency matrix (**[T3]**) raw binary data (López-Martínez C. 2005)

At the same time we can check an option for creating simultaneously the corresponding bitmap image files.

Several channels may be processed at a time. The selection of the BMP options enables the creation of output bmp files, as we mentioned before.
Users may choose between three types of output binary data:
• Modulus: Linear representation of the considered **[T3]** element amplitude. Ouput file name: Tij_mod.bin (.bmp)
• Modulus: Element amplitude in dB=10log10(Modulus). Ouput file name: Tij_dB.bin (.bmp)

• Phase: Argument of the considered complex **[T3]** element (Only available for off-diagonal elements). Ouput file name: Tij_pha.bin (.bmp)
• Span: Correspond to the sum of the diagonal elements of **[T3]**, may also be processed (linear and dB) using this program (PolSARpro Documentation).

We selected options: T11(of 10log Modulus), T12 (phase). T22 (of 10log Modulus), T33 (of 10log Modulus) and Span (DeciBel) according to the suggestions of Pottier Er.

18.2.7 Decomposition Parameters

This step creates binary files corresponding to the different polarimetric descriptors obtained from the H/A/Alpha decomposition of the (3x3) complex Coherency matrix **[T3]** raw binary data.

The H/A/Alpha polarimetric decomposition is based on an eigenvector decomposition of the (3*3) complex Coherency **[T3]** matrix.

The (3x3) complex Coherency **[T3]** matrix being hermitian, semi-definite positive, its eigenvectors are orthogonal and its eigenvalues are real positive. The eigenvector decomposition of a distributed target coherency matrix is considered as a simple statistical model consisting in the expansion of the (3x3) complex Coherency matrix into a weighted sum of three coherency matrices.

Pseudo-probabilities of the (3x3) complex Coherency **[T3]** matrix expansion elements are defined, from the set of sorted eigenvalues.

The distribution of the probabilities can be fully described by two parameters :

- The entropy (H) indicates the degree of statistical disorder of the

scattering phenomenon. It derives, in the Von Neumann sense, from the set of probabilities as:

- For high entropy values, i.e. superior to 0.7, a complementary parameter is

necessary to fully characterize the set of probabilities. The anisotropy (A) is defined as the relative importance of the secondary scattering mechanisms.

Each unitary eigenvector of the (3x3) complex Coherency **[T3]** matrix may be parameterized using 4 real angular variables (a,b,c and d).

The condition of mutual orthogonality between the eigenvectors involve that the 3 polarimetric parameters sets resulting from the expansion are not independent. For this reason, each polarimetric parameter is associated to a 3 symbol Bernoulli statistical process. In this way, the estimate of the mean polarimetric parameter set is given by:

A physical interpretation has been given to these 4 polarimetric descriptors (López-Martínez C. 2005).

Data to be decomposed may be processed through an additional filtering procedure consisting of a boxcar filter. Users have then to set the size of the (N*N) sliding window used to compute the local estimate of the average matrix (López-Martínez C. 2005).

We set this size to be: 8*1 like in all previous cases.

18.2.8 H/A/Alpha Classification

This program creates binary and bitmap image files resulting from the classification of polarimetric data in the H-Alpha, H-A and Alpha-A planes obtained from the H/A/Alpha decomposition of polarimetric raw binary data.

This program offers also the possibility to create color coded bitmap image files. The color coding is realised by assigning input files (results of the H/A/Alpha decomposition) either to the Red Green Blue channels or to the Hue Saturation Lightness channels of a 24 bit colormap.

Polarimetric descriptors of scattering mechanisms, such as H, A and Alpha are known to be tightly related to observed media physical properties. Such relevant parameters may be used to classify in an unsupervised way polarimetric data, using linear decision boundaries in the (H-Alpha), (H-A) or (Alpha-A) planes. The different decision boundaries are set in an arbitrary way so as to isolate different canonical scattering properties usually encountered in polarimetric data sets.

H-Alpha Classification

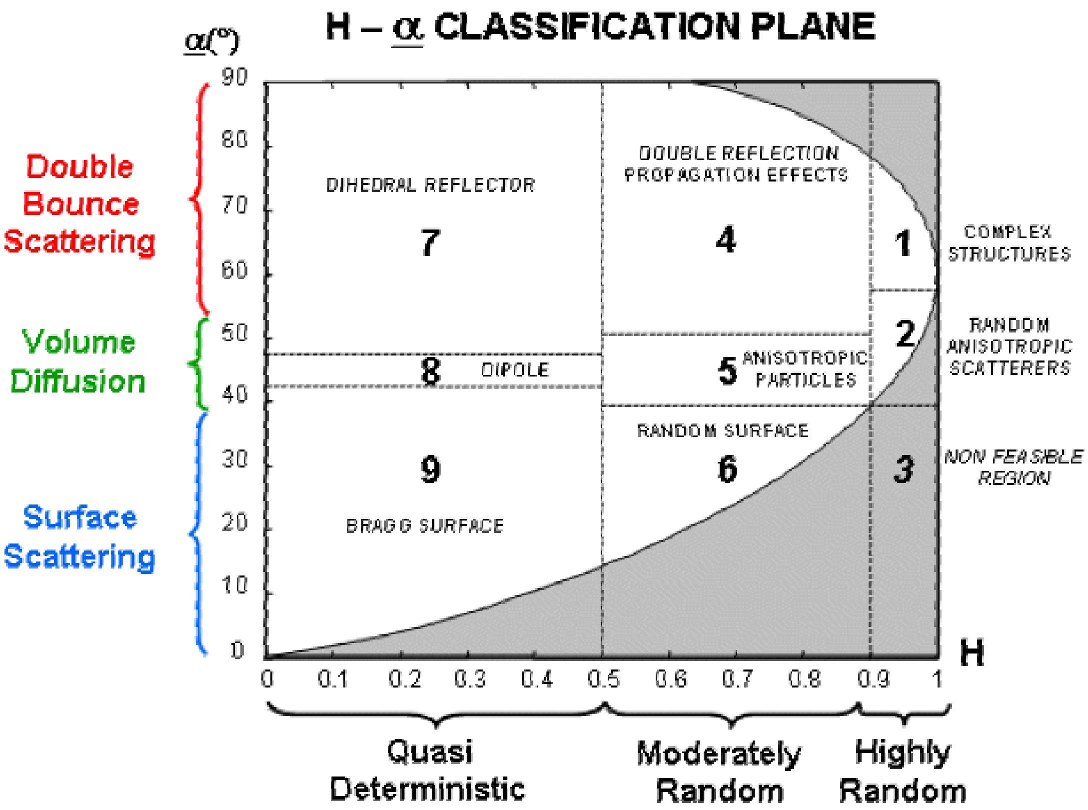

The H/Alpha classification aims to discriminate different types of canonical scattering mechanisms, using Alpha, with different degrees of randomness from the entropy H. Pixels are assigned to one of the 8 classes delimited in the H-Alpha plane using linear boundaries. Gray areas correspond to unreachable regions.

H-A Classification

The joint use of H and A allows to fully describing the pseudo-probability spectrum of a distributed coherency matrix. H may be used to discriminate random scattering from deterministic polarimetric patterns, while the anisotropy is useful to estimate the pseudo probability distribution in the case of intermediate entropy values.

A-Alpha Classification

The last combination of the H-A-Alpha parameters leads to the definition of a classification scheme relying on a segmentation of the Alpha-A plane. The coordinates of the linear decision boundaries remain similar to those stipulated for the H-Alpha and H-A classification procedures.

H-A-Alpha Classification

Each classification procedures creates three output files
• A classified data binary file containing the class index of
each pixel of the input image.
• The corresponding bitmap image file.
• A bitmap image file indicating the pixels occurrence
(density) in the selected classification plane.
• A bitmap image file indicating the location of classified
data in the selected classification plane.
The different classification procedures may be simultaneously
selected. The different output files are
• H_alpha_class.bin & H_alpha_class.bmp
• H_alpha_occurence_plane.bmp
H_alpha_segmented_plane.bmp
• H_A_class.bin & H_A_class.bmp
• H_A_occurence_plane.bmp & H_A_segmented_plane.bmp
• A_alpha_class.bin & A_alpha_class.bmp
• A_alpha_occurence_plane.bmp
A_alpha_segmented_plane.bmp

Color Map

The color coding of the bitmap output files is realized by the way of a 9 element colormap initialised with arbitrary values. Users have the possibility to modify the elements of the colormap in an interactive way (López-Martínez C. 2005).

18.2.9 Eigenvalue Set Parameters

This program creates binary files corresponding to the different polarimetric descriptors obtained from the H/A/Alpha decomposition of the (3x3) complex Coherency matrix **[T3]** raw binary data.

An option may be set to simultaneously create the corresponding bitmap image files.

The H/A/Alpha polarimetric decomposition is based on an eigenvector decomposition of the (3*3) complex Coherency **[T3]** matrix. Pseudo-probabilities of the (3x3) complex Coherency **[T3]** matrix expansion elements
are defined, from the set of sorted eigenvalues. The different Polarimetric Descriptors proposed from the Eigenvalue Sets are:

The anisotropy (**A**): $$A = \frac{p_2 - p_3}{p_2 - p_3} \quad with \quad 0 < A < 1$$

The anisotropy12 (**A12**): $$A12 = \frac{p_1 - p_2}{p_1 - p_2} \quad with \quad 0 < A12 < 1$$

The Single bounce Eigenvalue Relative Difference (S.E.R.D) and the Double bounce Eigenvalue Relative Difference (D.E.R.D).

The polarisation asymmetry (**PA**): $$PA = \frac{p_1 - p_3}{p_2 - p_3} \quad with \quad 0 < PA < 1$$

The polarisation fraction (**PF**): $$PF = 1 - 3p_3 \quad with \quad 0 < PF < 1$$

The Radar vegetation Index (**RVI**): $$RVI = \frac{4p_3}{p_1 + p_2 + p_3} \quad with \quad 0 < RVI < 1$$

The Pedestal Height (**PH**): $$PH = \frac{min(p_1, p_2, p_3)}{max(p_1, p_2, p_3)} \quad with \quad 0 < PH < 1$$

The Kozlov Anisotropy (**KA**): $$KA = \frac{|s_1|^2 - |s_2|^2}{|s_1|^2 + |s_2|^2} \quad with \quad 0 < KA < 1$$

Where ***s1*** and ***s2*** are the pseudo eigenvalues of the 2x2 Complex Sinclair Matrix

The Kozlov Complex Anisotropy (**KCA**):

$$KCA = \frac{s_1 - s_2}{s_1 + s_2} \quad with \quad 0 < |KCA| < 1$$

Where ***s1*** and ***s2*** are the pseudo eigenvalues of the 2x2 Complex Sinclair Matrix

The Lueneburg Anisotropy (**LA**):

$$LA = \sqrt{\frac{3}{2}} \sqrt{\frac{p_2^2 + p_3^2}{p_1^2 + p_2^2 + p_3^2}} \quad with \quad 0 < LA < 1$$

The Shannon Entropy (**SE**): $$SE = SE_I + SE_P$$

With: $$SE_I = 3\,log\left(\frac{\pi e Tr[T3]}{3}\right) \qquad SE_P = log\left(27\,\frac{det[T3]}{Tr[T3]^3}\right)$$

In this step we calculated 6 parameters according to the indications of Er. Pottier based on the summer school training of 2013 in Harokopio University. The parameters we calculated are: Pseudo Probabilities (pi,p2,p3), Polarisation Asymmetry (p1-p3,1-3p3), Polarisation Fraction (1-3p3), Lueneburg Anisotropy and Shannon Entropy (H=Hi+Hp). Furthermore, we decided to calculate Radar Vegetation Index (R.V.I.) too as we process images that cover vegetated areas and we thought that it was an interesting idea to apply this index since we might get important information.

18.2.10 Polarimetric Decompositions

PolSARpro offers the opportunity to its users to apply one of the well-known Polarimetric Target Decompostion Theorems on polarimetric data set (López-Martínez C. 2005).

The objective of the coherent decompositions is to express the measured scattering matrix by the radar, as a the combination of the scattering responses of simpler objects (López-Martínez C. 2005).

There are multiple Polarimetric Decomposition models like: Cloude, An & Yang, Freeman, Neuman, Van Zyl, Yamaguchi, L,Zhang, Cameron etc. In this paper we applied 3 of them according to the indications of Er. Pottier according to summer school training of 2013 in Harokopio University. We applied the models of Freeman, Yamaguchi and Van Zyl.

In Yamaguchi and Van Zyl models we selected option of creating TgtG files in order to create a 24-bit colour BMP image (Windows Bitmap format) which contains contrasted red, green and blue channels assigned to the 3 Huynen Target Generators (TgtG) after decomposition (López-Martínez C. 2005).

The target decomposition was first introduced by Chandrasekhar (1960) and later applied to polarized microwave by Huynen (1970). Coherent decomposition theorems use [S] matrices. It considers a matrix [S] as linear combination of several other scatterers. A method for coherent target decomposition was presented by Krogager, 1988. His approach was based on the obsarvation that any complex, symmetric scattering matrix can be decomposed into three components, as if the scattering were due to a sphere, a diplane and a right or left rotating helix. A three-component scattering model for polarimetric SAR data is proposed by Freeman and Durden (1998). Cloude et.al. (1966(a), 1995(b)) have suggested the H-A-alpha target decomposition theorem. Van Zyl (1989) describes the use of an imaging radar polarimetric data for unsupervised classification of scattering behavior by comparing the polarization properties of each pixel in an image to that of simple classes of scattering such as even number of reflections, odd number of reflections, and diffuse scattering (Shah K. 2011).

Coherent target decomposition methods can only be applied to coherent scattering. Generally, the scattered wave is partially polarized and the user might be interested in the extraction of geophysical parameters from an area that exhibits significant natural variability in the scattering properties (Van Zyl, 1992). For different target decomposition methods Alberga et al. (2004) has applied Minimum Distance, Maximum Likelihood and Parallelepiped classifier. A four-component scattering model is proposed by Yamaguichi et al., 2005 to decompose polarimetric synthetic aperture radar images. Circular polarization power is added as the fourth component to the three component scattering model which describes surface, double bounce, and volume scattering. This circular polarization term is added to take into account of the co-pol and the cross-pol correlations which generally appear in complex urban area scatttering and disappear for natural distributed scatterer. Wang, et.al (2009) proposed a method of unsupervised classification of polarimetric SAR data based on image clustering and H/A/α decomposition. Fully polarimetric L band data collected by ALOS PALSAR system was used in this paper. The relation between physical structure and polarimetric signal properties is studied explicitly using polarimetric decomposition. The H/A/α decomposition theorem is the basis for the design of the proposed processing scheme for polarimetric SAR images. An improved land-cover classification based on this indicates the scattering properties of target classes very well and hence can be used to produce a much more improved classification result. The volume scattering Fv from the Freeman decomposition contributes a significant part to the improvement of classification. A comparison of polarimetric target decomposition methods is proposed by Zhang et.al. (2008). Results show that among many target decomposition algorithms, the coherent and incoherent formulations are quite comparable in distinguishing natural targets and man-made buildings. Pauli decomposition, Cameron decomposition and Freeman decomposition are suitable for the detection of natural targets. On the other hand, SDH decomposition, OEC decomposition, and Four-component model, in particular, are very useful for man-made target extraction. The Touzi decomposition is investigated for wetland characterization. A target scattering decomposition was investigated by Touzi et. al. (2009), for wetland classification. The Touzi decomposition, which permits a roll-invariant target scattering decomposition, leads to the characterization of wetland classes in terms of unique target parameters. Ballester-Berman et. al. (2010) proposed a procedure for exporting the Freeman–Durden PolSAR TD concept to PolInSAR data. The formulation of the Freeman–Durden decomposition has been adapted to PolInSAR in order to jointly retrieve not only the magnitude but also the interferometric phases (related to the vertical locations) of the direct (odd-bounce), double-bounce, and volume scattering mechanisms (Turkar V. 2011).

18.2.10.1 Freeman

The Freeman decomposition models the covariance matrix as the contribution of three scattering mechanisms:

- Volume scattering where a canopy scatterer is modeled as a set of randomly oriented dipoles.
- Double-bounce scattering modeled by a dihedral corner reflector.
- Surface or single-bounce scattering modeled by a first-order Bragg surface scatterer (López-Martínez C. 2005).

The classical model-based decomposition was Freeman-Durden decomposition (FDD) developed by Freeman and Durden, which decomposed the coherency matrix of PolSAR data into three components: surface scattering, double-bounce scattering, and volume scattering with the reflection symmetry condition. The reflection symmetry condition implies that the correlation between copolarized term and cross polarized term is zero. Freeman-Durden decomposition is used in various applications since it is easy to understand and accomplish (Zhang S. 2014).

In Freeman-Durden decompostion, pixels are divided into three scattering categories: double bounce, volume, and surface based on the dominance in backscattering power. However, the great mass of pixels possess of mixed machnism in pratical investigation.
Freeman decomposition, entropy Hp and anisotropy Ap: Decompose each pixel by Freeman-Durden decomposition, and compute scattering powers, Ps, Pd and Pv, and then calculate scattering power entropy Hp and anisotropy Ap (Yang W.).

18.2.10.2 Yamaguchi

The Yamaguchi Decomposition is based on physical scattering models of microwaves. In these algorithms, the covariance or the coherency matrix is separated into several basic models corresponding to different physical scattering mechanisms in the real world.

In the Yamaguchi Decomposition, the coherency matrix is decomposed as a weighted sum of four types of scattering models, namely the surface scattering, the double-bounce scattering, the volume scattering, and the helix scattering model (Shan Z. 2012).

The modified Yamaguchi four-component scattering power decomposition method with a rotation concept of 3 x 3 coherency matrix [T] about line of sight is evaluated. It has been found that the modified Yamaguchi four-component scattering power decomposition (4-CSPD) method significantly improved the decomposition results as compared to original 4-CSPD by the minimizing the cross-polarized (HV) components. This modified 4-CSPD leads the enhancement in the double bounce scattering and surface scattering components and also avoids the over-estimation problem in volume scattering component as compared to original 4-CSPD from the sloped terrain (Singh G.).

Yamaguchi 4- component has one additional scattering mechanism that is helix. Helix scattering often appears in complex urban areas where as disappears in almost all natural distributed scenarios.

18.2.10.3 Van Zyl

A comparative study has indicated that Van Zyl decomposition gives better classification accuracy than other decomposition techniques. Many scientists think that VanZyl decomposition contributes a significant part to the improvement of classification.

It is clearly seen that Van Zyl decomposition gives better accuracy than Freeman decomposition. Van Zyl decomposition gives the best results than all these decomposition techniques (Turkar V. 2011).

The van Zyl decomposition both decompose the covariance matrix into three types of scattering mechanisms: single bounce scattering with an odd number of bounces (surface scatterer), dihedral reflection with an even number of bounces (double bounce or dihedral scatterer), and randomly oriented dipole scatter (diffuse or volume scatterer) (Kong M. 2014).

The van Zyl method is a model-based decomposition of the covariance or coherency matrix. This method classifies samples or groups of averaged samples as odd-bounce, even-bounce, or diffuse scatterers. This classification is based on the principle that scatterers of simple geometrical structures have primarily a co-pol response, but the number of bounces or reflections that the radar signal experiences creates a recognizable phase difference between the HH and the VV channels (the relative phase changes by 180 degrees for every bounce).

A van Zyl classification decomposes the image into primitive reflector types that correspond to elements of objects of interest. Further classification can consist of proximal combinations of those reflector types to identify objects.

The van Zyl classification does not retain information about the non-dominant reflection mechanisms for each pixel (PCI Geomatics, 2015).

The Van Zyl decomposition was first introduced using a general description of the 3x3 convariance C3 matrix for azimuthally symmetrical natural terrain in the

$$\boldsymbol{C}_3 = \sum_{i=1}^{i=3} \lambda_i \underline{\boldsymbol{u}}_i \cdot \underline{\boldsymbol{u}}_i^{*\mathrm{T}}$$
$$= \Lambda_1 \begin{bmatrix} |\alpha|^2 & 0 & \alpha \\ 0 & 0 & 0 \\ \alpha^* & 0 & 1 \end{bmatrix} + \Lambda_2 \begin{bmatrix} |\beta|^2 & 0 & \beta \\ 0 & 0 & 0 \\ \beta^* & 0 & 1 \end{bmatrix} + \Lambda_3 \begin{bmatrix} 0 & 0 & 0 \\ 0 & 1 & 0 \\ 0 & 0 & 0 \end{bmatrix}$$

with:

$$\Lambda_1 = \lambda_1 \left[\frac{\left(\mu - 1 + \sqrt{\Delta}\right)^2}{\left(\mu - 1 + \sqrt{\Delta}\right)^2 + 4|\rho|^2} \right] \quad \alpha = \frac{2\rho}{\mu - 1 + \sqrt{\Delta}}$$
$$\Lambda_2 = \lambda_2 \left[\frac{\left(\mu - 1 - \sqrt{\Delta}\right)^2}{\left(\mu - 1 - \sqrt{\Delta}\right)^2 + 4|\rho|^2} \right] \quad \beta = \frac{2\rho}{\mu - 1 - \sqrt{\Delta}}$$
$$\Lambda_3 = \lambda_3$$

The van Zyl decomposition thus shows that the first two eigenvectors represent equivalent scattering matrices that can be interpreted in terms of odd and even numbers of reflections. The expression given in Equation (above) and obtained from an eigenvector/eigenvalue analysis of 3x3 Hermitian-averaged covariance C3 matrix corresponds to the starting point of another class of target decomposition theorems called the model-based decompositions (Lee J.-S. 2009).

18.2.11 Wishart Classification

This program creates binary and bitmap image files resulting from the segmentation of polarimetric data using the Wishart H-Alpha and Wishart H-A-Alpha schemes. The Wishart polarimetric classification scheme performs a

Maximum Likelihood (ML) statistical segmentation of a polarimetric data sets based on the multivariate complex Wishart probability density function of second order matrix representations. An optimal segmentation necessitates maximizing a global ML function over the entire polarimetric data set and requires an unreasonable amount of time. A suboptimal solution consists in iteratively optimising this function using a k-mean clustering algorithm. It is well known that such an algorithm may get stuck in local minima and is then highly sensitive to the initialisation conditions. It was found that an initialisation of the different clusters using the results of the H-Alpha classification procedures led to satisfying and stable results (J.S. Lee et al.). A similar ML segmentation scheme explicitly including Anisotropy related information may be built from the Wishart statistics and led to improved segmentation results (López-Martínez C. 2005).

19. RESULTS

19.1 Photointerpretation

Humans are adept at visually interpreting data. We can distinguish millions of colors, several shades of gray, and have a demonstrated ability to identify water, vegetation, and urban forms on several types of imagery.

There are limits to a person's ability to distinguish small differences in color. We are especially limited in our resolution of shades of gray. If data are collected using 256 shades of gray, but an analyst can only distinguish 8-10 (optimistically) of them, a great deal of information is potentially lost. The human interpreter is outpaced by the precision of the data. Computers, however, have no trouble distinguishing 256 shades of gray.

Each one is individually recognizable. And, the analyst has control over the conputer's presentation of the data. She can group it any way she pleases, extract a portion of it, or display it in false color. Data sets can also be combined, compared, and contrasted with more ease and precision (not to mention speed) than if the task were left to humans alone.

Human interpretations are highly subjective, hence, not perfectly repeatable. Conversely, results generated by computer--even when erroneous--are usually repeatable.

When very large amounts of data are involved (a series of photos of an orange grove taken at 5 day intervals over an entire growing season) the computer may be better suited to managing the large body of detailed (and tedious) data (Crum S. 1995).

In order to take advantage of and make good use of remote sensing data, we must be able to extract meaningful information from the imagery. This brings us to the topic of discussion in this chapter - interpretation and analysis - the sixth element of the remote sensing process which we defined in Chapter 1. Interpretation and analysis of remote sensing imagery involves the identification and/or measurement of various targets in an image in order to extract useful information about them. Targets in remote sensing images may be any feature or object which can be observed in an image, and have the following characteristics:

- Targets may be a point, line, or area feature. This means that they can have any form, from a bus in a parking lot or plane on a runway, to a bridge or roadway, to a large expanse of water or a field.

- The target must be distinguishable; it must contrast with other features around it in the image.

Much interpretation and identification of targets in remote sensing imagery is performed manually or visually, i.e. by a human interpreter. In many cases this is done using imagery displayed in a pictorial or photograph-type format, independent of what type of sensor was used to collect the data and how the data were collected. In this case we refer to the data as being in analog format. As we discussed in

Chapter 1, remote sensing images can also be represented in a computer as arrays of pixels, with each pixel corresponding to a digital number, representing the brightness level of that pixel in the image. In this case, the data are in a digital format. Visual interpretation may also be performed by examining digital imagery displayed on a computer screen. Both analogue and digital imagery can be displayed as black and white (also called monochrome) images, or as colour by combining different channels or bands representing different wavelengths.

When remote sensing data are available in digital format, digital processing and analysis may be performed using a computer. Digital processing may be used to enhance data as a prelude to visual interpretation. Digital processing and analysis may also be carried out to automatically identify targets and extract information completely without manual intervention by a human interpreter. However, rarely is digital processing and analysis carried out as a complete replacement for manual interpretation. Often, it is done to supplement and assist the human analyst.

Manual interpretation and analysis dates back to the early beginnings of remote sensing for air photo interpretation. Digital processing and analysis is more recent with the advent of digital recording of remote sensing data and the development of computers. Both manual and digital techniques for interpretation of remote sensing data have their respective advantages and disadvantages. Generally, manual interpretation requires little, if any, specialized equipment, while digital analysis requires specialized, and often expensive, equipment. Manual interpretation is often limited to analyzing only a single channel of data or a single image at a time due to the difficulty in performing visual interpretation with multiple images. The computer environment is more amenable to handling complex images of several or many channels or from several dates. In this sense, digital analysis is useful for simultaneous analysis of many spectral bands and can process large data sets much faster than a human interpreter. Manual interpretation is a subjective process, meaning that the results will vary with different interpreters. Digital analysis is based on the manipulation of digital numbers in a computer and is thus more objective, generally resulting in more consistent results. However, determining the validity and accuracy of the results from digital processing can be difficult.

It is important to reiterate that visual and digital analyses of remote sensing imagery are not mutually exclusive. Both methods have their merits. In most cases, a mix of both methods is usually employed when analyzing imagery. In fact, the ultimate decision of the utility and relevance of the information extracted at the end of the analysis process, still must be made by humans (NRC, 2016).

Speckle Noise

Unlike optical images, radar images are formed by coherent interaction of the transmitted microwave with the targets. Hence, it suffers from the effects of **speckle noise** which arises from coherent summation of the signals scattered from ground scatterers distributed randomly within each pixel. A radar image appears more noisy than an optical image. The speckle noise is sometimes suppressed by applying a **speckle removal filter** on the digital image before display and further analysis.

Backscattered Radar Intensity

A single radar image is usually displayed as a grey scale image, such as the one shown above. The intensity of each pixel represents the proportion of microwave backscattered from that area on the ground which depends on a variety of factors: types, sizes, shapes and orientations of the scatterers in the target area; moisture content of the target area; frequency and polarisation of the radar pulses; as well as the incident angles of the radar beam. The pixel intensity values are often converted to a physical quantity called the backscattering coefficient or normalised radar cross-section measured in decibel (dB) units with values ranging from +5 dB for very bright objects to -40 dB for very dark surfaces.

Interpreting SAR Images

Interpreting a radar image is not a straightforward task. It very often requires some familiarity with the ground conditions of the areas imaged. As a useful rule of thumb, the higher the backscattered intensity, the rougher is the surface being imaged.

Flat surfaces such as paved roads, runways or calm water normally appear as dark areas in a radar image since most of the incident radar pulses are specularly reflected away.

Calm sea surfaces appear dark in SAR images. However, rough sea surfaces may appear bright especially when the incidence angle is small. The presence of oil films smoothen out the sea surface. Under certain conditions when the sea surface is sufficiently rough, oil films can be detected as dark patches against a bright background.

Trees and other vegetations are usually moderately rough on the wavelength scale. Hence, they appear as moderately bright features in the image. The tropical rain forests have a characteristic backscatter coefficient of between -6 and -7 dB, which is spatially homogeneous and remains stable in time. For this reason, the tropical rainforests have been used as calibrating targets in performing radiometric calibration of SAR images.

Very bright targets may appear in the image due to the corner-reflector or double-bounce effect where the radar pulse bounces off the horizontal ground (or the sea) towards the target, and then reflected from one vertical surface of the target back to the sensor. Examples of such targets are ships on the sea, high-rise buildings and regular metallic objects such as cargo containers. Built-up areas and many man-made features usually appear as bright patches in a radar image due to the corner reflector effect.

The brightness of areas covered by bare soil may vary from very dark to very bright depending on its roughness and moisture content. Typically, rough soil appears bright in the image. For similar soil roughness, the surface with a higher moisture content will appear brighter (CRISP 2001).

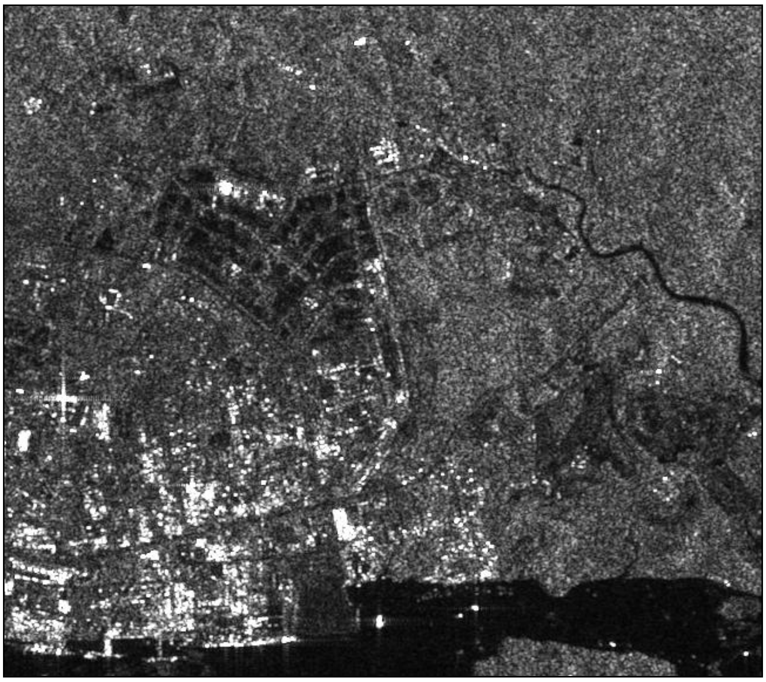

Figure 46 - ERS Sar image (Speckle example) (CRISP 2001)

The correct geologic interpretation of radar images depends critically on a knowledge of how radar waves interact with natural surfaces. There are significant differences between the microwave and more familiar optical wavelengths in the mechanics of imaging and in the measured characteristics of the target. Because of the side-looking illumination geometry, all radar images are distorted to some extent. In addition, the longer wavelength of radar makes them most sensitive to surface roughness at scales near the radar wavelength. Of secondary importance are variations in the dielectric constant of the target; this parameter is similar for dry geologic materials except metallic compounds, which may be present at high elevations on Venus (Farr T.).

By interpretation, we mean giving the spatial organization of the main cartographic elements in a SAR image: road and hydrological networks, urban areas, forest or sea areas, relief, etc (Tupin F. 1999)

Often, SAR images are really difficult to be interpreted: the presence of speckle as well as of some distortion effects, like shadowing and layover, makes the analysis of this kind of image complex (Franceschetti G.).

19.2 Results of ENVISAT Data Analysis

Figure 47 - Area of Envisat images (background- GoogleEarth)

Lee & Frost Filter Results

Below you can see the multitemporal study of an Amazon area in the state of Tocantins. Initially, we had applied few filters but when we got our results we concluded that Lee and Frost filters give the better outcomes. For this case analysis we had four different date images: one of 2006, one of 2005 and 2 referring to 2004 (April and August). For getting better results, we applied various combinations for getting our RGB images. Though, in order to test each filter and kernel results, we kept stable the date line and we altered the kernel number and the filter type each time. So, at first, concerning the results of timeless analysis, keeping stable the filter type (at first the Lee and then the Frost one) we changed each time the kernel number (from 5 to 7). Then we tried another mechanism of keeping same the kernel number and changing the filter type.

As for the results with the same filter and the different number of kernels we observed that the bigger number the kernel we apply the best and clearer results we get. So, when we increase the kernel number we achieve better speckle reduction and we can see clearly the study areas. In the maps below we can see the results of Lee filter application of kernels 5x5 and 7x7. In kernel type 5x5 the speckle phenomenon is more dominant while in the kernel 7x7 the speckle has significantly reduced but in some cases it leads to generalizations and sometimes this is not very helpful when we want to study in detail an area. Comparing different filter results, we see that there is no valuable difference between them. Moreover, it is of high importance to say that there are areas that be represented in clear colors like a frame focusing in a red feature which scatters significantly on August 2004 and not the rest of dates. This may happen because this feature has high moisture this season or that year and month was highly vegetated. The same can be observed in some green areas of May 2005 that actually are cultivated areas so in that period of time are not in fallow for sure since they scatter high signal values. Some brown or yellow areas mean that the backscattered significantly on August 2004 and May 2005 but the next year they didn’t give back strong signal. In this case, if it is about a cultivated area, it can be a land in fallow.

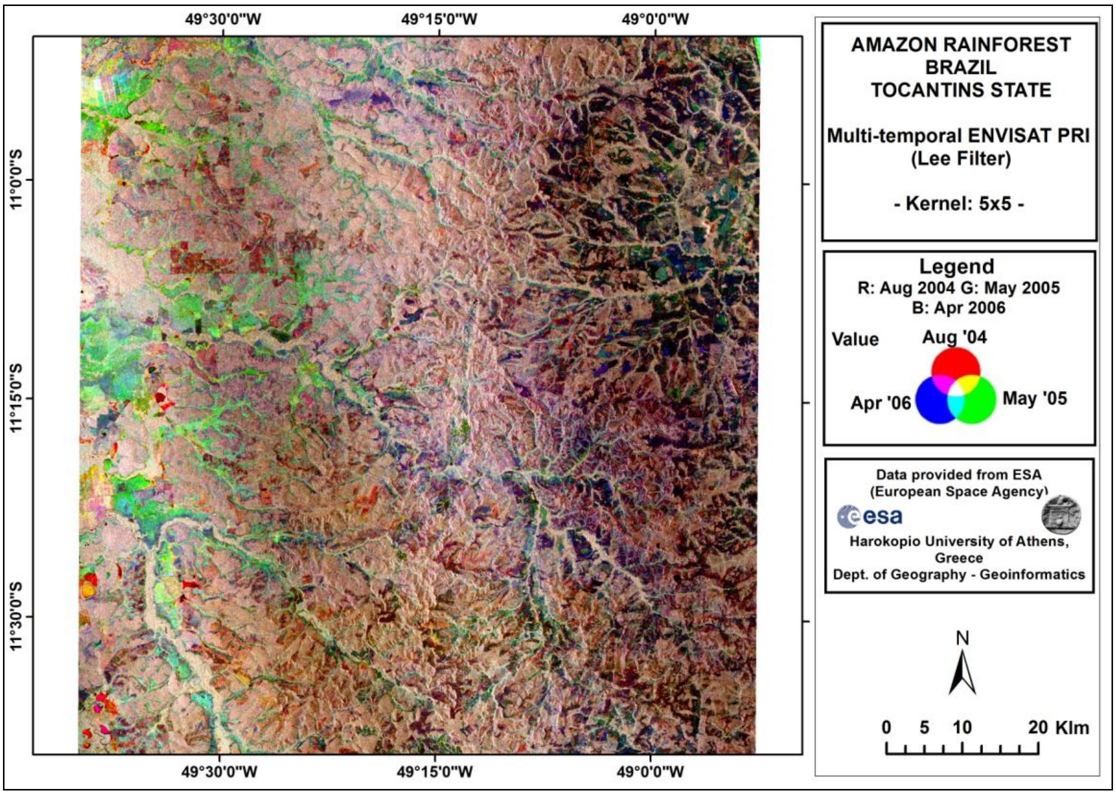

Figure 48 – Multi-temporal false color image (R:Aug2004, G:May2005, B:Apr2006), Lee Filter, Kernel 5x5

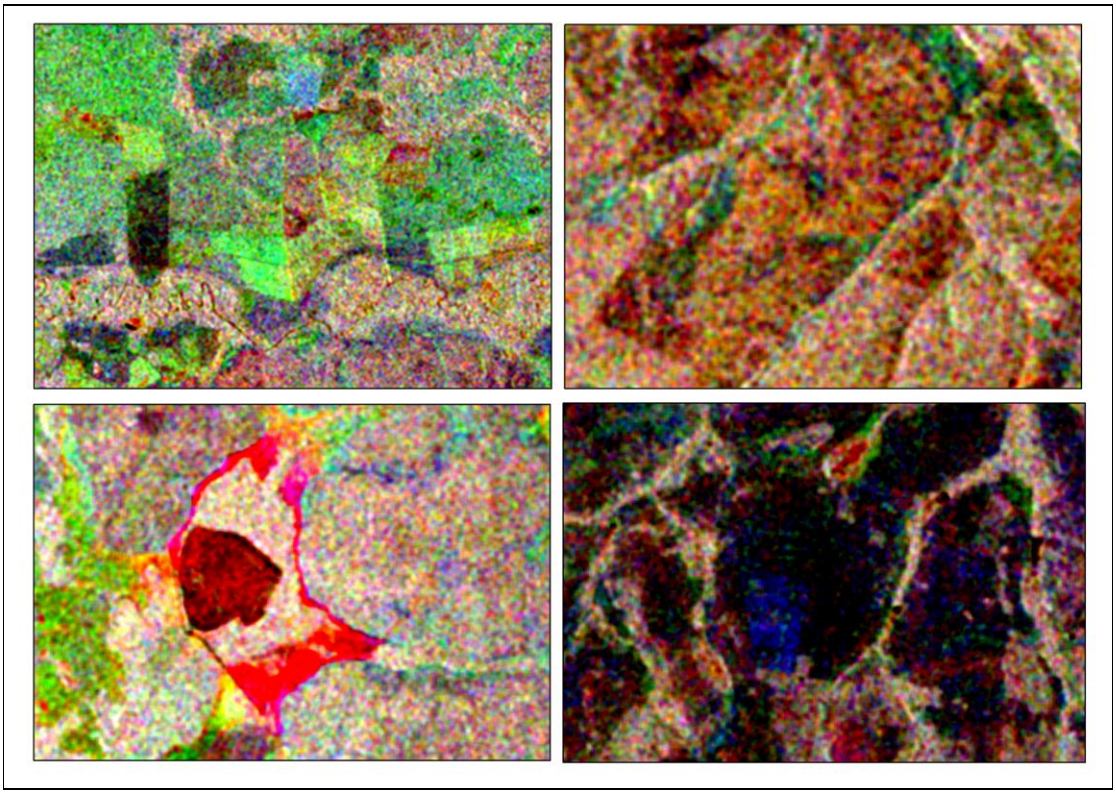

Figure 49 - Multi-temporal false color image (R:Aug2004, G:May2005, B:Apr2006), Lee Filter, Kernel 5x5, zoom areas

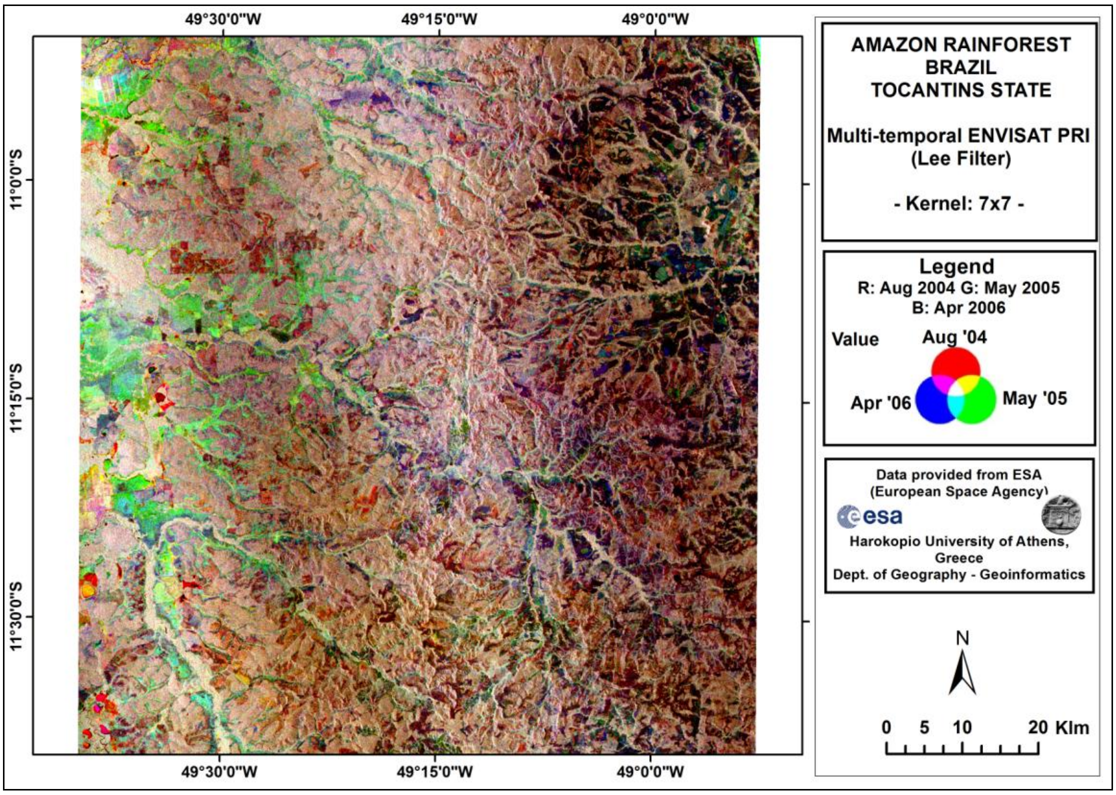

Figure 50 - Multi-temporal false color image (R:Aug2004, G:May2005, B:Apr2006), Lee Filter, Kernel 7x7

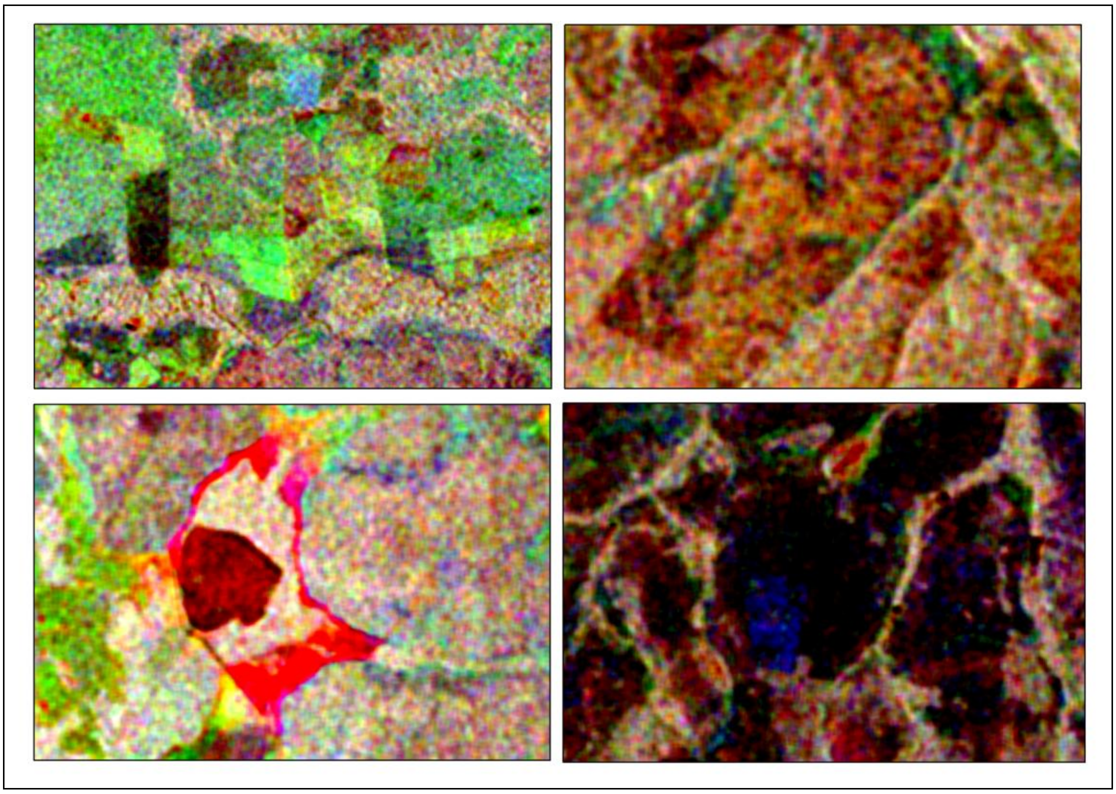

Figure 51 - Multi-temporal false color image (R:Aug2004, G:May2005, B:Apr2006), Lee Filter, Kernel 7x7, zoom areas

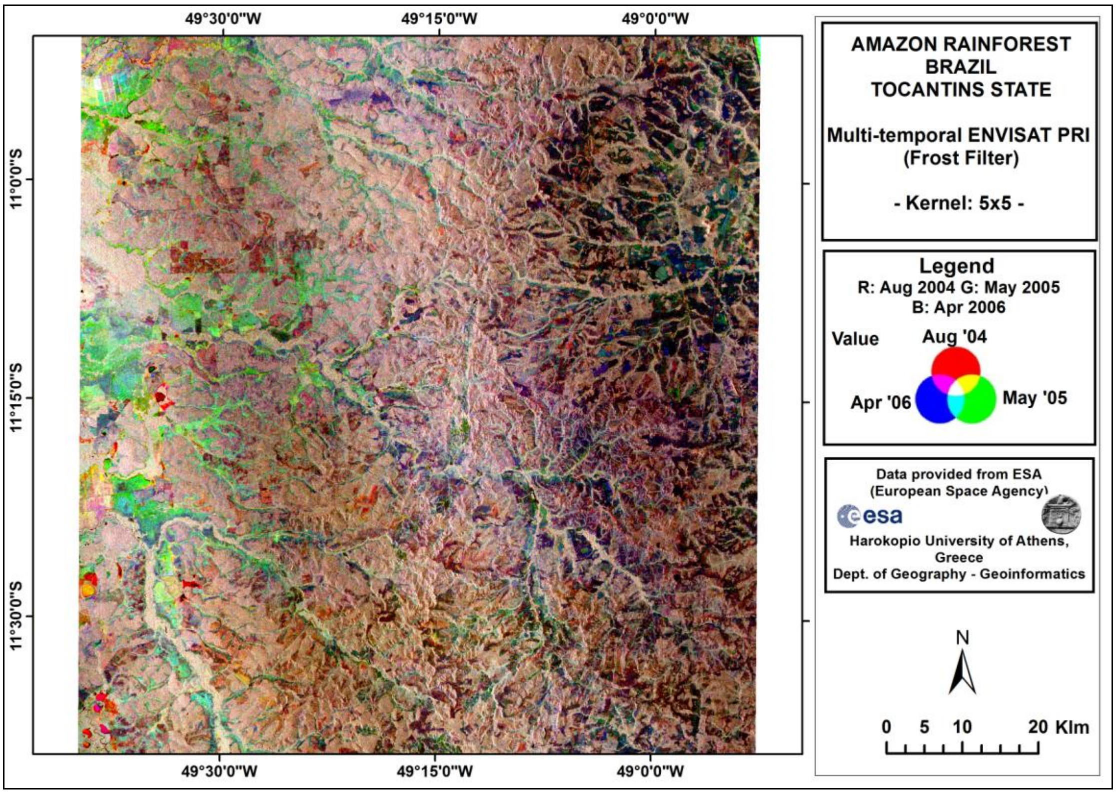

Figure 52 - Multi-temporal false color image (R:Aug2004, G:May2005, B:Apr2006), Frost Filter, Kernel 5x5

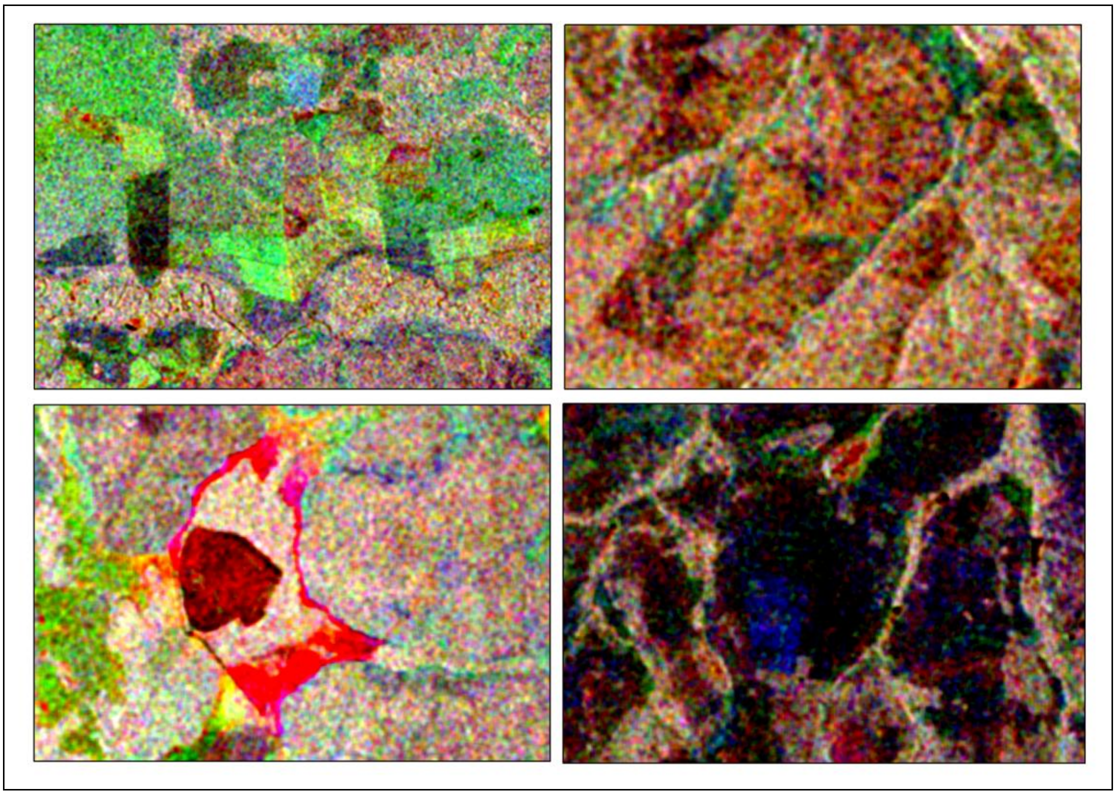

Figure 53 - Multi-temporal false color image (R:Aug2004, G:May2005, B:Apr2006), Frost Filter, Kernel 5x5, zoom areas

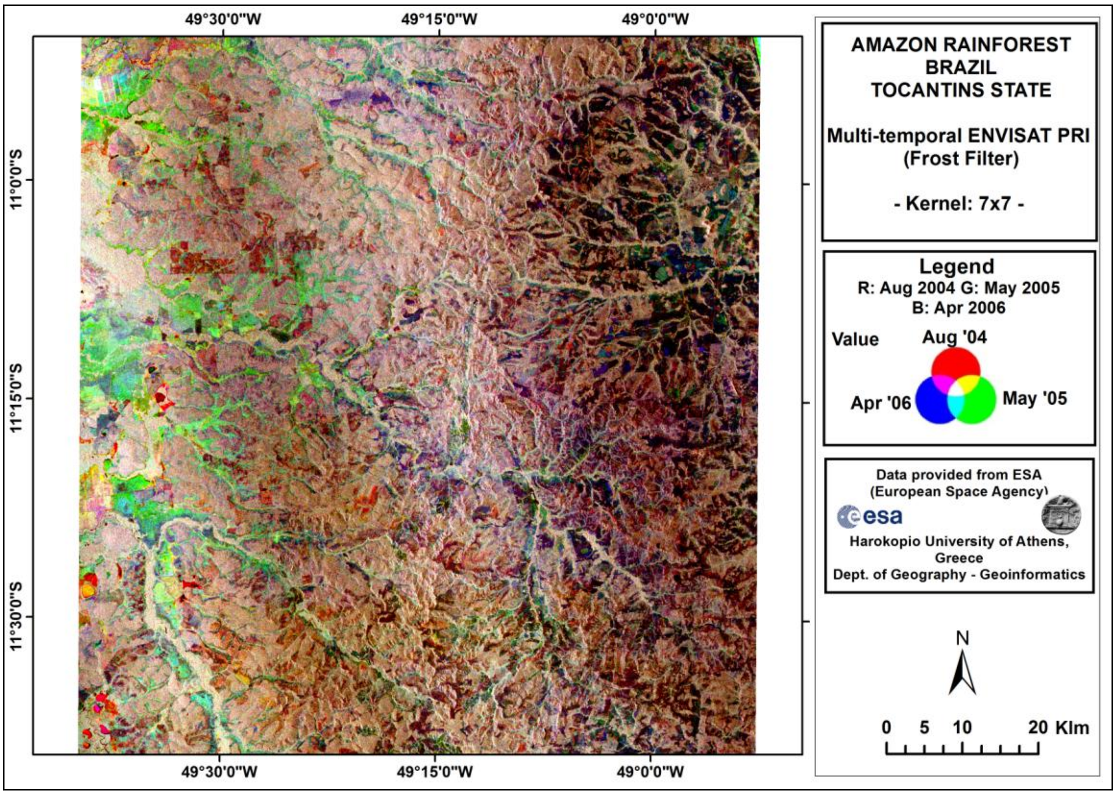

Figure 54 - Multi-temporal false color image (R:Aug2004, G:May2005, B:Apr2006), Frost Filter, Kernel 7x7

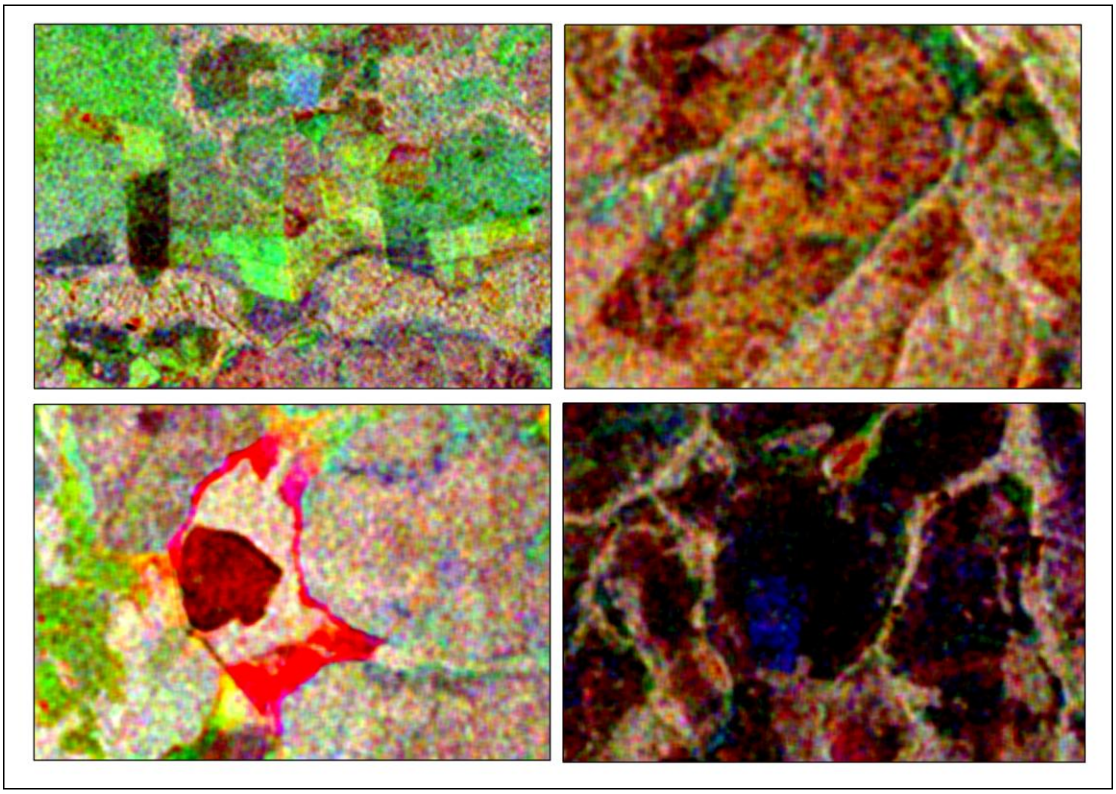

Figure 55 - Multi-temporal false color image (R:Aug2004, G:May2005, B:Apr2006), Frost Filter, Kernel 7x7, zoom areas

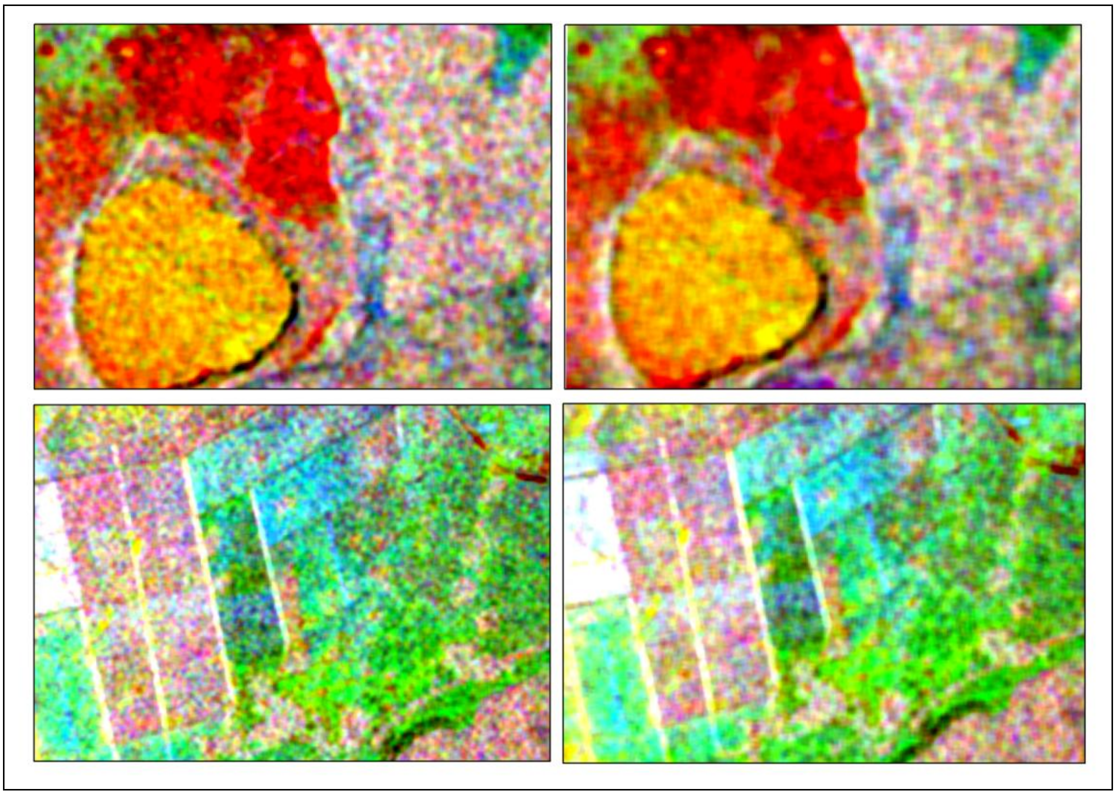

Figure 56 - Multi-temporal false color image (R:Aug2004, G:May2005, B:Apr2006), Frost Filter, Kernel 5x5 (on the left) 7x7 (on the right), zoom areas

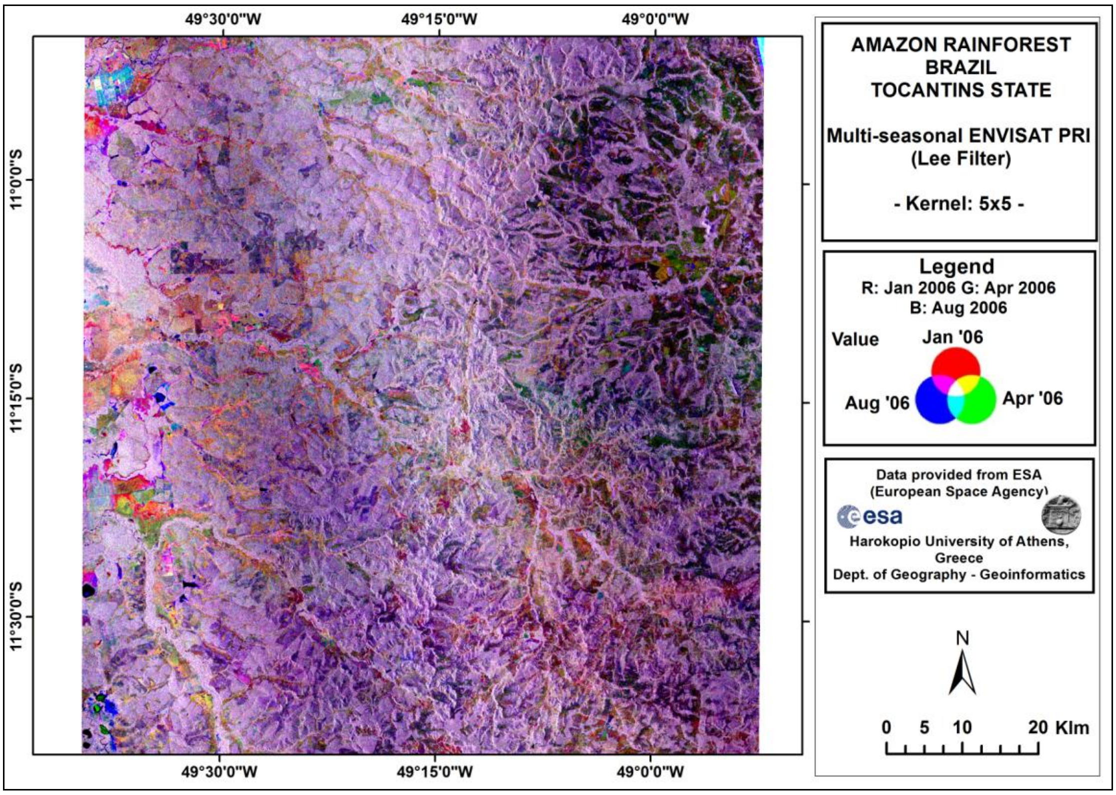

Figure 57 - Multi-seasonal false color image (R:Jan2006, G:Apr2006, B:Aug2006), Lee Filter, Kernel 5x5

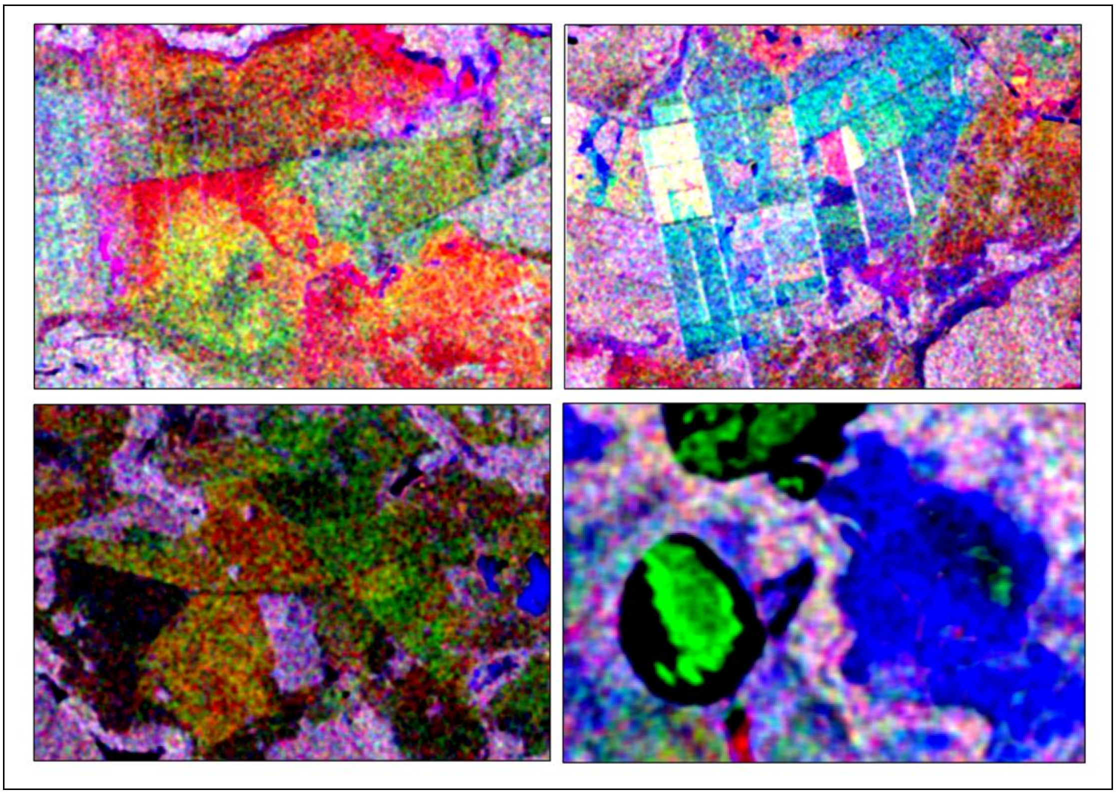

Figure 58 - Multi-seasonal false color image (R:Jan2006, G:Apr2006, B:Aug2006), Lee Filter, Kernel 5x5, zoom areas

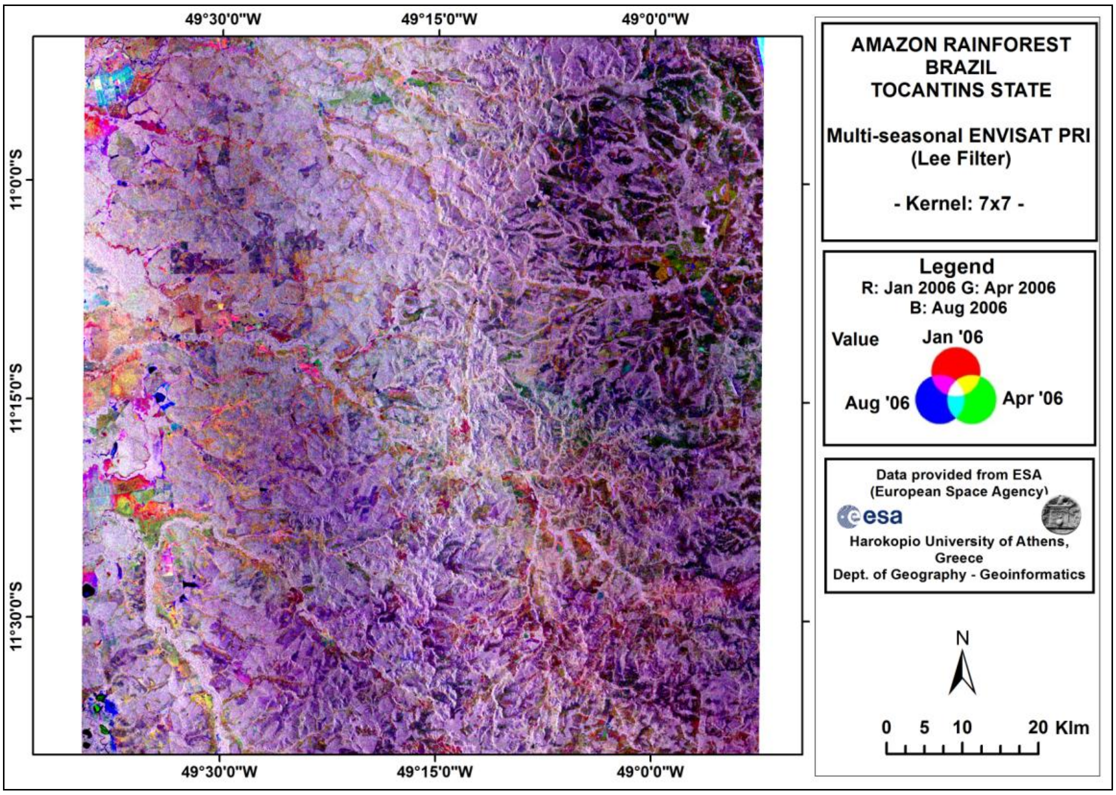

Figure 59 - Multi-seasonal false color image (R:Jan2006, G:Apr2006, B:Aug2006), Lee Filter, Kernel 7x7

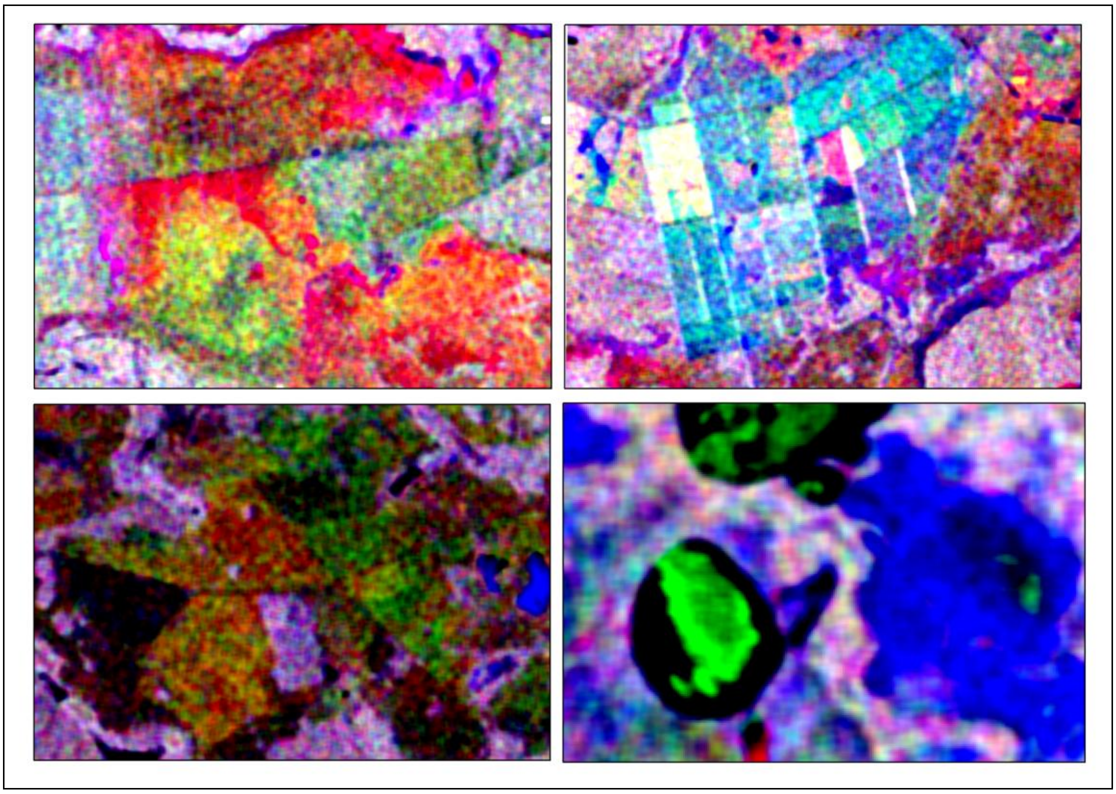

Figure 60 - Multi-seasonal false color image (R:Jan2006, G:Apr2006, B:Aug2006), Lee Filter, Kernel 7x7, zoom areas

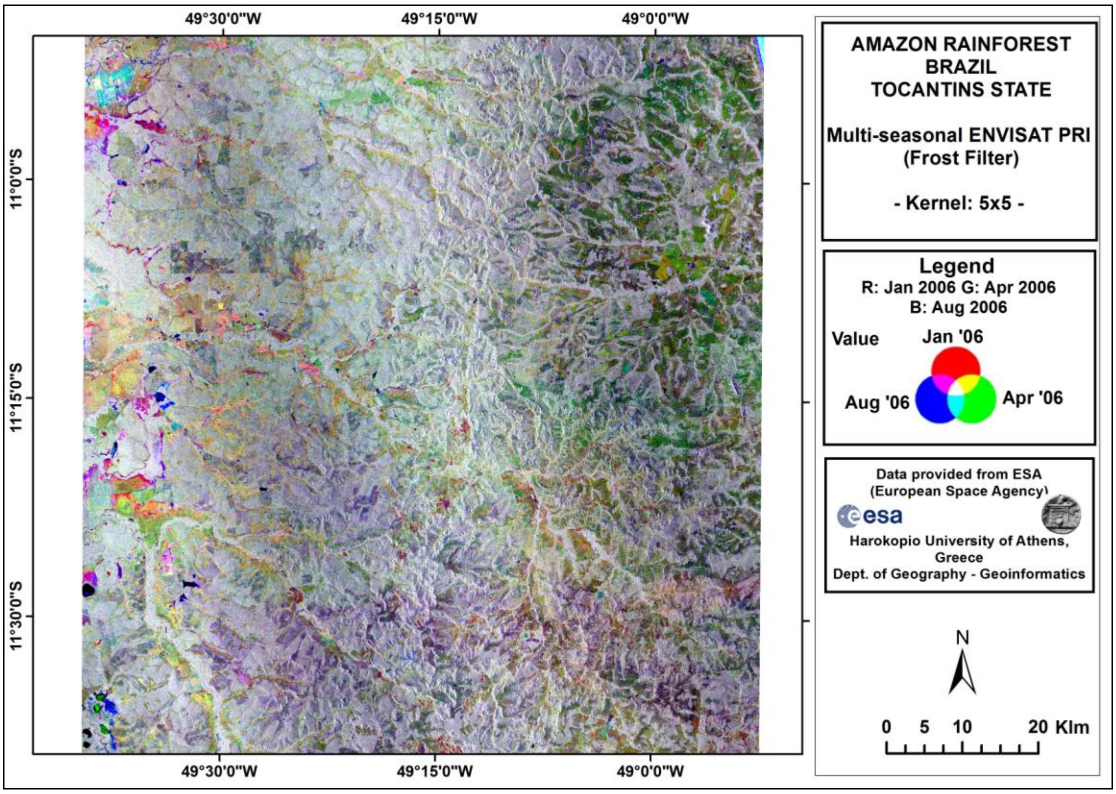

Figure 61 - Multi-seasonal false color image (R:Jan2006, G:Apr2006, B:Aug2006), Frost Filter, Kernel 5x5

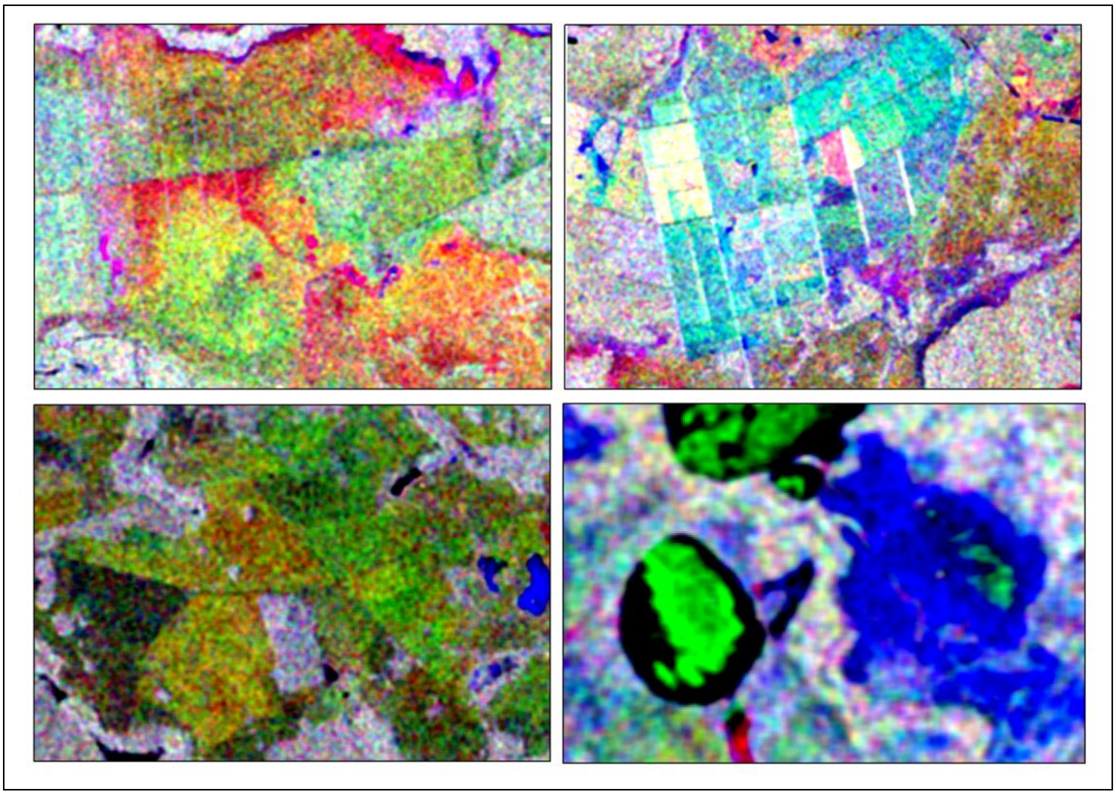

Figure 62 - Multi-seasonal false color image (R:Jan2006, G:Apr2006, B:Aug2006), Frost Filter, Kernel 5x5, zoom areas

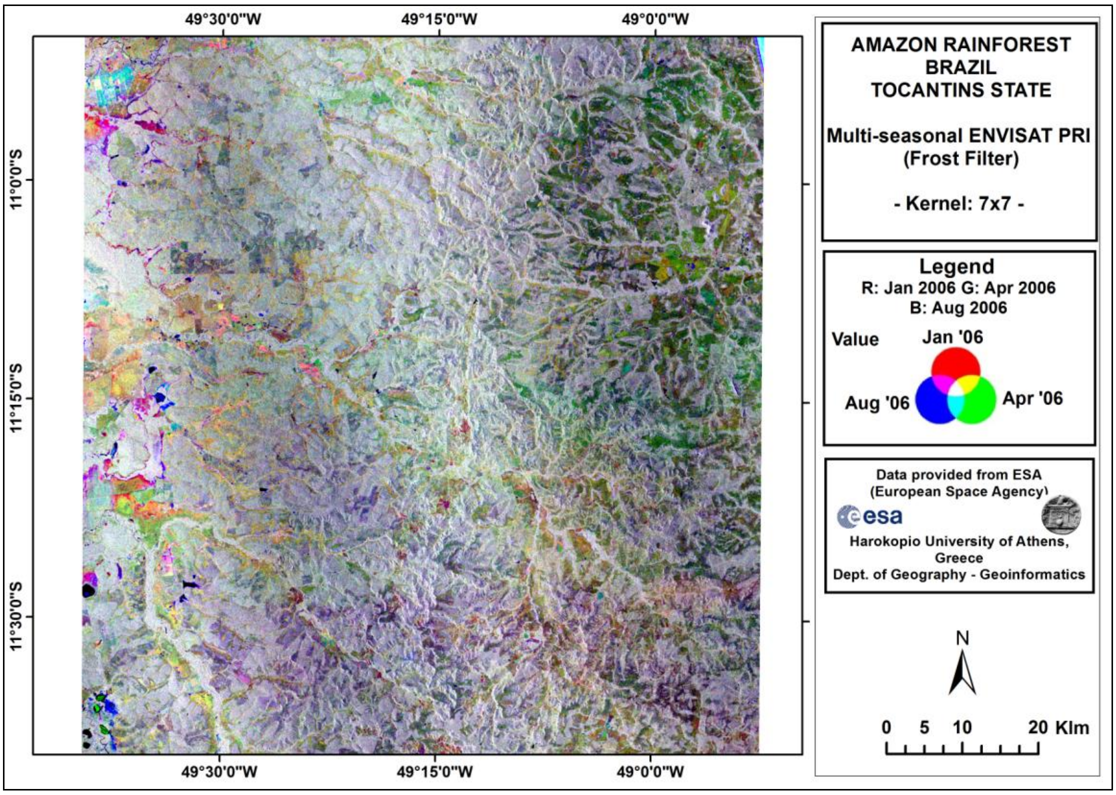

Figure 63 - Multi-seasonal false color image (R:Jan2006, G:Apr2006, B:Aug2006), Frost Filter, Kernel 7x7

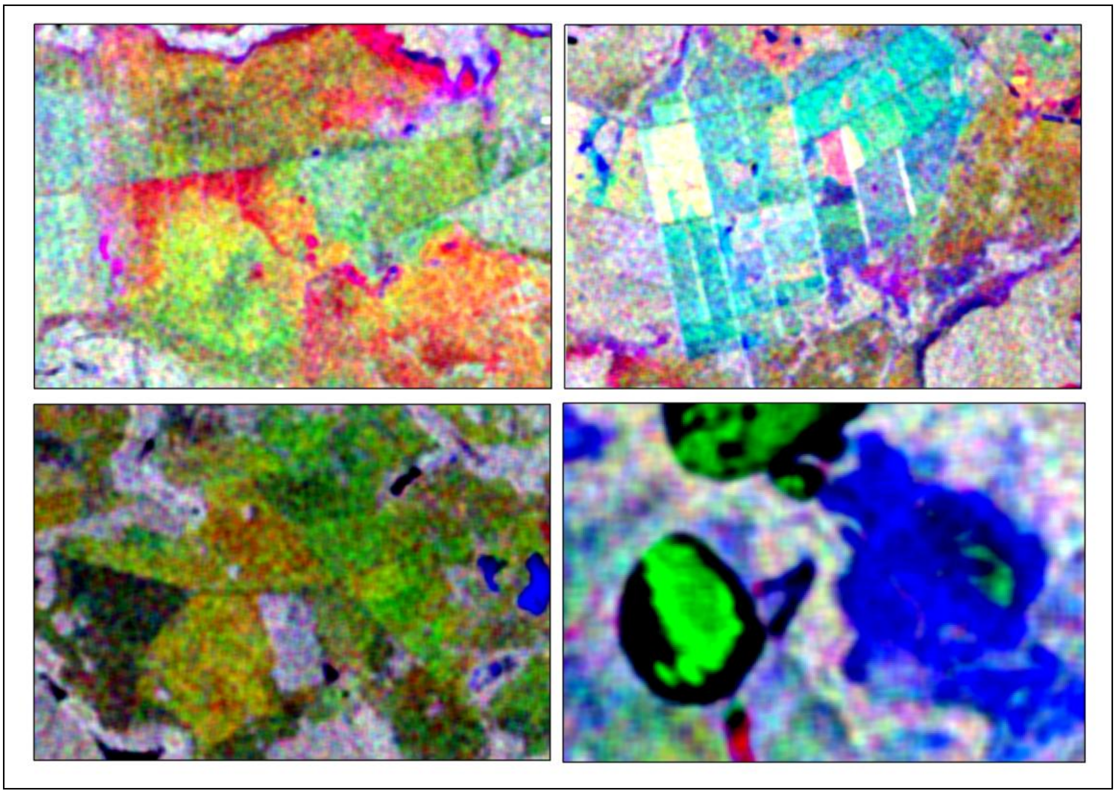

Figure 64 - Multi-seasonal false color image (R:Jan2006, G:Apr2006, B:Aug2006), Frost Filter, Kernel 7x7, zoom areas

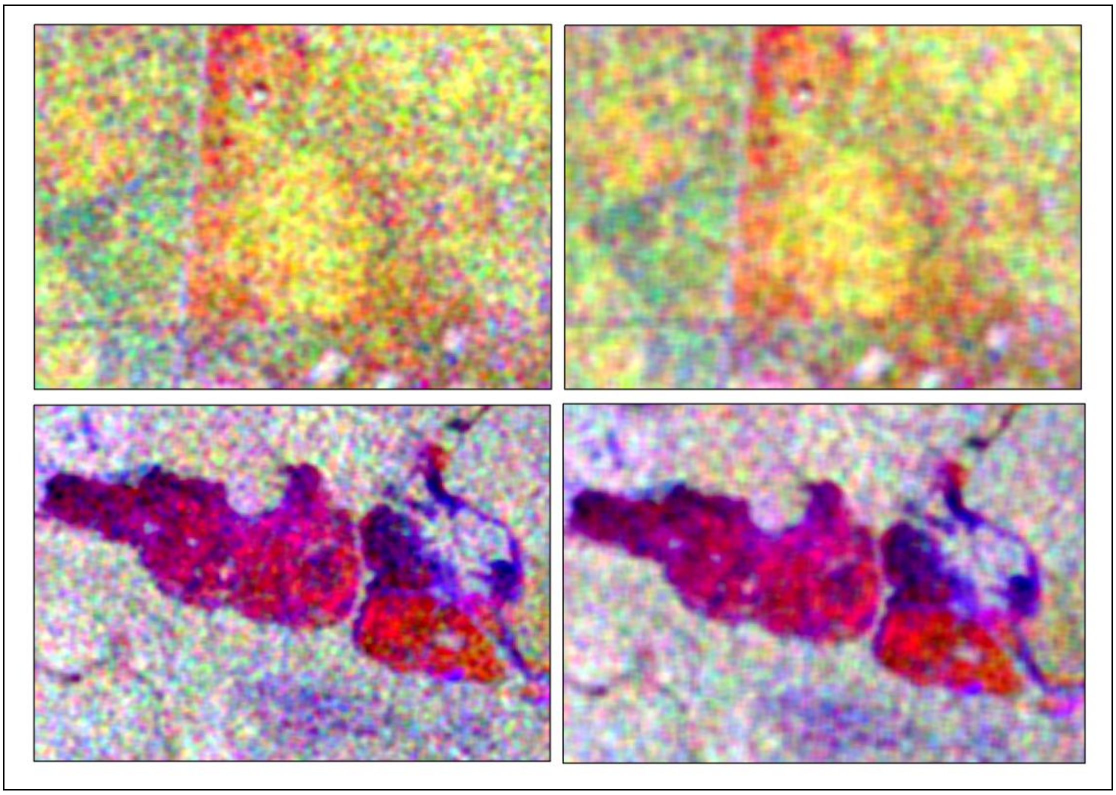

Figure 65 - Multi-seasonal false color image (R:Jan2006, G:Apr2006, B:Aug2006), Frost Filter, Kernel 5x5 (on the left) 7x7 (on the right), zoom areas

The same results can be observed in multi-seasonal analysis too. There we apply a RGB combination of images of the same year but of different month (season-winter, spring, summer). In figures 59, 61, 63, 65 we see some probably cultivated areas presented in cyan color. This means that spring-summer time they backscattered significantly while on January not. So, if it is about cultivated areas maybe on April and August are more moisturing or have more dense vegetation. Here, we observe the same phenomenon as previously of having regions with single colors (green, blue) which means that scatter high signal values in one special month and only. In figure 66, we can observe the different speckle reduction of Frost filter with kernel 5x5 and 7x7. In this case, maybe we would choose Kernel 5x5 although give a “noise result” because the 7x7 one leads to generalizations and information reduction.

Concluding, we summarize that this study area presents a high activity since there exist big differences in time (between different years but different months of the same year too). Maybe, it is about a fertile land and this is the reason why has so many towns and villages.

19.3 Results of ALOS Data Analysis

19.3.1 H-A-alpha Decomposition

As we previously write we used 24 out of 29 scenes that we initially had. The reason was that 5 of 29 images showed problems in processing so they were rejected. Some of the scenes refer to cultivated regions and other ones contain virgin forest areas and residential villages. Moreover, during the last inspect of the area we decided to show, in this case study, the results of an area located in the center Brazil country and in the south part of Amazon forest. The satellite scene located in this area is of 02 December 2010 and covers part of the Tocantins state. This happens because we thought that the scenes covering an area with cultivated and virgin forestland too would be an interesting case. Plus, we initially suggested that we apply an analysis of an area covered by Envisat and Alos images simultaneously but unfortunately there was a small distance between the 2 datatype images so this couldn't happen.

The scene that is going to be analyzed in this study is one of Tocantins state acquired the December of 2010. As we have previously described Tocantins is an inland state of north-central Brazil. Some of the geographical characteristics that are contained inside the Alos range are Municipalities: Cachoeirinha and Duere, Boa Nova and Ponta Pora on the north, Gurupi on the southeast, Cariri do Tocantins on the south and Farmoso do Araguaia on the southwest which is the largest municipality by area in the state. Moreover a part of Xarante river runs through this state and a small area of Comprida lake on the southeast of the scene.

In this part, we must say that there is a large amount of results that came up from this study so we decided to show the results that refer to 2 types of Polarimetric Decompositions; H-A-alpha decomposition that is one of the most frequently used ones and Freeman-Durden decomposition that has been proved ideal for vegetation analysis and classification according to many studies.

When we apply H-A-alpha polarimetric decomposition then the scattering matrix is converting to coherency matrix which is decomposed into eigenvalues and eigenvectors. It is a 3x3 matrix where the three eigenvectors represent the three different scattering mechanisms. The eigenvalues show the intensity of each mechanism respectively. So, acquiring the coherency matrix [T] which is a unitary scattering matrix, we can get important informattion about the whole scattering contribution (Vyjayanthi N. 2012).

Thus, eigenvalues give the amount of scattering contribution while the scattering type is related with the eigenvectors via the alpha angle.

Polarimetric scattering entropy H is a global measure of the distribution of the components of the scattering process. Values of entropy range from 0 to 1 and when we have H=0 means that matrix [T]-coherency matrix has only one nonzero Eigenvalue and represents one deterministic scattering process, while when we have values of H=1 means that all eigenvalues are equal and represents a scattering totally random (Vyjayanthi N. 2012). Actually, entropy indicates the relationship between the eigenvalues of each scattering mechanism.

Anisotropy is an additional component of polarimetric H-A-a classification which increases the classification accuracy. This component is related to the eigenvalues (Vyjayanthi N. 2012).

The alpha angle varies between 0^o and 90^o and identifies the type of scattering. Thus, if we have an angle of 0^o means that the scattering is related to plane surface plane while when we have an angle of 45^o it means that the scattering characteristics are those of a dipole (see figure 68). Between these values there is an irregular surface that gets values from 0^o to 45^o while on the other hand, when we have values from 45^o to 90^o the response of the ground is the result of a double bounce scatterer (see figure 67) (Vyjayanthi N. 2012).

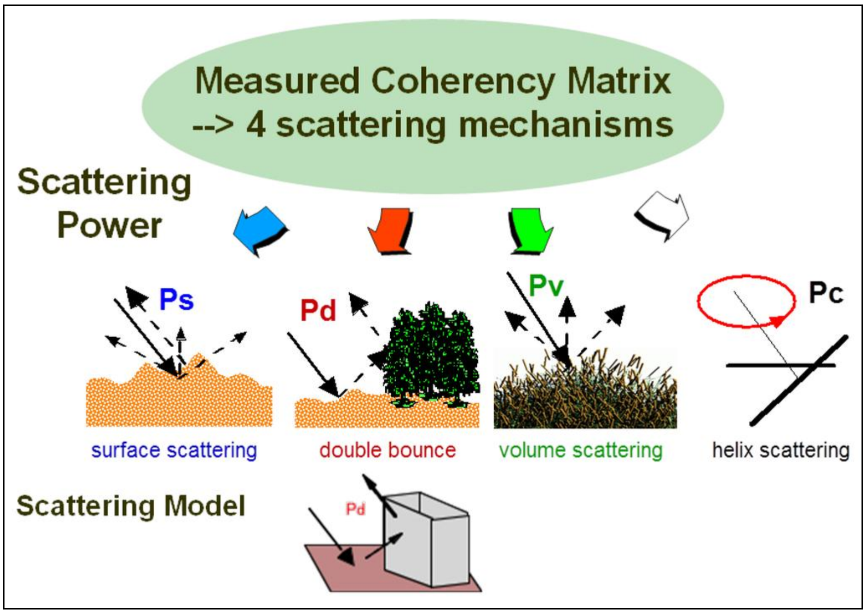

Figure 66 - Schematic diagram of the four-component scattering power decomposition with the coherency matrix. Measured scattering matrix [S] is transformed to coherency matrix [T] and is decomposed into the surface scattering power Ps, the double-bounce scattering power Pd, the volume scattering power Pv and the helix scattering power Pc. (Shibayama, 2015)

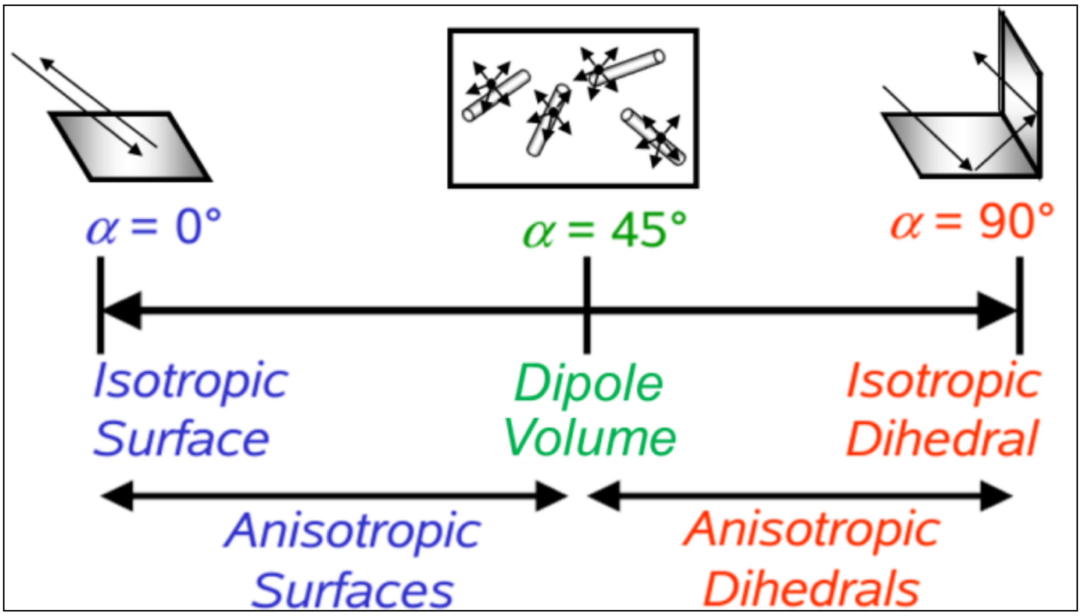

Figure 67 - Physical meaning of the dominating intrinsic scattering mechanism expressed by the mean alpha scattering angle (ranging from surface scattering α = 0 to dihedral scattering α = π/2) (Jagdhuber, 2014)

Furthermore, Cloude and Pottier, as we previously mentioned proposed an algorithm-graph that helps in identifying the polarimetric scattering mechanisms, the H-a plane (Vyjayanthi N. 2012).

This model has been employed to derive entropy, alpha and anisotropy segmentation to characterize the image in terms of its scattering mechanism. The entropy–alpha space and the associated physical scattering in terms of mean scattering process and the high or low values of entropy indicates the randomness of the target that we examine (Vyjayanthi N. 2012).

The entropy–alpha space divides the target response into eight classes (see figure 69) as we have analyzed in the theory chapters too, in accordance to the mean scattering process and the randomness of the scattering process. The basic scattering mechanism of each pixel of a polarimetric SAR image can then be identified by comparing its entropy and α parameters to fixed thresholds. The different class boundaries, in the H-α plane have been determined so far discriminating surface reflection (SR), volume diffusion (VD) and double bounce reflection (DB) along the α axis and low, medium and high degree of randomness along the entropy axis (Vyjayanthi N. 2012).

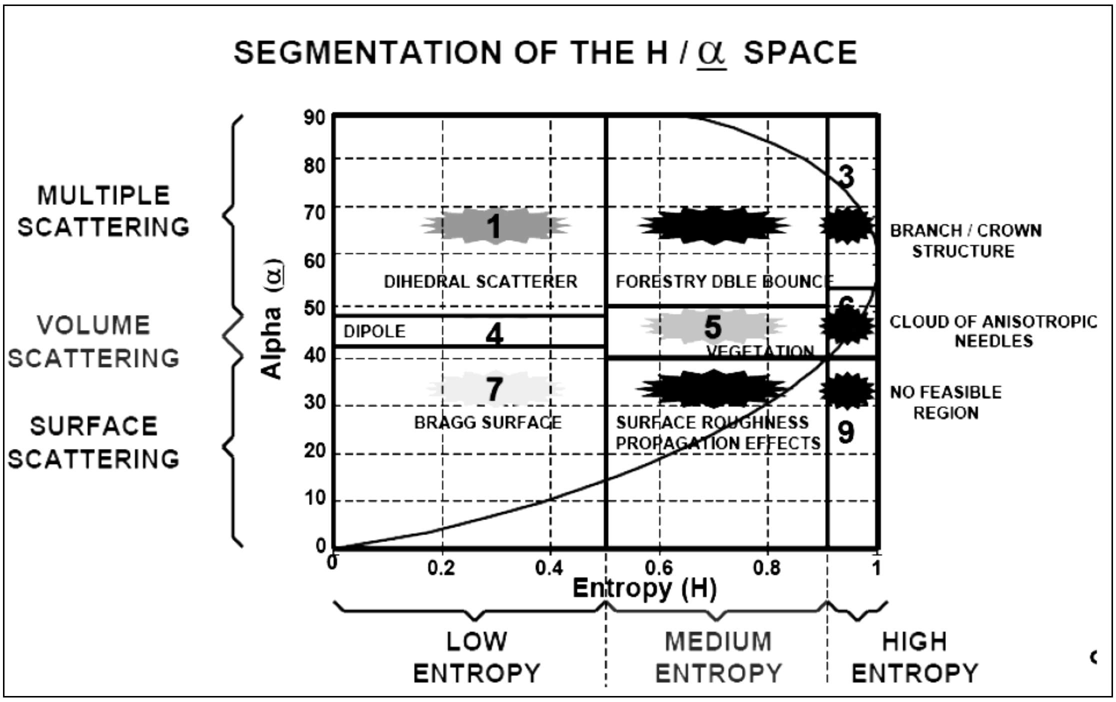

Figure 68 – Segmentation of H/a space

Segmentation in the H-α plane permits identification of scattering mechanisms in a macroscopic way. For example agricultural fields and baresoils are characterized by surface scattering. Usually, scattering over forested areas is dominated by volume scattering while urban areas are mainly characterized by double bounce scattering over surfaces (Vyjayanthi N. 2012).

This classified map is divided into nine zones: high entropy, medium entropy, low entropy and the variation of alpha angle from 0 to 90^{o}. H-Alpha classification space represents all possible random and any deterministic scattering mechanisms. When H=0, all values from $0 \leq \alpha \leq 90^{o}$ can be attained, where as for H=1, there exists only one value $\alpha = 60^{o}$ which reflects increasing disability to differentiate scattering mechanisms as the entropy increases. The nine zones in α- H classification space correspond to different scattering mechanisms: Zone 1: High entropy multiple scattering; Zone 2: High entropy vegetation scattering; Zone 3: High entropy surface scattering; Zone 4: Medium entropy surface scattering; Zone 5: Medium entropy vegetation scattering; Zone 6: Medium entropy surface scattering; Zone 7: Low entropy multiple scattering; Zone 8: Low entropy dipole scattering; Zone 9: Low entropy surface scattering (Vyjayanthi N. 2012).

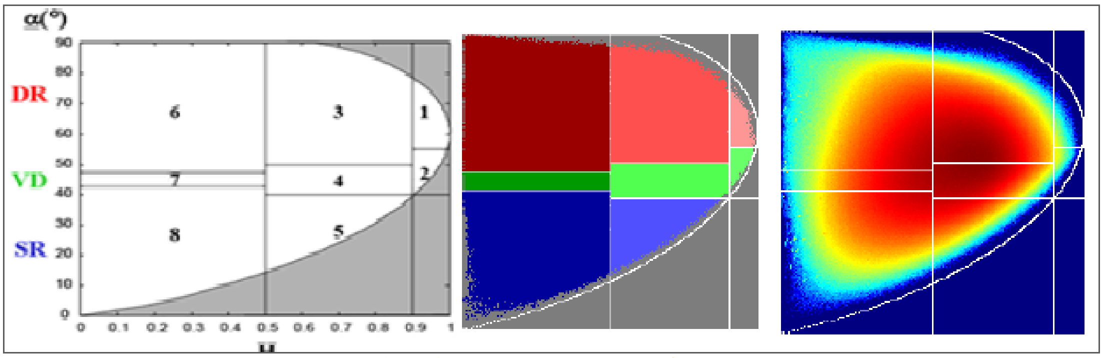

Figure 69 – Example of scattering mechanism, polarimetric data occurrence and H/a plane (Vyjayanthi N. 2012).

If the Entropy is close to '0', the alpha angle gives type of the dominant scattering mechanism for that resolution cell i.e., scattering is volume, surface or double bounce. Entropy increases as a natural measure of the inherent reversibility of the backscatter data and hence it can be used for identification of underlying scattering mechanism (Vyjayanthi N. 2012).

When the entropy–alpha space is not able to distinguish the number of scattering mechanisms and their relative dominance we can introduce anisotropy which is a measure of the number of dominant scattering mechanisms involved in the scattering process and it is feasible for it to achieve better discrimination between the different scattering classes (Vyjayanthi N. 2012).

Anisotropy is a very useful parameter because can differentiate scattering mechanisms which have different eigen-value distributions but similar entropy values. When the entropy values for two clusters are the same, a high anisotropy value show two dominant scattering mechanisms with equal chance of occurrence and a less significant third mechanism, whereas a low anisotropy value shows a dominant first scattering mechanism and two insignificant secondary mechanisms with equal importance. Anisotropy gives the homogeneity of a target with reference to the radar look direction. For homogeneous target, low anisotropy value is observed (Vyjayanthi N. 2012).

In our example, alpha angle results show that in the region that we examine we have values from 0^o to almost 73^o (72.9831^o). The fact that we have no 90^o alpha values means that in this region there are no scatterers that act like a double bounce targets and isotropic dihedrals. Actually, is about targets that behave almost (because we have no 90^o values) like a helix.

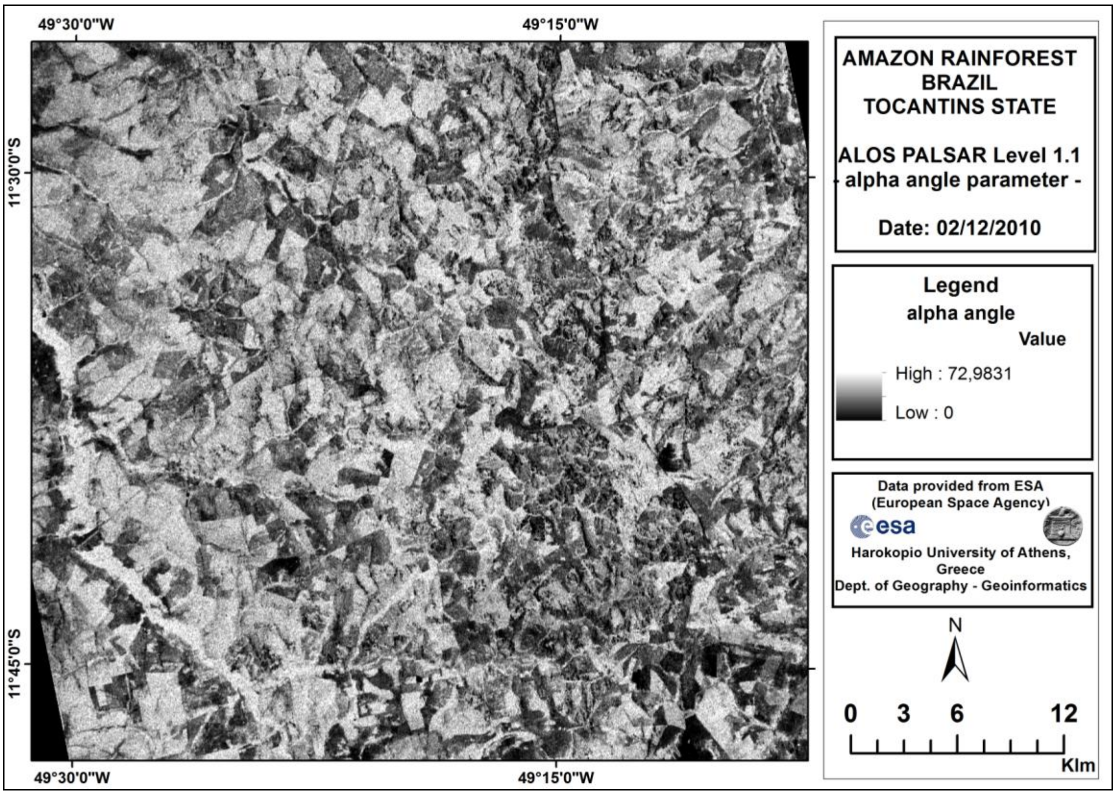

Figure 70 – a angle parameter derived from H-A-alpha decomposition, Tocantins state, Brazil

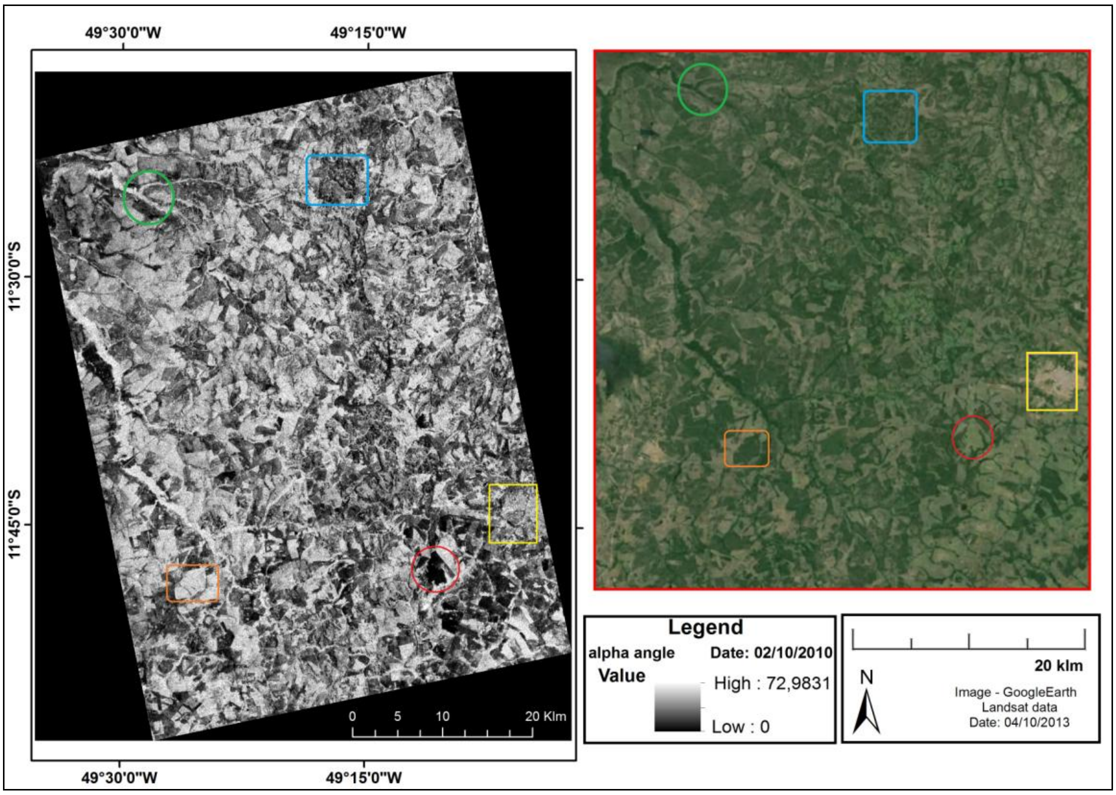

Figure 71 – Comparison of a angle result scene and GoogleEarth image

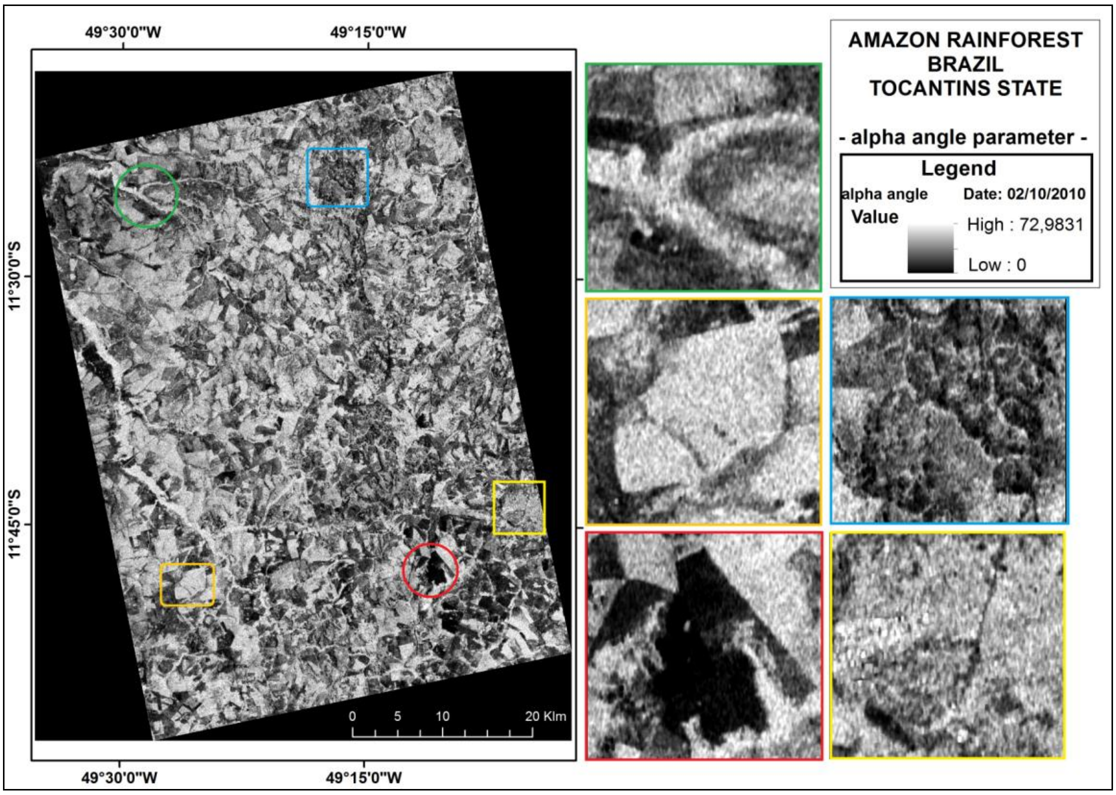

Figure 72 – Inspection of special areas with different scattering results, alpha angle parameter

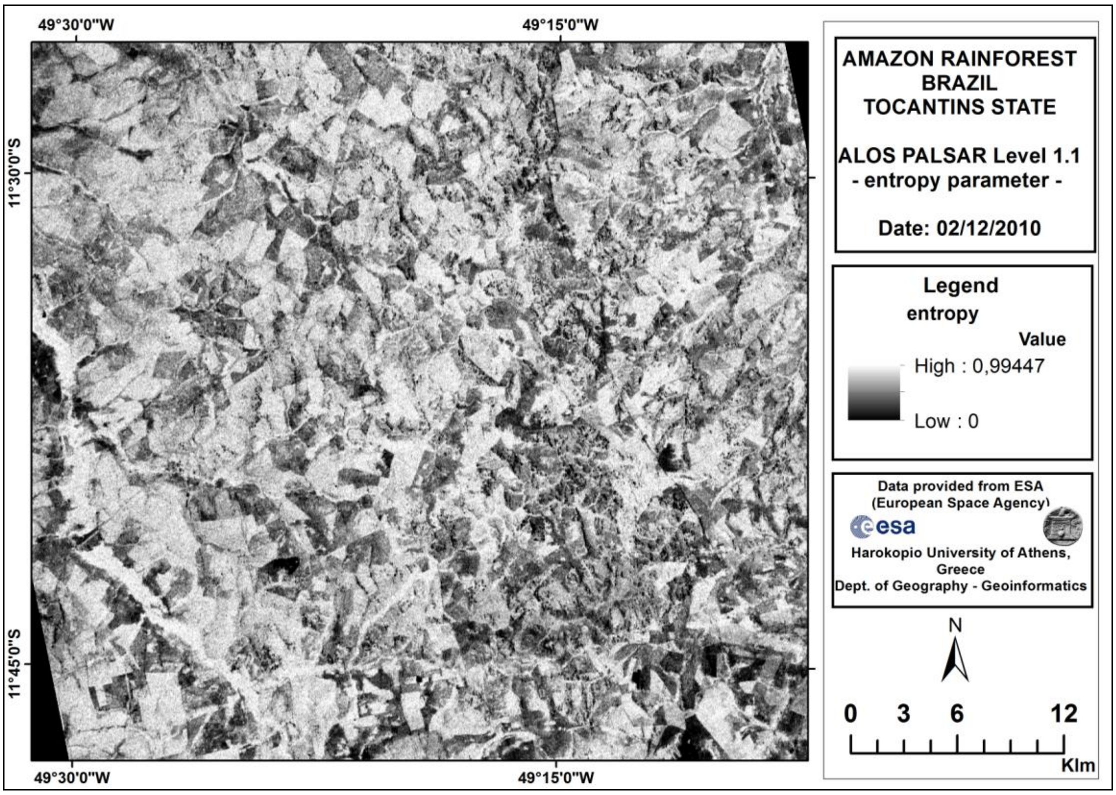

Figure 73 - entropy parameter derived from H-A-alpha decomposition, Tocantins state, Brazil

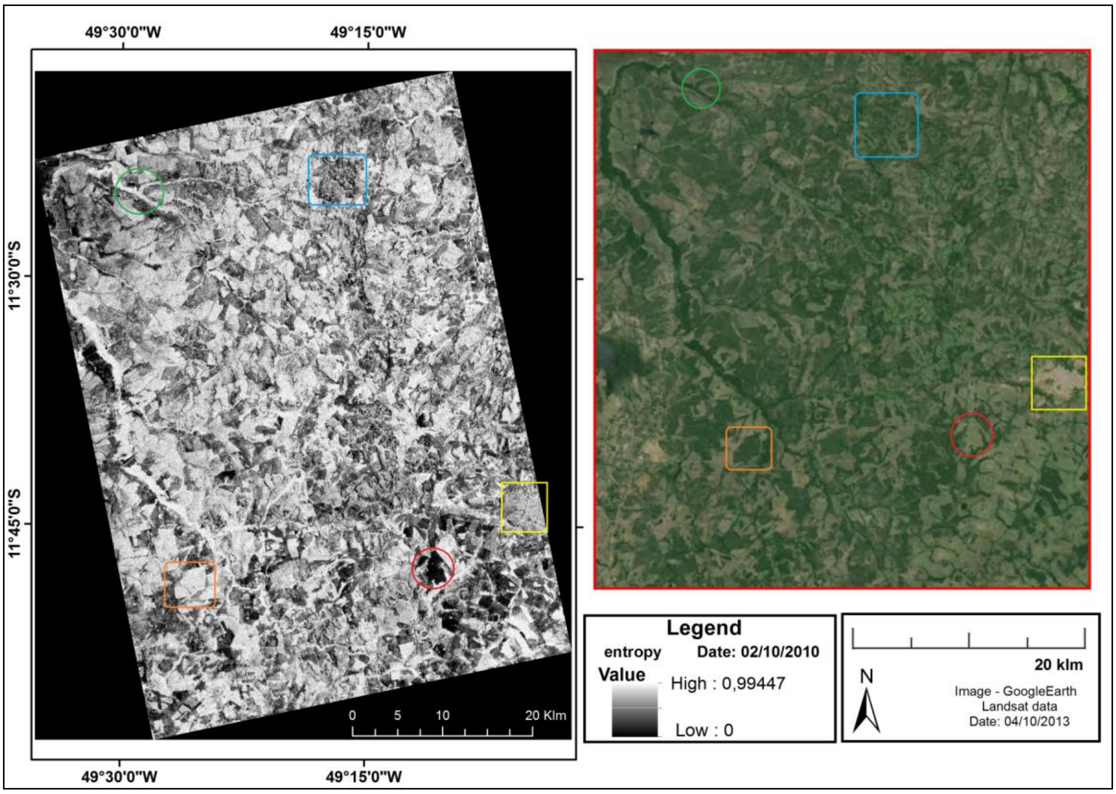

Figure 74 - Comparison of entropy result scene and GoogleEarth image

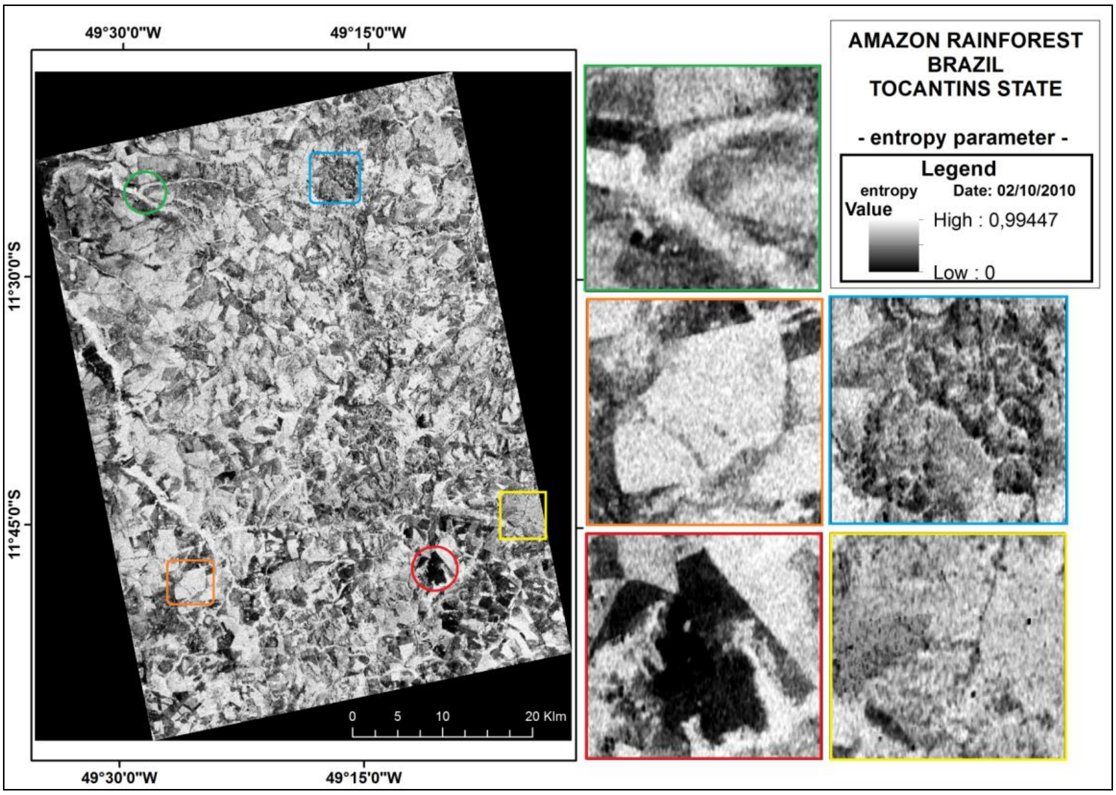

Figure 75 - Inspection of special areas with different scattering results, entropy parameter

As we can see in the maps of alpha angle (figure 71, 72 & 73), we have cited a GoogleEarth scene which shows the same area with the Alos image. We have pinpointed some areas of interest just to see how alpha angle parameter can differentiate various land characteristics. Yellow box could represent a barren land area or a part of the land with very low and poor vegetation. Though, taking into account the theory and that in this area there are values of a angle between 30^o and 50^o, we conclude that is about an urban environment since buildings and other human constructions give a high value of angle. The orange frame focuses over a vegetated area where the a angle gets values around 45 ^{o}. This means that the vegetation is not very high or dense but it is indeed a healthy vegetated area. On the contrary, in the red circle we have a barren or deforestated area with very low alpha values. It may also be a plot being in fallow. Moving to the north part of the image, we observe that Preto river and Mateira stream demonostrate extremely light results having values of alpha angle around 45 or higher. Moreover, this area contains very dense vegetation and it is known that very dense vegetation constitutes scatterer with high angle values, around π/4, as it can provoke volume scattering. Concluding, blue frame shows a part of the image where angle –parameter can give us a very good and clear mapping of the terrain while we have a quite rough surface. As we previously analyzed, simply rough areas get values of alpha angle below 45^o.

Moving on the entropy results of the same area (figures 74, 75 76) we can observe that the results are almost the same with alpha angle parameter ones as it has the ability to show with high values (→ 1) vegetated areas and urban environment while it gives low values to barren and not significantly rough areas. Though, it important to say that entropy parameter shows some scatterers like stronger that alpha angle (urban area on the southeast part of the scene that is given with lighter color-higher pixel values). Actually, when in entropy (and anisotropy) results do we have high values this means that in these areas we have a deterministic scattering process.

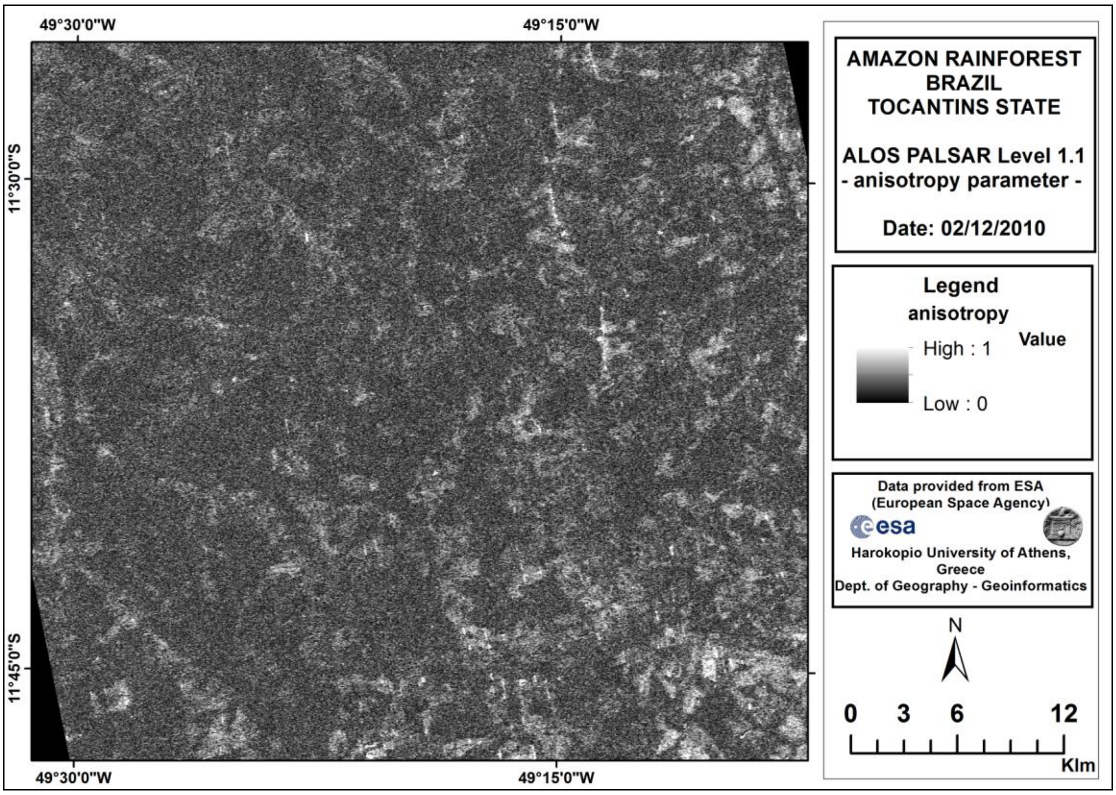

Figure 76 - anisotropy parameter derived from H-A-alpha decomposition, Tocantins state, Brazil

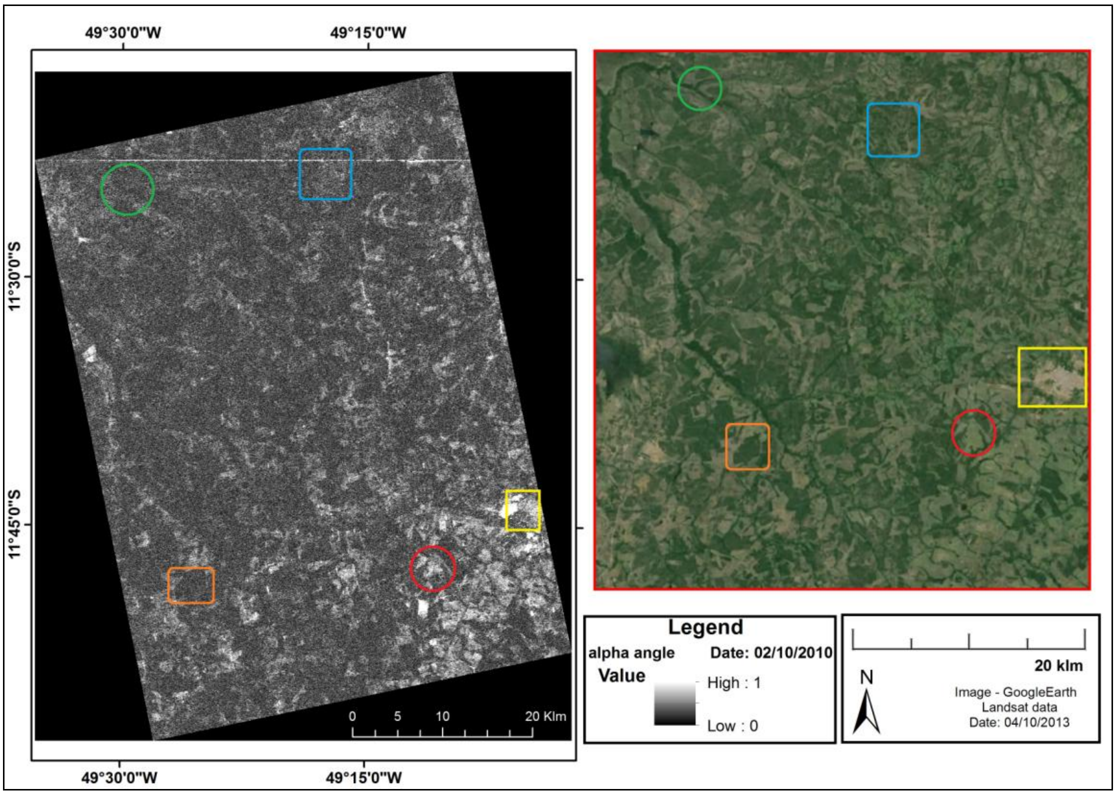

Figure 77 - Comparison of anisotropy result scene and GoogleEarth image

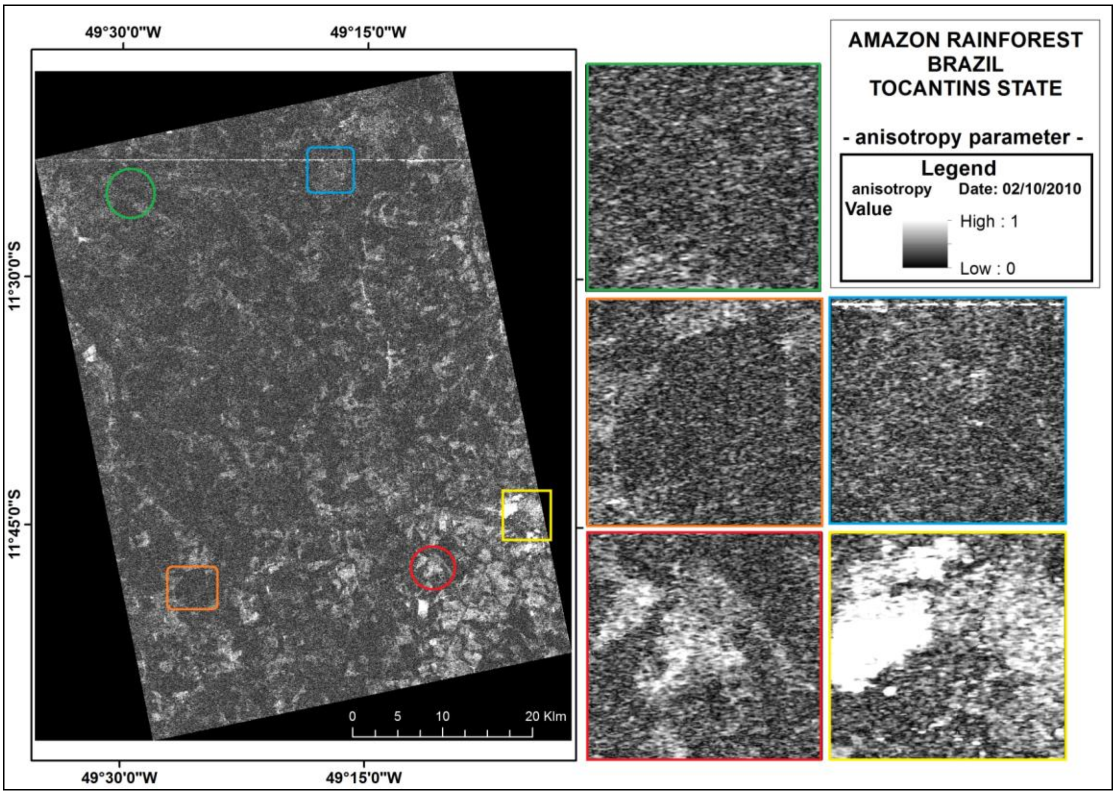

Figure 78 - Inspection of special areas with different scattering results, anisotropy parameter

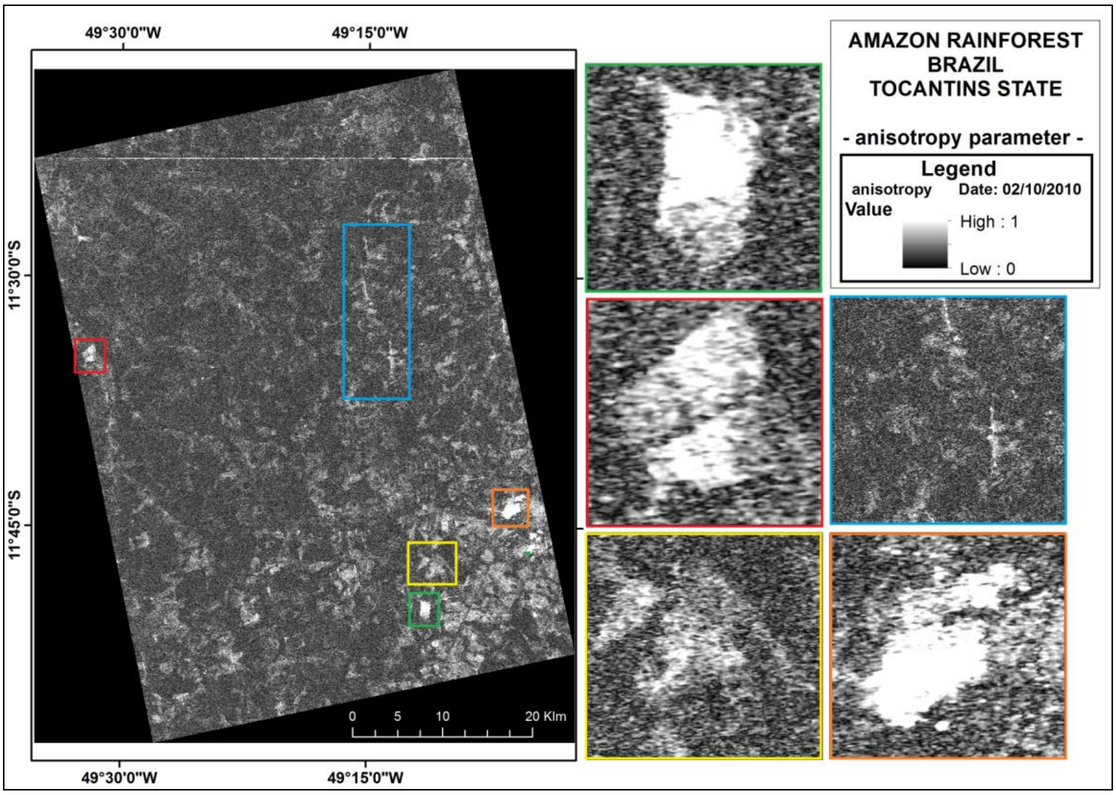

Figure 79 - Inspection of special areas with different scattering results, anisotropy parameter (version 2)

Ending up with anisotropy parameter results (figures 77, 78, 79 & 80), we see a different visualization since the majority of pixels have low values and there are regions that get extremely high values and constitute areas that we hadn't observed previously. This is very important and it is actually the main characteristic of this parameter. Hence, when we have almost the same results from alpha and entropy parameters, anisotropy comes to "light" unexplored areas as it is a measure of the number of dominant scattering mechanisms and it is feasible to achieve better discrimination between the different scattering classes. If we take a look in the figure 81 which is a false-color image, we can see how anisotropy focuses on extremely barren and low rough areas while in collaboration with alpha angles can highlight special urban targets.

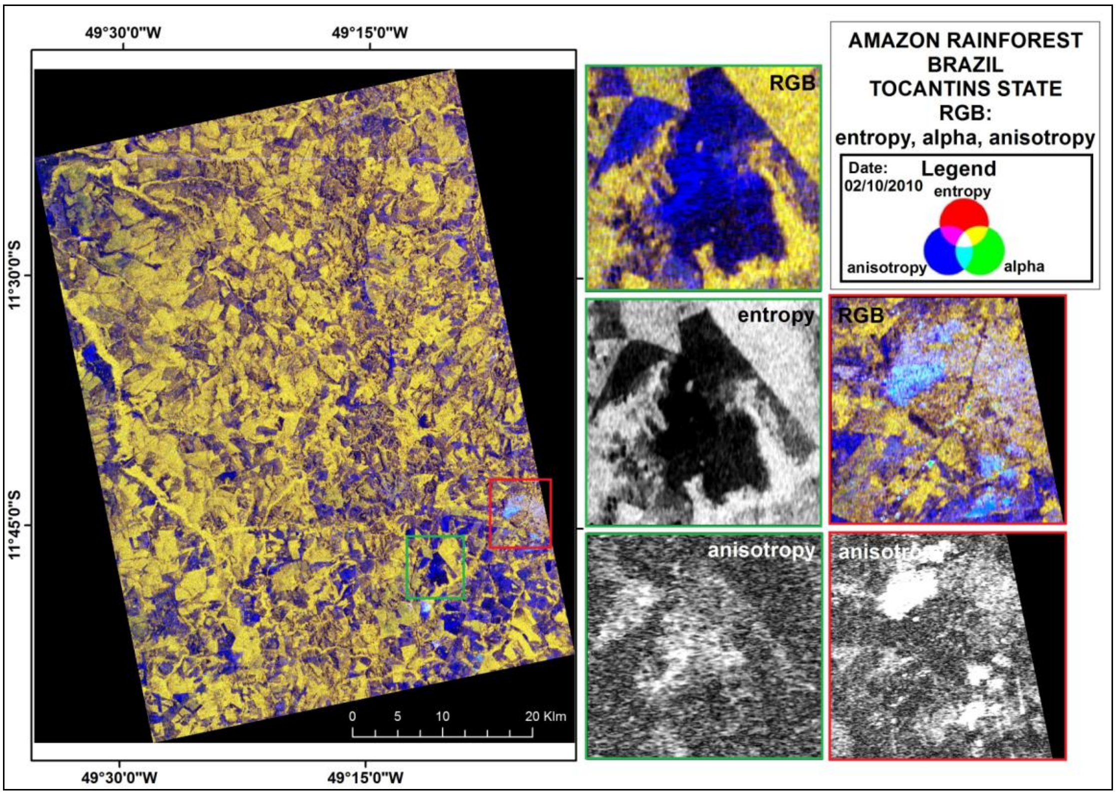

Figure 80 – RGB image of H-A-a decomposition parameters, Tocantins state, Brazil

As for the H-a plane segmentation, we can see in the plane below (figure 82) that the majority of the total information it is located in the areas 5, 6, 7 and 8. These areas represent obviously the vegetated targets plus some barren parts of Brazil land. More specifically, zones 5 and 6 represent volume scatterers, viz., vegetation features with medium or even high entropy values. As for the forest areas, there are various types of scattering mechanisms. At first, a tree can (i) backscatters from its canopy top, (ii) can give multiple and volume backscattering from its vegetated part and (iii) it can be a backscattering from the land surface. Moreover, microwave satellite systems bands play a significant role in penetration range of each one. In our case, L-band is able to penetrate trees canopy and reach the land surface. So, in this area we have a big part that consists of vegetation that gives medium and high entropy values, where the high ones mean that we have a presence of more than one dominant scattering mechanism. In zones 5 and 6 we meet dense vegetation and parts of the upper canopy that backscatter the signal (zone: 6 → cloud of anisotropic needles). Moving on the zones 7 and 8 we have cases of backscattering from rough or bragg surfaces, i.e. part of cultivated land that is temporarily in fallow or barren land. These results are strengthened by the fact that the area that we study contains many cultivated plots that spread throughout the whole scene.

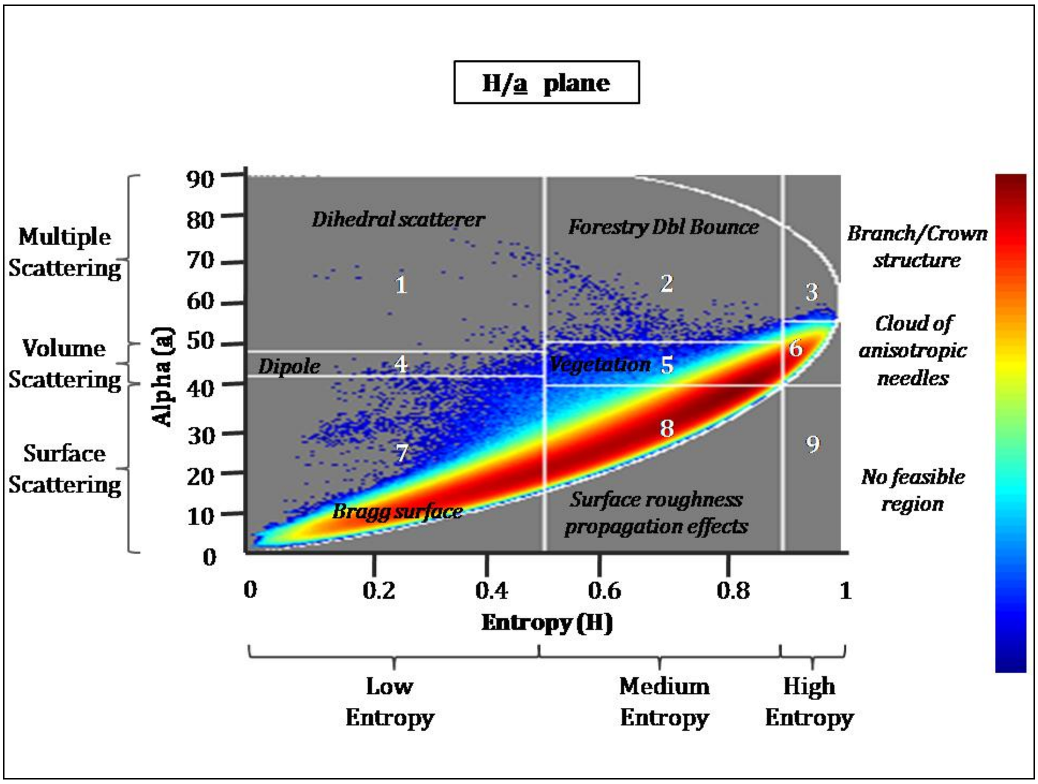

Figure 81 – H/a plane segmentation, Tocantins state, Brazil

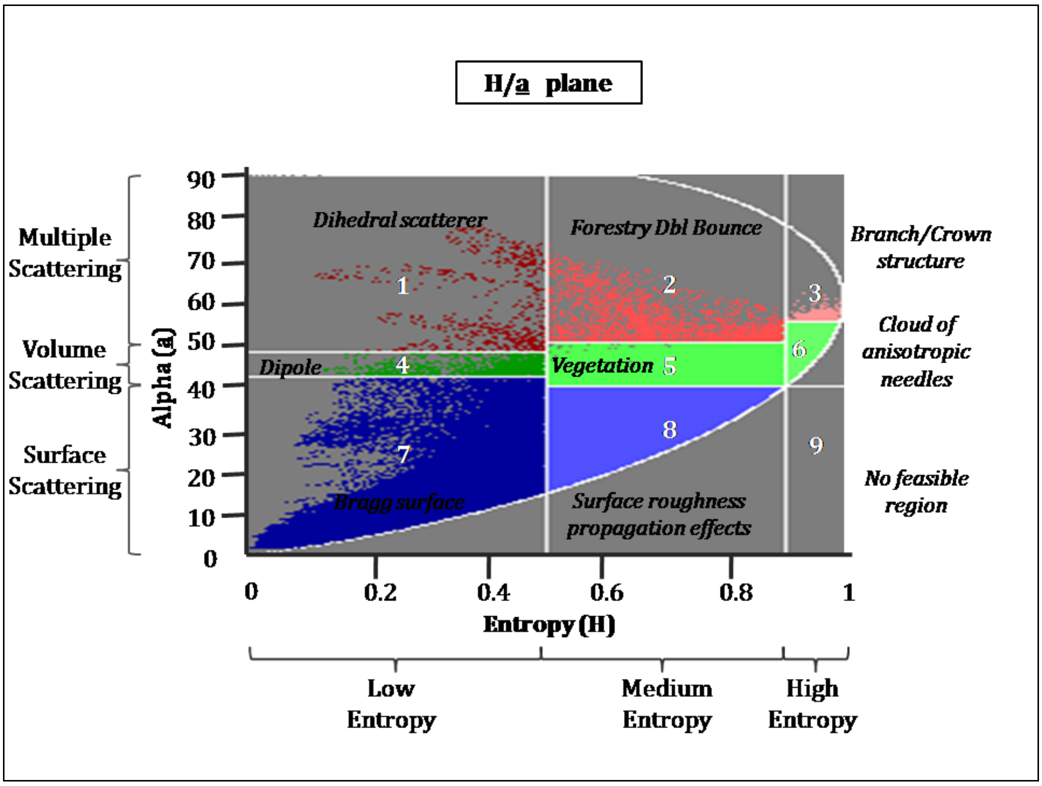

Figure 82 – H/a plane classification, Tocantins state, Brazil

Finally, we can in the next plane the classification coming from the H/a plane plus the figure that is the map with the visualization of this classification.

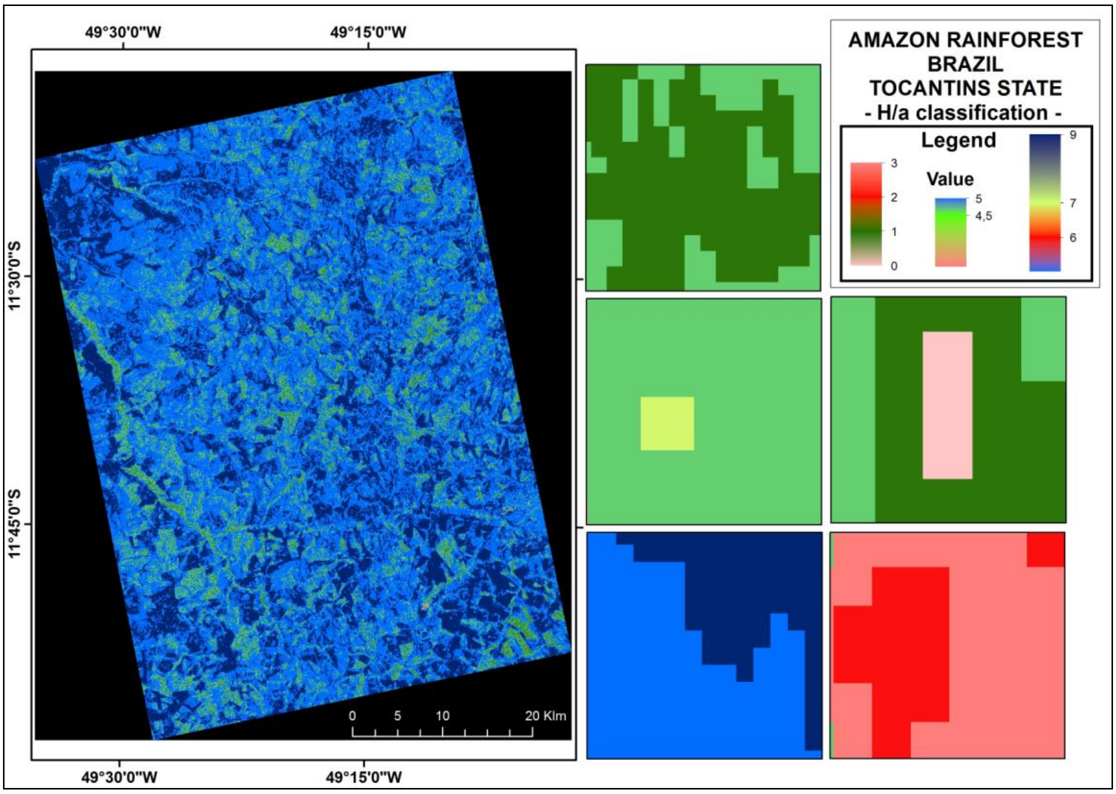

Figure 83 – H/a plane classification (different plane classes), Tocantins state, Brazil

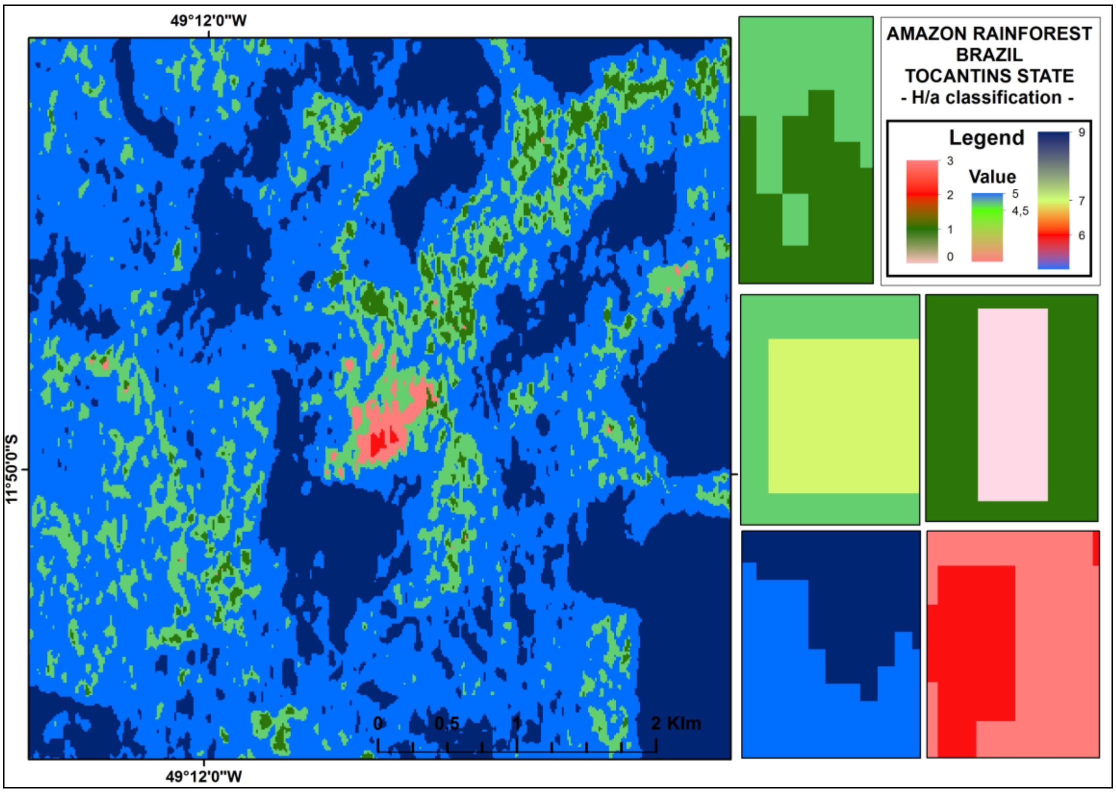

Figure 84 - H/a plane classification (different plane classes), Tocantins state, Brazil

In figures 84 and 85 we can see the visualization of H/a plane classification. The light pink areas represent crown structure that comes from the top of vegetation backscattering that is the canopy backscattering, the light green areas represent the vegetated parts of the study area and dark blue regions are land parts where we have bragg surfaces where the a percentage of the signal can penetrate the land surface and then backscatters.

Moreover, we calculated various H-A combinations that can be used for more detailed analysis of the area based on these parameters extraction. Below we can see the results of these combinations (figures 86-89).

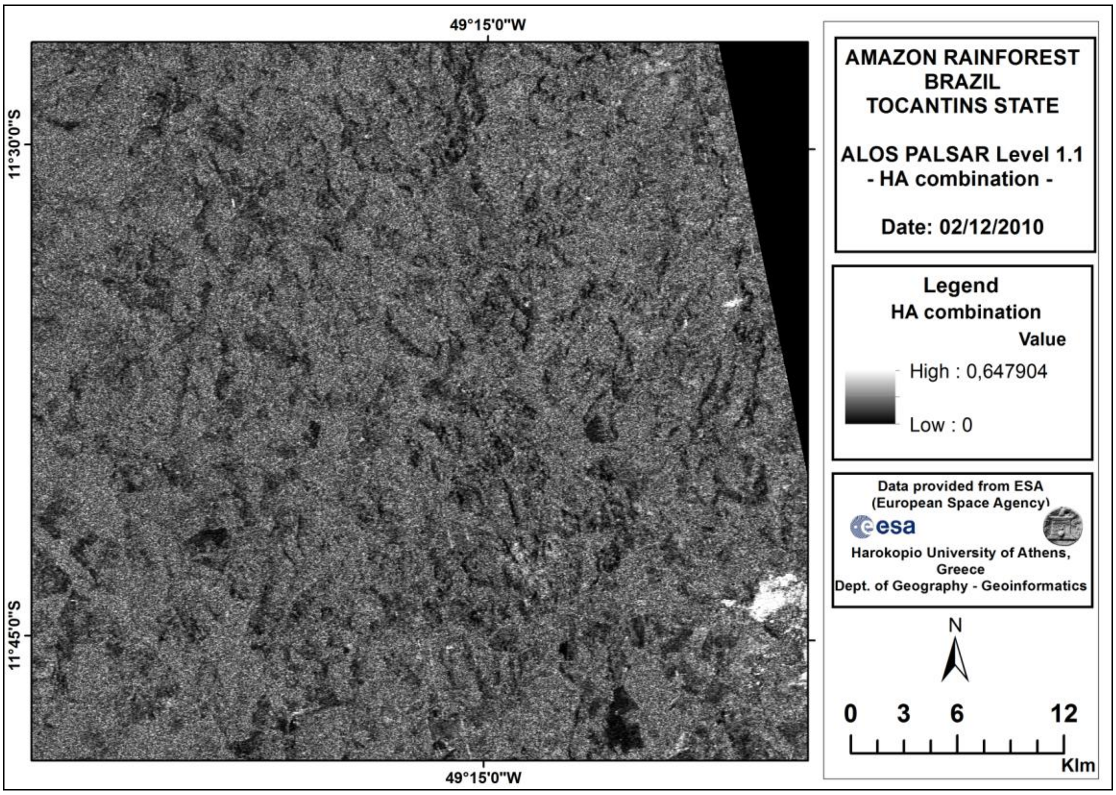

Figure 85 – HA combination of entropy and anisotropy parameters, Tocantins state, Brazil

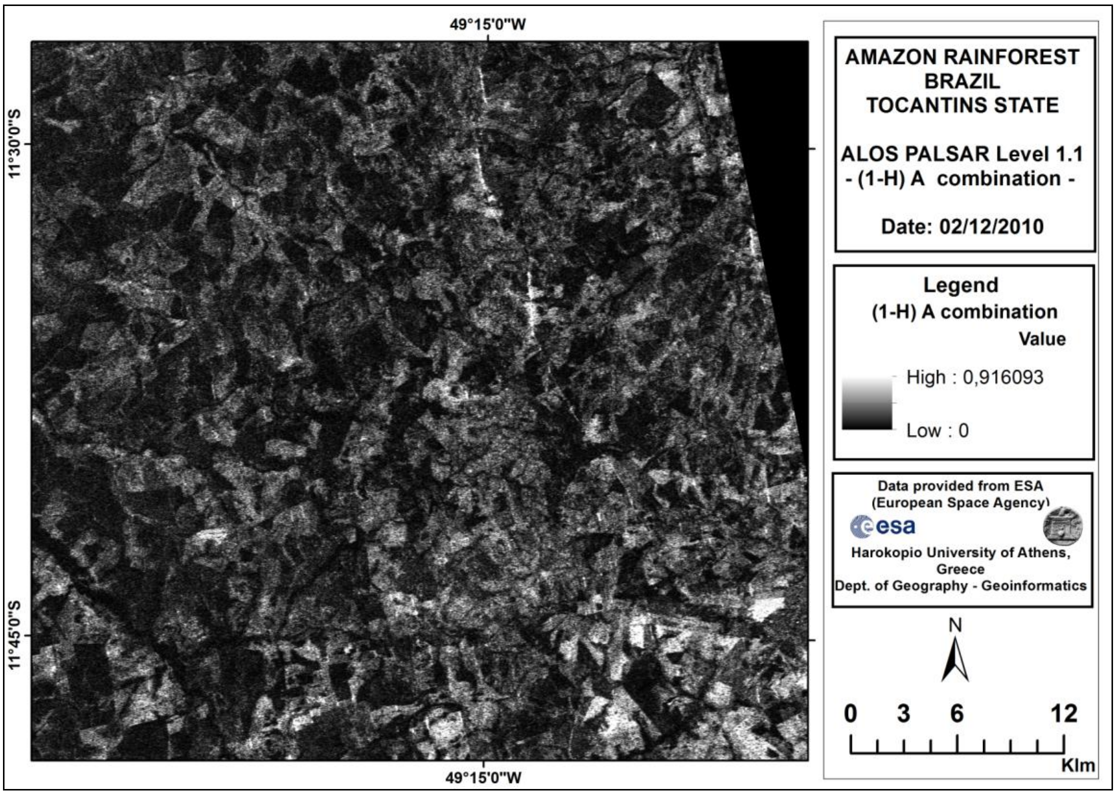

Figure 86 – (1-H)*A combination of entropy and anisotropy parameters, Tocantins state, Brazil

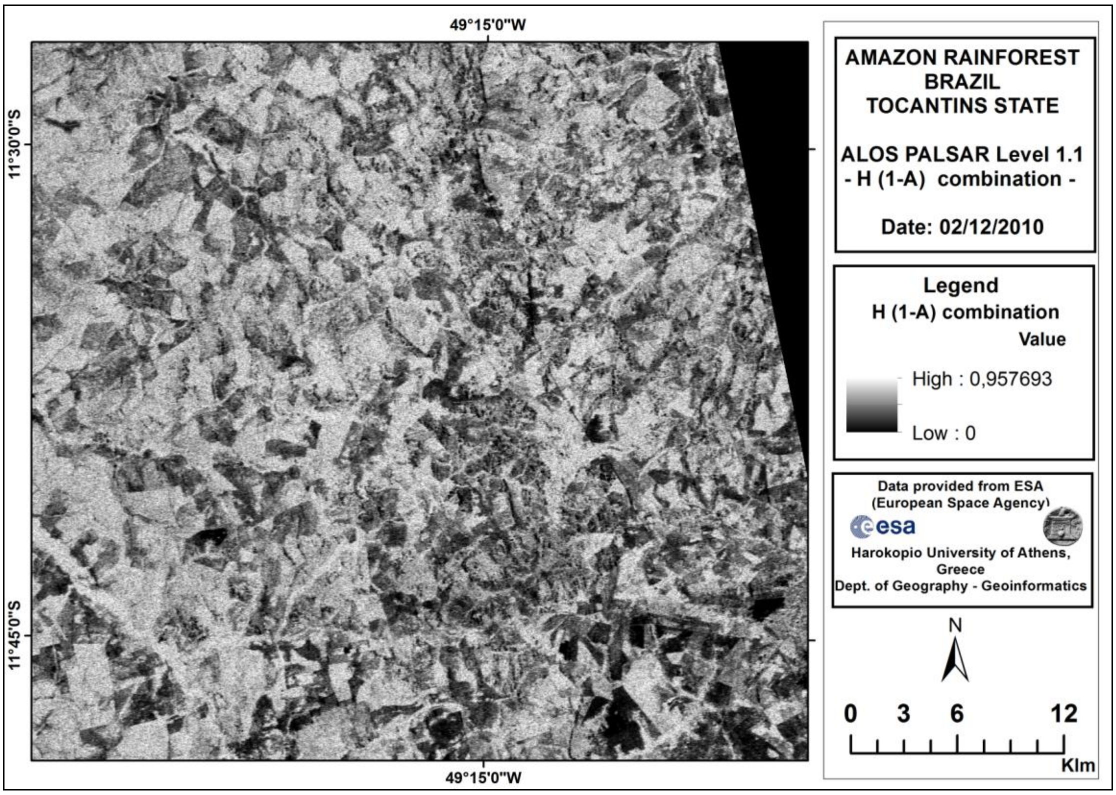

Figure 87 – H*(1-A) combination of entropy and anisotropy parameters, Tocantins state, Brazil

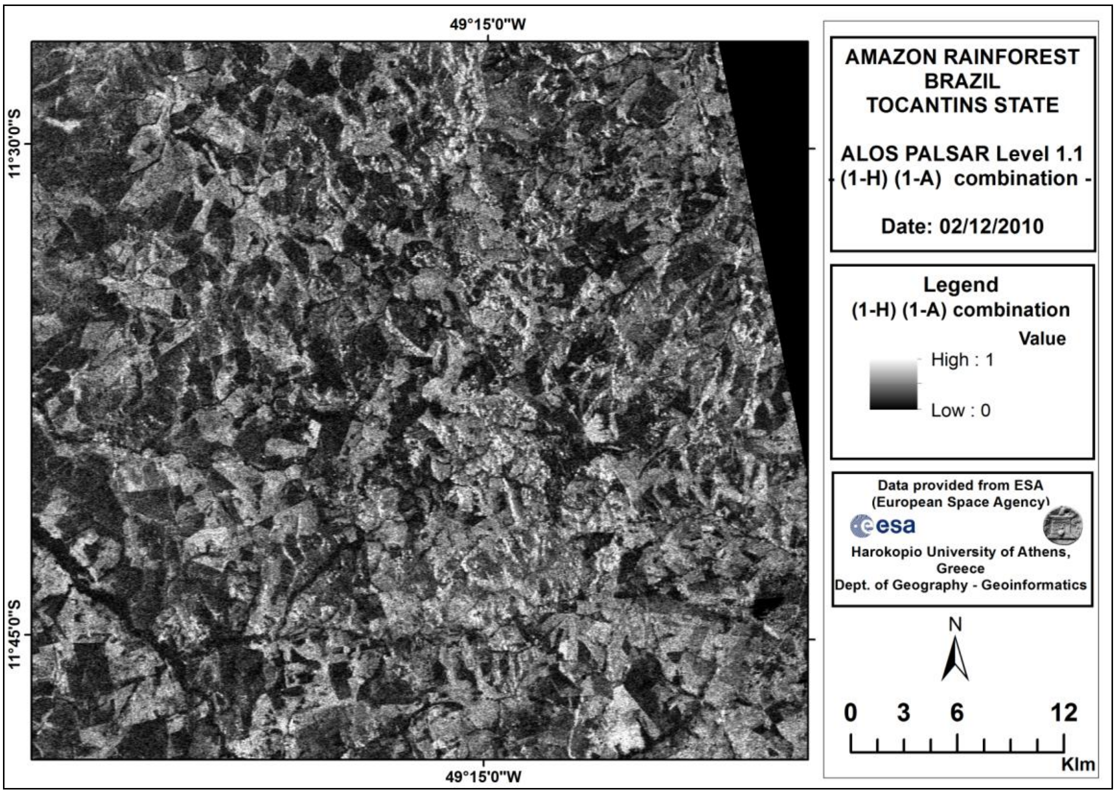

Figure 88 – (1-H)*(1-A) combination of entropy and anisotropy parameters, Tocantins state, Brazil

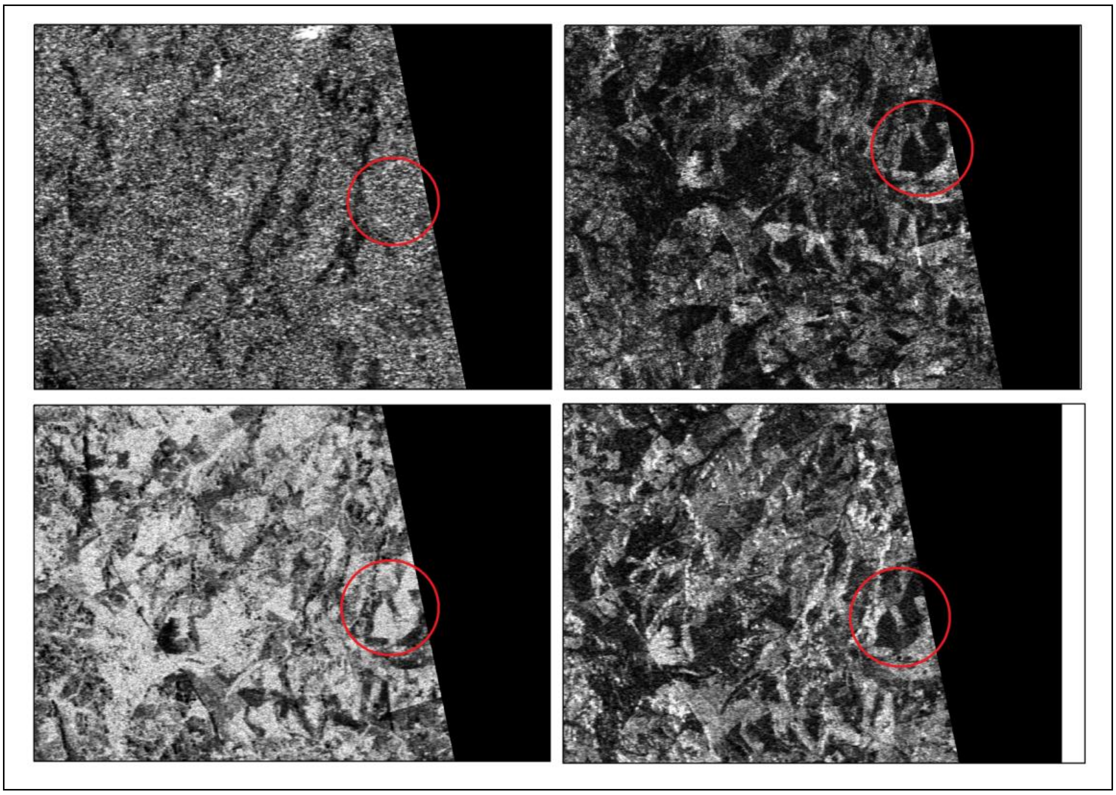

Figure 89 – (from left, clockwise) HA, (1-H)*A, H*(1-A), (1-H)*(1-A) combinations of H/A decomposition parameters, zoom areas

From these results we reach the conclusion that HA combination creates an generalized image where we can't distinguish many features while the rest 3 combinations give a more classified image that some of them have common coding with some H/A/a Decomposition parameters. Though, HA results are in common with anisotropy results. On the other hand, H*(1-A) combination give similar results with entropy ones while H*(1-A), (1-H)*(1-A) combinations are similar to alpha and entropy outcomes respectively. On figure 90 we can see that the feature in the red circle are visualized differently according to each combination results. In 1-H)*A and H*(1-A) combinations is given with bright colors while on the (1-H)*(1-A) combination is given with dark colors. Moreover, on the first combination is impossible to distinguish this feature nevertheless some features that are like streams can be easily located in dark color lines.

19.3.2 Freeman-Durden Decomposition

As we previously analyzed, Freeman-Durden decomposition is a statistical model based decomposition technique that has better stability in convergence and preserves the dominant scattering mechanism of each class. According this decomposition, the image pixels are divided into three categories: surface, volume and even bounce scattering. Pixels in each category are classified independently of pixels in the other categories in order to preserve the purity of scattering characteristics for each class. This unsupervised algorithm was applied in our Alos Palsar data of Amazon area, as a way to define the forested area and to evaluate the effectiveness of vegetation characterization based on polarimetric data alone (Vyjayanthi N. 2012).

Freeman-Durden decomposition models the covariance matrix as the contribution of three scattering mechanisms (see figures 90-93)

- Volume scattering where a canopy scatterer is modeled as a set of randomly oriented dipoles.
- Double-bounce scattering modeled by a dihedral corner reflector.
- Surface or single-bounce scattering modeled by a first-order surface scatterer (Vyjayanthi N. 2012).

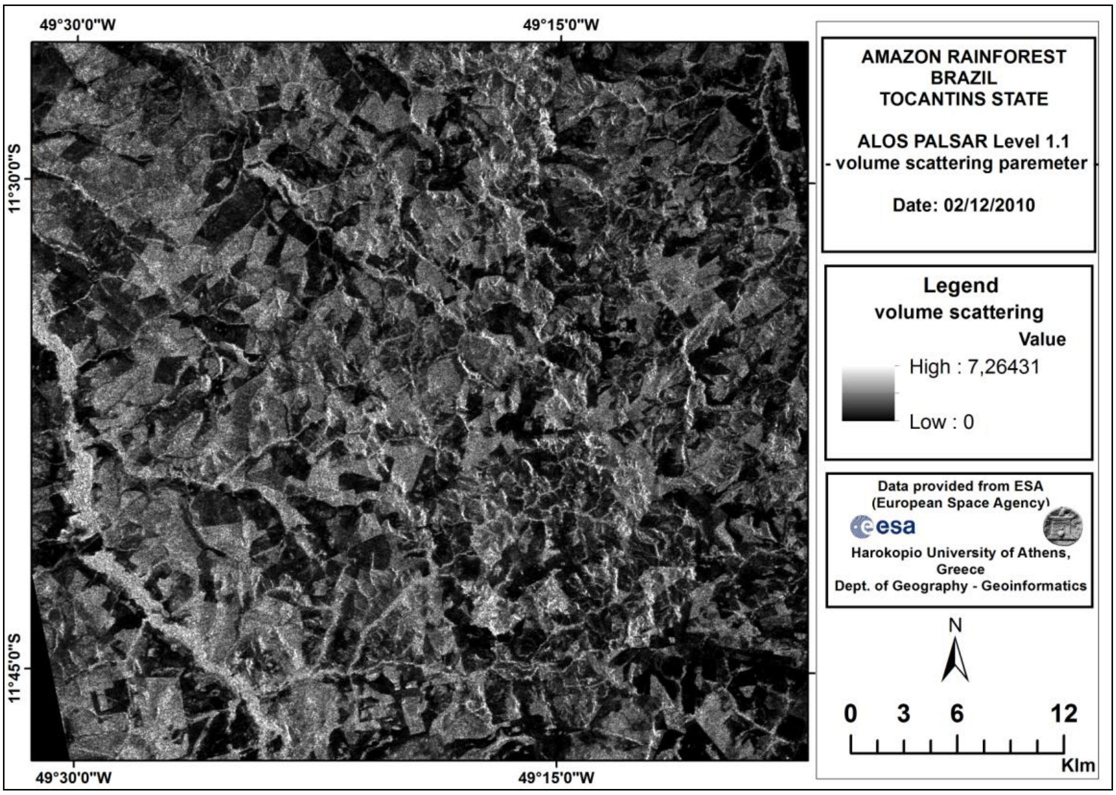

Figure 90 – Volume Scattering parameter *(Pv)* derived from Freeman-Durden decomposition, Tocantins state, Brazil

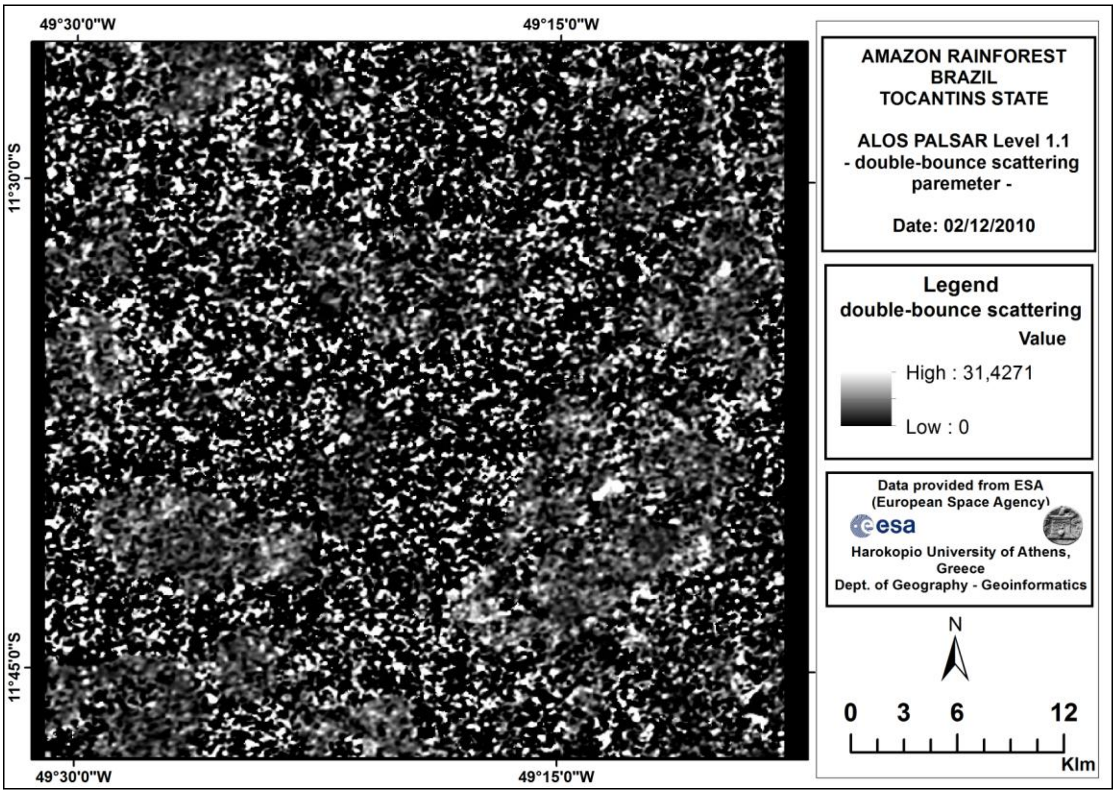

Figure 91 – Double-bounce parameter *(Pd)* derived from Freeman-Durden decomposition, Tocantins state, Brazil

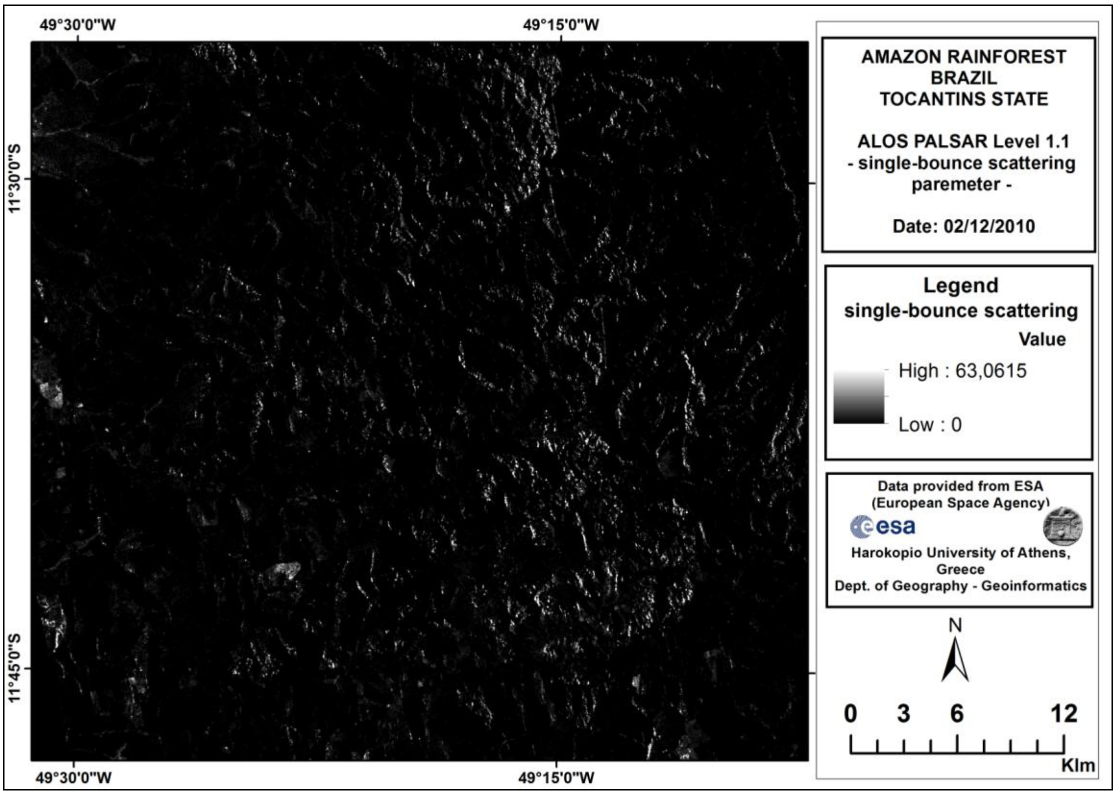

Figure 92 – Single bounce parameter *(Ps)*derived from Freeman-Durden decomposition, Tocantins state, Brazil

The volume scattering from a forest canopy is modeled as an ensemble of randomly oriented thin dipoles. The volume scattering cannot be characterized by a single scattering matrix of a pure target. As the study area contains various forest parts, volume scattering was dominant in the study area. Agricultural area has shown surface scattering. This can be interpreted as indication that the longer wavelengths (L-band in this case) can penetrate the relatively short vegetation in agricultural area and the backscatter is mostly from the underlying ground (Vyjayanthi N. 2012).

The Freeman-Durden decomposed image provided a good separation of forest from agricultural fields but classification within the forest is poor. Barren areas and the individual trees were easily discriminated.

The second component of the Freeman decomposition corresponds to double-bounce scattering. The electric poles show the double bounce scattering and are seen as bright red color (figure 94). Though, in this case we didn't have this type of scatters so we don't see a lot of areas behaving like this. On the other hand we have some areas with individual trees in the barren regions also showing the double bounce scattering and could be easily discriminated (Vyjayanthi N. 2012).

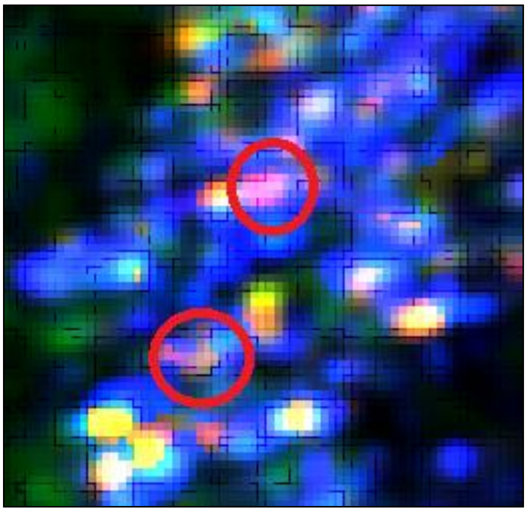

Figure 93 - Freeman-Durden RGB image (Double-Volume-Single bounce scattering)

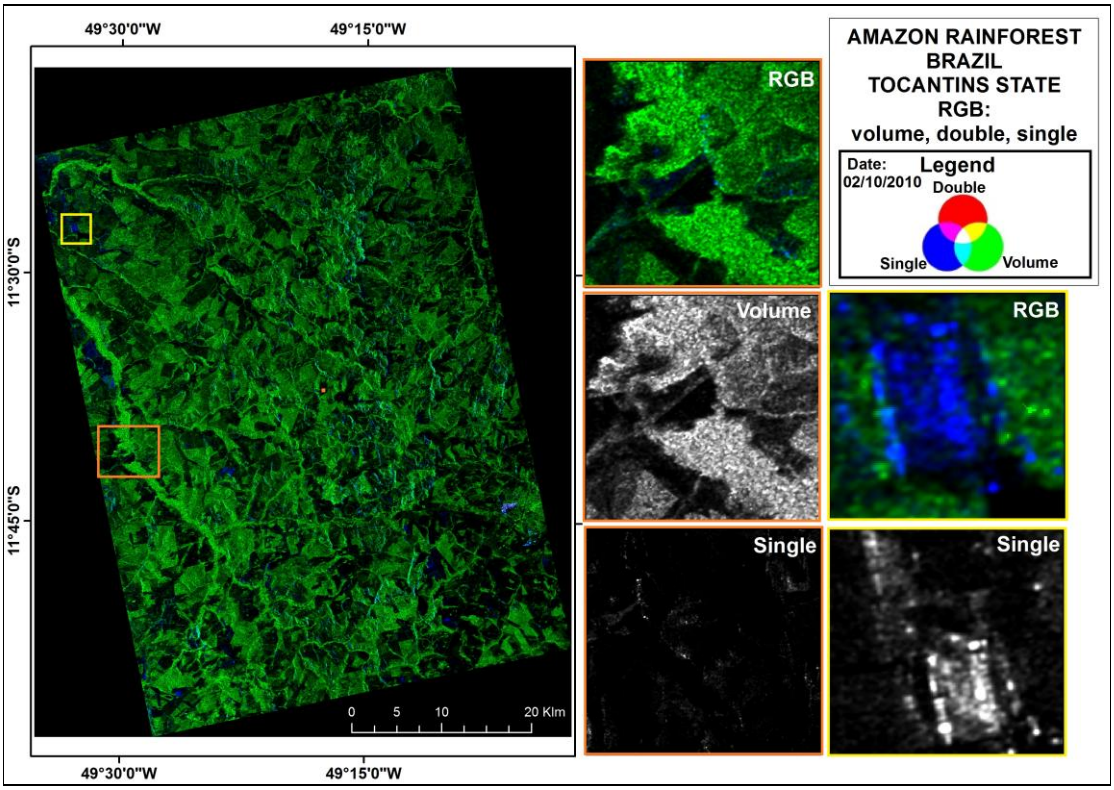

Figure 94 - RGB image of Freeman-Durden decomposition parameters, Tocantins state, Brazil

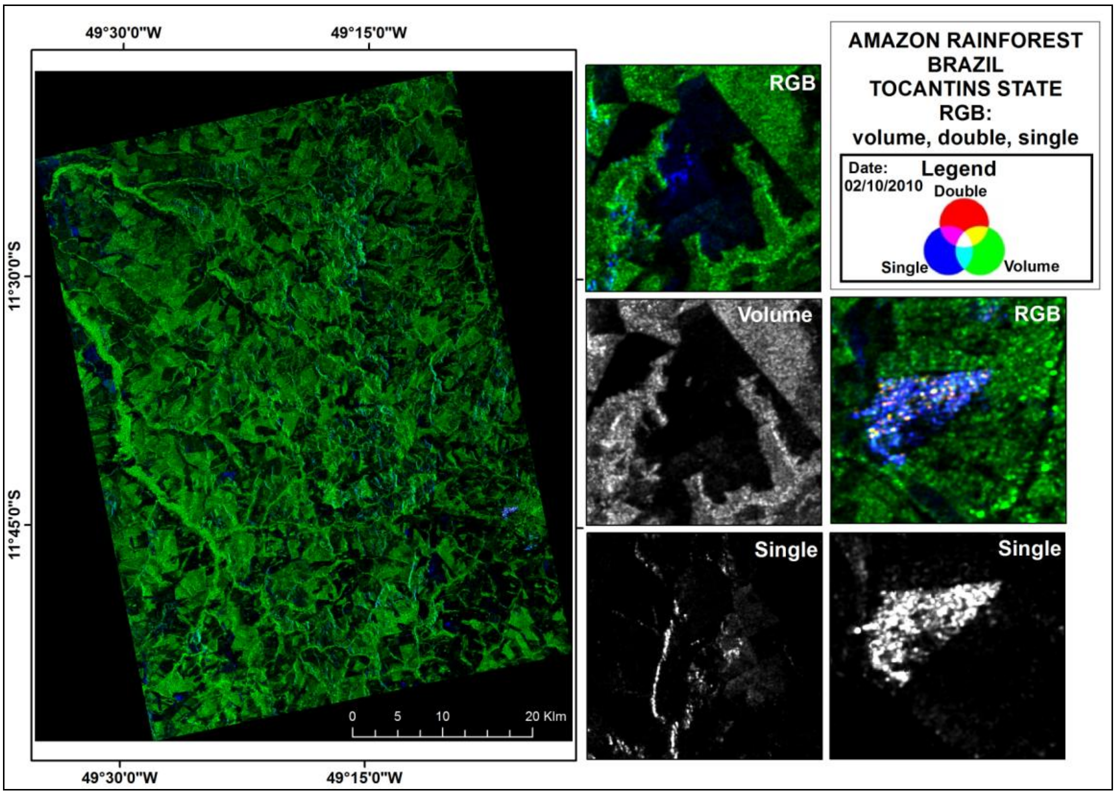

Figure 95 - RGB image of Freeman-Durden decomposition parameters, Tocantins state, Brazil (areas examined in H/A/a Decomposition)

Consequently, the scattered power *Pv*, *Pd* and *Ps* are used to generate a RGB image with distinguishable themes as separate classes using polarimetric information of a single image, which describe different scattering mechanisms (see figures 95-96). There, is quite obvious that Volume-scattering parameter and single scattering is highly recommended rough and urban areas since they can detect this type scatterer targets while single-scaterring parameter focuses on villages and towns (white color).

20. CONCLUSION

We used 2 types of satellite SAR data; ENVISAT and PALSAR ones. We studied a vast area of Brazilian Amazon territory that included few states like Para and Tocantins where have been reported deforestation cases in the past. ENVISAT images cover Tocantins state land while PALSAR ones refer to 4 different Brazilian states (Pará, Amapá, Tocantins and Goiás).

In this Thesis we decided to show the results from one of these states, Tocantins, since is the one that contains ENVISAT and PALSAR data simultaneously while it is about an area that contains al lot of crops, cultivated regions, virgin forest and urban land where we could examine the polarimetric characteristics of our data over the different feature scattering properties.

The ENVISAT data are of VV polarization and locate over the same area while cover a time line from 2004 till 2006. The PALSAR dataset is of quad-polarization covering a vast land expanse extended from the northern part of Brazil, Para state, including part of Amazon river, till the Goiás state.

As for the Envisat images we applied .various filters in order to reduce speckle phenomenon which is very common in SAR images and it usually confused with noise but it is not. From all the filters and kernel sizes that were applied we decided to show Lee and Frost of 5x5 and 7x7 kernel comparing the results. We separated the data into 2 groups of scenes for a multi-temporal and a multi-seasonal analysis too. There are few change detections in the whole area for the multitemporal and the seasonal analysis too. The point is that these changes may are changes that have to do with the farm land exploitation and high vegetation activity. So, we may conclude in the fact that the changes that have been detected are mostly seasonal changes. On the other hand, about the filters, we ended in the conclusion that both Lee and Frost filters give equal results while Kernel 5x5 reduces less the speckle filtering than the Kernel 7x7 that give better outcomes but in some cases provokes generalizations and information reduction.

As for the Alos images, in this thesis we analyzed mostly the Tocantins state results which showed interesting extracts. The area of Tocantins state, showed that contains cultivated areas, barren land and some villages and small towns too. We applied various Decomposition techniques but we decided to show the ones that are the most common applied plus techniques that are widely used for vegetation study and classification (Freeman-Durden classification). H/A/a Decomposition and classification provide important information about the various feature scattering mechanisms while the H/a plane provide a very good classification of the area characteristics. In this case where our scene contained mixed features (urban areas-villages and towns, cultivated land, forest and barren extents) was very interest to see how these different land parts behave with microwave radiation. Moreover, Freeman-Durden Decomposition has been applied in vegetated areas from many scientists and has been proved really able to distinguish vegetated features. In our cases we noted that described in detail urban areas while we observed the double-bounce scattering absence. It existed in only few areas inside urban regions. On the contrary, the volume scattering that comes from vegetation was dominant in the scene.

21. DISCUSSION

Concluding the basic part of ENVISAT and ALOS images using SAR Polarimetry methodology, I think that as far as the ENVISAT data is concerned, we could use, for a next step analysis, Alternating Polarization (AP) Mode provides for a more detailed study over polarimetry. Moreover, for the ALOS data, we could create timeseries with the images that cover the same land areas showing the vegetation changes over the years. Moreover, as far as it concerns the ALOS data we can apply supervised classification using special ROI areas for getting better results.

22. AKNOWLEDGEMENTS

I would like to thank very much Professor *Issaak Parcharidis* of Harokopio University of Athens, Department of Geography who entrusted me this topic. Furthermore, I specially thank Reasearcher *Sykioti Olga* from National Observatory of Athens who was the one that had the initial idea me to work on this science topic of SAR Polarimetry. Moreover, I thank *Eohelp*, the Technical Supporting Team of ESA (Earth Space Agency) who helped me so much during the whole data processing and responded immediately on my queries. Finally, I would like to thank particularly Prof. *Pottier Eric* at the University of Rennes 1 – France, Laboratoire: Institut d' Electronique et de Télécommunications who accepted to help me preparing my Thesis with object SAR Polarimetry and supported me very much in many parts that I faced problems and obstacles.

BIBLIOGRAPHY – REFERENCES

Butler, Rhett A. (2006). Amazon rainforest.Mongabay.com / A Place Out of Time: Tropical Rainforests and the Perils They Face. 9 January 2006.

C. N. Koyama and K. Schneider. A novel approach to estimate soil moisture under vegetation using partial polarimetric Alos Palsar Data. *International Archives of the Photogrammetry, Remote Sensing and Spatial Information Science, Volume XXXVIII, Part 8, Kyoto Japan 2010*

Chapter 6 in Jensen, J.R. 1996. Introductory Digital Image Processing: A Remote Sensing Perspective. *Second Edition, Upper Saddle River, NJ, Prentice Hall. 318pp.* (http://rslab.uc.edu/liu/courses/g361/note4.pdf), last site visit: 14/9/15

D.Haldar, M. Chakraborty, K.R. Manjunath and J.S. Parihar. Role of Polarimetric SAR data for discrimination/biophysical parameters of crops based on canopy architecture. *The International Archives of the Photogrammetry, Remote Sensing and Spatial Information Sciences, Volume XL-8, 2014 ISPRS Technical Commission VIII Symposium, 09 – 12 December 2014, Hyderabad, India*

Florence Tupin, Isabelle Bloch, and Henri Maˆıtre (1999). A First Step Toward Automatic Interpretation of SAR Images Using Evidential Fusion of Several Structure Detectors. *IEEE TRANSACTIONS ON GEOSCIENCE AND REMOTE SENSING, VOL. 37, NO. 3, MAY 1999*

F. Qiu, J. Berglund, J. R. Jensen, P. Thakkar and D. Ren (2004). Speckle Noise Reduction in SAR Imagery Using a Local Adaptive Median Filter. *GIScience and Remote Sensing, 2004, 41, No. 3, pp. 244-266.*

Gallant AL, Kaya SG, White L, Brisco B, Roth MF, Sadinski W, Rover J. Detecting Emergence, Growth, and Senescence of Wetland Vegetation with Polarimetric Synthetic Aperture Radar (SAR) Data. ***Water***. 2014; 6(3):694-722.

G. Singh, Y. Yamaguchi, S-E. Park and Ram Avatar. Evaluation of modified four-component scattering power decomposition method over highly. http://dspace.lib.niigata-u.ac.jp/dspace/bitstream/10191/30087/1/GI_26, last site visit: 17/9/15

Giorgio Franceschetti, Raffaella Guida, Antonio Iodice, Daniele Riccio, Giuseppe Ruello and Uwe Stilla. Simulation Tools for Interpretation of High Resolution SAR Images of Urban Areas. http://epubs.surrey.ac.uk/726883/2/Paper_guida_preprint.pdf, last site visit: 23/9/15

H. Joerg, M. Pardini, I. Hajnsek and Konstantinos Papathanasiou. Application of polarimetric sar tomography on agricultural vegetation for scattering characterization. *Application of Polarimetric SAR Tomography on Agricultural Vegetation for Scattering Characterisation. Polarimetric and Interferometric SAR Workshop (PI-SAR), 2015-0126 - 2015-01-30, Frascati, Italy.*

H. Cui. A deconvolution method to remove distortion caused by antenna radiation pattern from measurement. *IEEE. Antenna Technology (iWAT), 210 International Workshop. 1-3 March 2010. E-ISBN: 978-1-4244-4885-2.*

H.Skriver, W.Dierking, P. Gudmandsen, T. Le Toan, A. Moreira, K. Papathanassiou, and S. Quegan. (2003). Applications of synthetic apperture radar polarimetry, *Proceedings of the Workshop on POLinSAR - Applications of SAR Polarimetry and Polarimetric Interferometry (ESA SP-529).* 14-16 January 2003, Frascati, Italy. Editor: H. Lacoste. Published on CDROM., id.2.1, Bibliographic Code: 2003ESASP.529E...2S

Hong S-H, Kim H-O, Wdowinski S, Feliciano E. Evaluation of Polarimetric SAR Decomposition for Classifying Wetland Vegetation Types. ***Remote Sensing***. 2015; 7(7):8563-8585.

IEEE Transactions on Geoscience and Remote Sensing, VOL. 52, NO. 6, June 2014

Jong_Sen Lee, Jen_Hung Wen, Ainsworth, T. L., Kun-Shan Chen, Chen, A.J. Improved Sigma Filter for Speckle Filtering of SAR Imagery. *Geoscience and Remote Sensing, Volume:47 Issue:1*

Jong-Sen Lee and eric Pottier (2009). Polarimetric Radar Imaging: From Basics to Applications. *CRC Press. Taylor & Francis Group.*

J. David Ballester-Berman, Fernando Vicente-Guijalba, and Juan M. Lopez-Sanchez. Polarimetric sar model for soil moisture estimation over vineyards at c-band. *Progress In Electromagnetics Research, Vol. 142, 639–665, 201.*

J. Assuncao, C. Gandour, R. Rocha (2013). DETERing Deforestation in the Brazilian Amazon: Environmental Monitoring and Law Enforcement. *Climate Policy Initiative.Nucleo De Avaliacao De Politicas Climaticas PUC-Rio. CPI Report*.(http://climatepolicyinitiative.org/wp-content/uploads/2013/05/DETERring-Deforestation-in-the-Brazilian-Amazon-Environmental-Monitoring-and-Law-Enforcement-Technical-Paper.pdf), last site visit: 03/02/2016

K.Arai. Polarimetric SAR Image Classification with High Frequency Component Derived from Wavelet Multi Resolution Analysis: MRA Maximum Curvature of Trajectory of Back Scattering Cross Section Converted from Eigen Space of Ellipticity and Orientation Angle Space of Polarization Signature. *(IJACSA) International Journal of Advanced Computer Science and Applications, Vol. 2, No.9, 2011*

K. Shah, V.R. Laskshmi Gorty, Ajay Phirke (Eds.) (2011). Technology systems and management. *First International Conference, ICTSM 2011, Mumbai, India, February 2011, Selected Papers. Editions: Springer.*

Lee, Jong-Sen (1980). Digital Image Enhancement and Noise Filtering by Use of Local Statistics,”*IEEE Transactions on Pattern Analysis and Machine Intelligence, Vol PAMI-2, No.2, March 1980, pp. 165-168.*

L. Gagnon and A. Jouan. Speckle Filtering of SAR Images - A Comparative Study Between Complex-Wavelet-Based and Standard Filters.

M. Caprioli, B. Figorito, E. Tarantino. Radiometric Normalization of Landsat ETM+ Data for Multitemporal Analysis. *The International Archives of the Photogrammetry, Remote Sensing and Spatial Information Sciences, Vol. 34, Part XXX*

Martin Kong, Brigitte Leblon, Renaud Mathieu, Claus -Peter Gross, Joseph Buckley , Laven Naidoo and Laura Bourgeau –Chavez (2014). Use of radarsat -2 polarimetric sar images for fuel moisture mapping in the kruger national park, south Africa. *IGARSS 2014, 978-1-4799-5775-0/14/$31.00 ©2014 Crown*

Mascarenhas, N. D. A. (1997). An Overview of Speckle Noise Filtering in SAR Images. *Image Processing Techniques, First Latino-American Seminar on Radar Remote Sensing: Proceedings of a conference held 2-4 December, 1996, Buenos Aires, Argentina, edited by Shaun Quegan and Joao R. Moreira (1997)., p.7. Bibliographic Code: 1997ESASP.407...71M*

N. Lahlou, L. Ferro-Famil and S. Allain Bailhache. Retrieving soil moisture below a vegetation layer using polarimetric tomographic sar data. IGARSS 2014, Quebec, Canada

N. Vyjayanthi. 2012. Synthetic Aperture radar data analysis for vegetation classification and biomass estimation of tropical forest area. Faculty of Spatial Information Technology. (http://shodhganga.inflibnet.ac.in/handle/10603/3440), last site visit: 04/02/2016

Seyed Hamed Alemohammad. Retrieving Vegetation Parameters and Soil Reflection Coefficients with P-band SAR Polarimetry, *IEEE IGARSS, Italy 2015, Code number: 7480*

S. Zwieback and I. Hanjnsek. Analysis of invariances in sar polarimetry. IEEE GOLD REMOTE SENSING, 4 - 5 June 2012 Roma, Italy, ISBN13: 978-88-7431-668-7, ©2013 Giannini Editore

S-H. Hong, and S. Wswonski. Double-Bounce Component in Cross-Polarimetric SAR From a New Scattering Target Decomposition.

S. Zhang, S. Wang and B. Chen (2014). Modified Hybrid Freeman/Eigenvalue Decomposition for Polarimetric SAR Data. *Journal of Sensors Article ID 168720*

Takashi Shibayama, Yoshio Yamaguchi, and Hiroyoshi Yamada. (2015). Polarimetric Scattering Properties of Landslides in Forested Areas and the Dependence on the Local Incidence Angle. Remote Sens. 2015, 7(11), 15424-15442; doi:10.3390/rs71115424

Thomas Jagdhuber, Julia Stockamp, Irena Hajnsek and Ralf Ludwig. (2014). Identification of Soil Freezing and Thawing States Using SAR Polarimetry at C-Band. Remote Sensing 2014, 6(3), 2008-2023; doi:10.3390/rs6032008

T. Jagdhuber, 2012, Soil parameter retrieval under vegetation cover using SAR polarimetry, Institutional Repository of the University of Potsdam, URN urn:nbn:de:kobv:517-opus-60519, http://nbn-resolving.de/urn:nbn:de:kobv:517-opus-60519, https://publishup.uni-potsdam.de/opus4-ubp/frontdoor/index/index/docId/5894 last site visit: 5/10/15

V. Turkar and Y.S. Rao (2011). Applying Coherent and Incoherent Target Decomposition Techniques to Polarimetric SAR Data. *International Conference on Technology Systems and Management (ICTSM) 2011 Proceedings published by International Journal of Computer Applications® (IJCA)*

V. Akbari , Y. Larsen, A. P. Doulgeris, and T. Eltoft. The impact of terrain correction of polarimetric sar data on glacier change detection. *IGARSS.*

Wen Yang, Tong-yuan Zou, Hong Sun, Xin Xu. Improved Unsupervised Classification Based on Freeman-Durden Polarimetric Decomposition.

W-M. Boerner. Basics of SAR Polarimetry I. UIC_ECE Communications, Sensing & Navigation Laboratory. http://www.dtic.mil/dtic/tr/fulltext/u2/a471015.pdf , last visit: 10/09/15

Y. Huang and J.V. van Genderen (1996). Evaluation of several Speckle Filtering Techniques for ERS-1&2 Imagery. *International Archives of Photogrammetry and Remote Sensing. Vol. XXXI, Part B2, Vienna 1996*

Zhengxiao Li a and James Bethel (2008). Image coregistration in sar interferometry. *The International Archives of the Photogrammetry, Remote Sensing and Spatial Information Sciences. Vol. XXXVII. Part B1. Beijing 2008*

Zhenghao Shi and Ko B. Fung, “A Comparison of Digital Speckle Filters,” Proceedings of IGARSS 94, August 8-12, 1994, pp. 2129-2133. (http://www.exelisvis.com/docs/AdaptiveFilters.html), last site visit: 10/9/15.

Zili Shan, Hong Zhang , Chao Wang, Fan Wu, Bo Zhang, Yixian Tang. A modified model based sar target decomposition method for polarimetric data. *Proc. ‘Fringe 2011 Workshop’, Frascati, Italy, 19–23 September 2011 (ESA SP-697, January 2012)*

Internet sources

Alaska Satellite Facility (ASF). https://www.asf.alaska.edu/sar-data/palsar/terrain-corrected-rtc/, last site visit: 14/9/15

Alaska Satellite Facility (ASF). https://www.asf.alaska.edu/data-tools/mapready/, last site visit: 24/9/2015

Alaska Satellite Facility (ASF) https://www.asf.alaska.edu/data-tools/mapready/, last site visit: 24/9/15

C. López-Martínez, L. Ferro-Famil, E. Pottier. January 2005. TUTORIAL ON SAR POLARIMETRY. Polarimetry Tutorial. PolSARPro. ESA

CRISP. 2001. http://www.crisp.nus.edu.sg/~research/tutorial/sar_int.htm, last site visit: 20/9/15

E. Pottier, L. Ferro-Famil. January 2004. POLARIMETRIC SPECKLE FILTERING. IETR - Institut d'Électronique et de Télécommunications de Rennes, Saphir Software GmbH. (https://earth.esa.int/documents/653194/657397/speckle_filtering.pdf), last site visit: 04/02/16

ESA. https://earth.esa.int/web/guest/missions/esa-operational-eo-missions/envisat, last site visit: 6/9/15

ESA. https://earth.esa.int/web/guest/missions/esa-operational-eo-missions/envisat/history, last site visit: 6/9/15

ESA. https://earth.esa.int/web/guest/missions/esa-operational-eo-missions/envisat/operations#_56_INSTANCE_wHK8_matmp, last site visit: 6/9/15

ESA. https://earth.esa.int/web/guest/missions/esa-operational-eo-missions/envisat/instruments, last site visit: 6/9/15

ESA. https://earth.esa.int/web/guest/missions/esa-operational-eo-missions/envisat/instruments/asar, last site visit: 6/9/15

ESA. https://earth.esa.int/web/guest/missions/esa-operational-eo-missions/envisat/instruments/asar/design, last site visit: 6/9/15

ESA. https://earth.esa.int/web/guest/missions/esa-operational-eo-missions/envisat/instruments/asar/design, last site visit: 6/9/15

ESA. https://earth.esa.int/documents/507513/1077939/nest+user+manual+5.1, last site visit:8/9/15

ESA. https://sentinel.esa.int/documents/247904/685163/Sentinel-1_User_Handbook, la/st site visit: 9/9/15

ESA. https://sentinel.esa.int/web/sentinel/sentinel-1-sar-wiki/-/wiki/Sentinel%20One/Application+of+Radiometric+Calibration+LUT, last site visit: 9/9/15

ESA. https://earth.esa.int/documents/653194/657397/speckle_filtering.pdf

, last site visit: 9/9/15

ESA. https://earth.esa.int/web/guest/missions/esa-operational-eo-missions/envisat/operations#_56_INSTANCE_wHK8_matmp, last site visit:11/10/15

ESA. https://earth.esa.int/documents/653194/656796/Introduction.pdf. last site visit: 10/9/15

ESA. https://earth.esa.int/documents/653194/656796/What_Is_Polarization.pdf last site visit: 10/9/15

ESA. https://.esa.int/web/sentinel/toolboxes/sentinel-1, last site visit: 5/9/15

ESA. https://earth.esa.int/web/polsarpro/home, last site visit: 5/9/15

ESA. https://earth.esa.int/documents/653194/656796/Polarimetric_Decompositions.pdf, last site visit: 17/9/15

ESA. https://earth.esa.int/documents/653194/656796/Polarimetric_Decompo//sitions.pdf, last site visit: 17/9/15

EXELIS. http://www.exelisvis.com/docs/AdaptiveFilters.html, last site visit: 10/9/15.

Hexagon Geospatial. ERDAS IMAGINE. 2015 http://www.geosystems.fr/images/PDF/2015_ERDAS_IMAGINE_BROCHURE_SCREEN.pdf, last site visit: 24/9/15

JAXA, http://www.eorc.jaxa.jp/ALOS/en/sci/sci_index.htm, last site visit:6/9/15.

JAXA, http://www.eorc.jaxa.jp/ALOS/en/about/palsar.htm, last site visit:6/9/15

JAXA, http://www.eorc.jaxa.jp/ALOS/en/sci/general.htm, last site visit:6/9/15

JAXA, http://www.eorc.jaxa.jp/ALOS/en/sci/strategic.htm, last site visit:6/9/15

JAXA, http://www.eorc.jaxa.jp/ALOS/en/obs/palsar_strat.htm, last site visit: 6/9/15

Lee, Jong-Sen. (1980). Digital Image Enhancement and Noise Filtering by Use of Local Statistics. IEEE Transactions on Pattern Analysis and Machine Intelligence, Vol PAMI-2, No.2, March 1980, pp. 165-168. (http://www.exelisvis.com/docs/AdaptiveFilters.html), last site visit: 10/9/15.

M. Roggo, WFF, The Amazon Rainforest, (http://wwf.panda.org/about_our_earth/teacher_resources/best_place_species/current_top_10/amazon_rainforest.cfm) last site visit: 5/10/15

Natural Resources of Canada (NRC). http://www.nrcan.gc.ca/earth-sciences/geomatics/satellite-imagery-air-photos/satellite-imagery-products/educational-resources/9303, last site visit: 19/9/15

Natural Recourses Canada (N.R.C.), Tutorial: Radar Polarimetry, Date Modified: 2014-12-01 (http://www.nrcan.gc.ca/earth-sciences/geomatics/satellite-imagery-air-photos/satellite-imagery-products/educational-resources/9579), last site visit 03/09/15

Ockert. January 23, 2011. What are the differences between horizontally polarized and vertically polarized signals? techbaron. http://techbaron.com/what-are-the-differences-b
PCIGeomatics. 2015. http://www.pcigeomatics.com/geomatica help/concepts/spw_c/spw3n128.html, last site visit: 22/9/15

etween-horizontally-polarized-and-vertically-polarized-signals/ , last site visit: 4/10/15

R. Buttler. E Encyclopedia Britannica. Encyclopedia Britannica (E.B.), (last updated: July 13, 2014) http://rainforests.mongabay.com/20brazil.htm, last site visit: 25/09/15

T. G. Farr. Chapter 5. Radar Interactions With Geologic Surfaces. http://topex.ucsd.edu/rs/sar_interpretation.pdf, last site visit: 20/9/15

The editors of Encyclopedia Britannica. Encyclopedia Britannica (E.B.). Parana-River. http://www.britannica.com/place/Parana-River, last site visit: 5/10/15

The editors of Encyclopedia Britannica. Encyclopedia Britannica (E.B.). Para state River. http://www.britannica.com/place/Para-state-Brazil , last site visit: 5/09/15

The editors of Encyclopedia Britannica. Encyclopedia Britannica (E.B.). Amapa state Brazil. http://www.britannica.com/place/Amapa, last site visit: 25/09/15

The editors of Encyclopedia Britannica. Encyclopedia Britannica (E.B.). Tocantins state Brazil. http://www.britannica.com/place/Tocantins, last site visit: 25/09/15

The editors of Encyclopedia Britannica. Encyclopedia Britannica (E.B.). Goias state Brazil. http://www.britannica.com/place/Goias-state-Brazil, last site visit: 25/09/15

The editors of Encyclopedia Britannica. Encyclopedia Britannica (E.B.). Xingu river Brazil. Xingu-River, last site visit: 25/09/15

University of Colorado: http://www.colorado.edu/geography/gcraft/notes/remote/remote_f.html, last site visit: 19/9/15